

Determination of Electrostatic Potential and Charge Distribution of
Semiconductor Nanostructures using Off-axis Electron Holography

by

Luying Li

A Dissertation Presented in Partial Fulfillment
of the Requirements for the Degree
Doctor of Philosophy

Approved April 2011 by the
Graduate Supervisory Committee:

Martha R. McCartney, Co-Chair
David J. Smith, Co-Chair
Michael J. Treacy
John Shumway
Jeff Drucker

ARIZONA STATE UNIVERSITY

May 2011

ABSTRACT

The research of this dissertation involved quantitative characterization of electrostatic potential and charge distribution of semiconductor nanostructures using off-axis electron holography, as well as other electron microscopy techniques. The investigated nanostructures included Ge quantum dots, Ge/Si core/shell nanowires, and polytype heterostructures in ZnSe nanobelts. Hole densities were calculated for the first two systems, and the spontaneous polarization for wurtzite ZnSe was determined.

Epitaxial Ge quantum dots (QDs) embedded in boron-doped silicon were studied. Reconstructed phase images showed extra phase shifts near the base of the QDs, which was attributed to hole accumulation in these regions. The resulting charge density was (0.03 ± 0.003) holes/nm³, which corresponded to about 30 holes localized to a pyramidal, 25-nm-wide Ge QD. This value was in reasonable agreement with the average number of holes confined to each Ge dot determined using a capacitance-voltage measurement.

Hole accumulation in Ge/Si core/shell nanowires was observed and quantified using off-axis electron holography and other electron microscopy techniques. High-angle annular-dark-field scanning transmission electron microscopy images and electron holograms were obtained from specific nanowires. The intensities of the former were utilized to calculate the projected thicknesses for both the Ge core and the Si shell. The excess phase shifts measured by electron holography across the nanowires indicated the presence of

holes inside the Ge cores. The hole density in the core regions was calculated to be $(0.4 \pm 0.2) / \text{nm}^3$ based on a simplified coaxial cylindrical model.

Homogeneous zincblende/wurtzite heterostructure junctions in ZnSe nanobelts were studied. The observed electrostatic fields and charge accumulation were attributed to spontaneous polarization present in the wurtzite regions since the contributions from piezoelectric polarization were shown to be insignificant based on geometric phase analysis. The spontaneous polarization for the wurtzite ZnSe was calculated to be $p_{\text{sp}} = -(0.0029 \pm 0.00013) \text{ C/m}^2$, whereas a first principles' calculation gave $p_{\text{sp}} = -0.0063 \text{ C/m}^2$. The atomic arrangements and polarity continuity at the zincblende/wurtzite interface were determined through aberration-corrected high-angle annular-dark-field imaging, which revealed no polarity reversal across the interface.

Overall, the successful outcomes of these studies confirmed the capability of off-axis electron holography to provide quantitative electrostatic information for nanostructured materials.

ACKNOWLEDGMENTS

First of all, I would like to express my deepest gratitude to my advisors Professor Martha R. McCartney and Regents' Professor David J. Smith for their esteemed support and guidance that made all the exciting achievements possible. As an expert in the area of electron holography, Professor McCartney is so experienced in experimental details as well as creative in generating new ideas, discussing with her is really a spiritual enjoyment. Professor Smith is really enthusiastic to work with, and his meticulous attitude and patience in front of students deeply impresses me. Study in their group will be a great memory for me.

I would like to thank Professors Michael Treacy, John Shumway, and Jeff Drucker for serving on my dissertation committee. I am grateful for the use of facilities in the John M. Cowley Center for High Resolution Electron Microscopy, and I thank for Karl Weiss and Dr. Zhenquan Liu for their technical support and assistance throughout my research.

I would like to express my appreciation to Professor Jeff Drucker, Dr. Sutharsan Ketharanathan, Dr. Eric Dailey, and Dr. Prashanth Madras of Arizona State University, and Professor Jianbo Wang and Dr. Lei Jin of Wuhan University for their collaboration and for providing the samples used for investigation in this dissertation. Financial support from US Department of Energy (Grant No. DE-FG02-04ER46168) is also gratefully acknowledged.

Particular thanks to our research group members for their help during my stay. I thank Dr. Lin Zhou, Lu Ouyang, Wenfeng Zhao, Michael Johnson, Allison

Boley, Sahar Hihath, Jae Jin Kim, Dinghao Tang, and Zhaofeng Gan for their friendship and kindness.

Finally, I am very grateful to my family for their love and encouragement in sunny and rainy days.

TABLE OF CONTENTS

	Page
LIST OF FIGURES	ix
CHAPTER	
1. INTRODUCTION	1
1.1 Background	1
1.2 Tailoring of Charge Distribution in Semiconductors	6
1.2.1. p-n junctions	6
1.2.2. Band-alignment-induced charge distribution	9
1.2.3. Polarization-induced charge distribution	11
1.3. Growth of Semiconductor Nanostructures	15
1.3.1. Epitaxial growth	15
1.3.2. Thermal evaporation	20
1.4. Outline of Dissertation	20
References	23
2. EXPERIMENTAL DETAILS	27
2.1. Off-axis Electron Holography	27
2.1.1. Background	27
2.1.2. Experimental setup	28
2.1.3. Reconstruction of electron holograms	30
2.1.4. Mean inner potential	36
2.2. Scanning Transmission Electron Microscopy	38
2.2.1. Energy-dispersive X-ray spectroscopy	39

CHAPTER	Page
2.2.2 High-angle annular-dark field imaging	40
2.3. Sample Preparation	42
References.....	45
3. STUDY OF HOLE ACCUMULATION IN INDIVIDUAL GERMANIUM QUANTUM DOTS IN P-TYPE SILICON	47
3.1. Introduction	47
3.1.1. Hut, pyramid and dome structures.....	47
3.1.2. Composition and shape transition for capped Ge quantum dots.....	50
3.1.3. Electron charging behavior of Ge quantum dots.....	51
3.2. Experimental Details	53
3.3. Results and Discussion.....	55
3.3.1. Charge distribution in n-type and p-type Ge quantum dots	55
3.3.2. Electron holography study of n-type Ge quantum dots	57
3.3.3. Electron holography study of p-type Ge quantum dots	58
3.3.4. Comparison of hole density with C-V measurement	65
3.4. Conclusions	66
References.....	68
4. OBSERVATION OF HOLE ACCUMULATION IN Ge/Si CORE/SHELL NANOWIRES	70
4.1 Introduction	70
4.2 Experimental Details	72

CHAPTER	Page
4.2.1 Determination of crystallographic and compositional structure	73
4.2.2. Determination of projected thicknesses.....	74
4.3. Results and Discussion.....	82
4.3.1. Calculation of hole density	82
4.3.2. Comparison with published measurements.....	89
4.4. Conclusions	90
References.....	92
5. CHARACTERIZATION OF CHARGE DISTRIBUTION ACROSS HOMOGENEOUS ZINC-BLENDE/WURTZITE HETEROSTRUCTURE JUNCTIONS IN ZnSe NANOBELTS INDUCED BY SPONTANEOUS POLARIZATION.....	94
5.1. Introduction	94
5.2. Experimental Details.....	97
5.3. Results and Discussion.....	98
5.3.1. Phase shift across WZ/ZB/WZ interfaces	98
5.3.2. Piezoelectric polarization across ZB/WZ interface.....	102
5.3.3. Mean inner potentials of ZB and WZ ZnSe	106
5.3.4. Aberration-corrected HAADF imaging of ZnSe ZB/WZ interface	108
5.3.5. Spontaneous polarization of ZnSe	110
5.4. Conclusions	112

CHAPTER	Page
References.....	114
6. SUMMARY AND FUTURE WORK	117
6.1 Summary.....	117
6.2 Future Work.....	119
References.....	124
APPENDIX	
RELEVANT PUBLICATIONS	126

LIST OF FIGURES

Figure		Page
1.1	Schematic of energy bands for the intrinsic conductivity of a semiconductor	1
1.2	Illustration of energy level quantization, which creates a two-dimensional electron gas (2DEG) [4].....	3
1.3	High resolution transmission electron micrograph of Ge quantum dot embedded in Si (001)	5
1.4	Schematic illustration of the p - n junction: (a) Energy diagram of p - and n -type semiconductors before junction formation. (b) Energy diagram after junction formation [19]	6
1.5	(a) Cross section, and (b) energy-band diagram, of forward-biased LED, illustrating the emission of photons due to electron-hole recombination [4]	8
1.6	Energy bandgap of Si, Ge and several III-V compounds [22]	9
1.7	(a) Type I band alignment of GaAs-InAs quantum dot. (b) Type II band alignment of Si-Ge quantum dot [27]	11
1.8	(a) Reconstructed phase image of an n -AlGaIn/InGaIn/AlGaIn/ p -AlGaIn heterojunction diode. (b) Experimental energy profile (open circles) and profiles (solid lines) [31].....	14
1.9	(a) Si-C bond chain along the stacking direction in the zincblende/wurtzite superlattice used for calculation. Small and large solid circles represent C and Si atoms, respectively [38]	16

Figure		Page
1.10	Sketch of the three primary growth modes. (a) Frank-van der Merwe growth mode. (b) Volmer-Weber growth mode. (c) Stranski-Krastanov growth mode	18
1.11	Sketch of the growth of Ge nanowires on Si substrate applying the vapor-liquid-solid growth mode. The Au seeds act as catalyst [46]	19
2.1	Geometry for off-axis electron holography in conventional TEM	29
2.2	Schematic illustrating the procedure for reconstructing electron hologram	31
2.3	Schematic illustration of the origins of holographic phase shifts due to electrostatic and magnetic fields [5]	34
2.4	Schematic showing essential components associated with the scanning transmission electron microscopy technique	39
2.5	The parameter ν as a function of the inner detector angle for outer detector angles = 0.2 rad (solid line), 0.5 rad (dotted line) and 1.0 rad (dashed line), respectively [30]	43
2.6	Image of the angle adjustment plate of the MultiPrep TM polishing device [31]	44
3.1	Diamond crystallographic structure of Ge and Si	48
3.2	(a) Elevated temperature STM image of hut and pyramid structures [10]. (b) Image of Ge multifaceted dome structure obtained using AFM [14]	49

Figure	Page
3.3	(a) The average Ge concentration in dome structure vs substrate temperature [17]. (b) Ge concentration in dome structure vs deposition rate [18] 51
3.4	Schematic of flat, truncated-pyramid island model 52
3.5	Schemes of layered growth for: (a) <i>n</i> -type; and (b) <i>p</i> -type; Ge QDs on Si (100) substrate 54
3.6	(a) Calculated profile of conduction and valence bands along the <i>z</i> axis [22]. (b) Calculated structure of the wave functions of two electrons and a hole localized in the vicinity of a Ge pyramid [23] 55
3.7	Theoretical modeling of: (a) phase shift distribution; and (b) projected potential distribution, induced by electron accumulation at <i>n</i> -type Ge QDs 57
3.8	<i>n</i> -type Ge quantum dot studied by electron holography. (a) Reconstructed phase image averaged from ten serial holograms. (b) Corresponding thickness image 58
3.9	(a) Electron hologram of individual Ge QD, embedded in Si [001] substrate, recorded in [110] projection. (b) Sketch of the pyramid-shaped dot and wetting layer [1]..... 60
3.10	(a) Line profile from A and B in Fig. 3.9 (b), shown as red line with squares. Blue line with open circles is the line profile across wetting layer only from C to D, as indicated in Fig. 3.9 (b) [1] 63

Figure	Page
3.11	Experimental C - V plots in red with theoretical reference C - V plot of conventional p -type Schottky diode without any Ge dots shown in blue dashed line [1] 65
4.1	(a) HREM image of Ge/Si core/shell NW with core diameter of 15 nm and shell thickness of 5 nm. (b) Room temperature electrical transport in Ge/Si core/shell NWs [5]..... 71
4.2	(a) HREM image confirming Ge/Si core/shell NW growth with good crystallinity. (b) HAADF image of Ge/Si core/shell NW showing brighter contrast in the core [1] 75
4.3	Sketch of cross-sectional sample preparation for Si NWs 76
4.4	HREM image showing cross section of Si NW orientated along [111] zone axis 77
4.5	(a) $\langle 110 \rangle$ Ge NWs formed by seedless VLS growth at $T = 300\text{ }^{\circ}\text{C}$ and $P = 5\text{ mtorr}$ digermane imaged using SEM. (a) and (b) grown with $\theta_{\text{Au}} = 1/2\text{ ML}$. (c) and (d) grown with $\theta_{\text{Au}} = 1\text{ ML}$ [7]..... 78
4.6	(a) HAADF image of Ge/Si core/shell NW with region used for intensity line profile analysis indicated by dashed black arrow. The outlined region inside the box [1]..... 81
4.7	(a) Electron hologram of the Ge/Si core/shell NW observed by HAADF. (b) Reconstructed phase image of NW with the area used for HAADF intensity line profile [1] 84

Figure	Page
4.8	Sketch of the co-axial cylindrical model of Ge/Si core/shell nanowire: the charge distributions in the core and shell surface regions are indicated [1]..... 86
4.9	(a) Schematic side view of the Ge NWs FETs with back-gates and 10-nm-thick SiO ₂ as the gate insulator. (b) Hole mobility vs gate voltage estimated from the transconductance of the device [17] 90
5.1	(a) Typical photoluminescence spectra obtained from three types of GaAs nanowires at T= 4.2 K. The percentage of wurtzite compared to zincblende structure increases from α to γ [8-9]..... 96
5.2	Calculated (a) valence band and (b) conduction band offsets as a function of iconicity f_i . Empty and filled squares and circles represent the band offsets [10]..... 97
5.3	(a) Electron hologram from ZnSe nanobelt location including WZ/ZB/WZ junctions. (b) HREM image of the same nanobelt at higher magnification. (c) Reconstructed phase image [1] 99
5.4	Sketches of: (a) unit cell of wurtzite structure; and (b) unit cell of zincblende structure 101
5.5	(a) HREM image of the ZB/WZ interface as used for strain map calculation. (b) Strain map for ε_{zz} ; and (c) strain map for ε_{xx} of the same region of HREM imaging [1] 103

Figure	Page
5.6	Simulations of the amplitude/phase VS. thickness relations for the transmitted beam (the (000) beam) for: (a) ZB structure at $[-110]$ zone axis; and (b) WZ structure at $[-2110]$ zone axis 106
5.7	(a) Aberration-corrected HAADF image of ZB/WZ interface: the Zn-Se atomic columns are clearly observed. The intensity line profiles along an array of Zn-Se atomic columns in ZB region [1]..... 109
5.8	(a) Electron hologram of ZnO film. (b) Phase image reconstructed from the hologram. (c) Averaged one-dimensional phase change profile obtained from the box region in (b) [36] 111
6.1	Scanning transmission electron microscopy image of Ge <i>pn</i> junction nanowires. The top inset shows the junction position, which is of slight larger diameter [6] 120
6.2	(a) Transmission electron micrograph of GaAs nanopillar. (b) Corresponding high-resolution electron micrograph shows high density of stacking faults and twinning structures 122

Chapter 1

INTRODUCTION

1.1 Background

Semiconductors are generally classified in terms of their electrical conductivity with electron currents intermediate in magnitude between that of a conductor and an insulator. Conductivity values are roughly in the range of 10^5 to 10^{-6} siemens per meter, and are strongly dependent on temperature. A highly purified and undoped semiconductor exhibits what is called intrinsic conductivity: the schematic energy band diagram for a semiconductor is shown in Figure 1.1. The conductivity at 0 K is effectively zero since all states in the valence band are filled and all states in the conduction band are vacant. The band gap energy, E_g , which is defined as the difference in energy between the lowest point of the conduction band and the highest point in the valence band, is narrower for

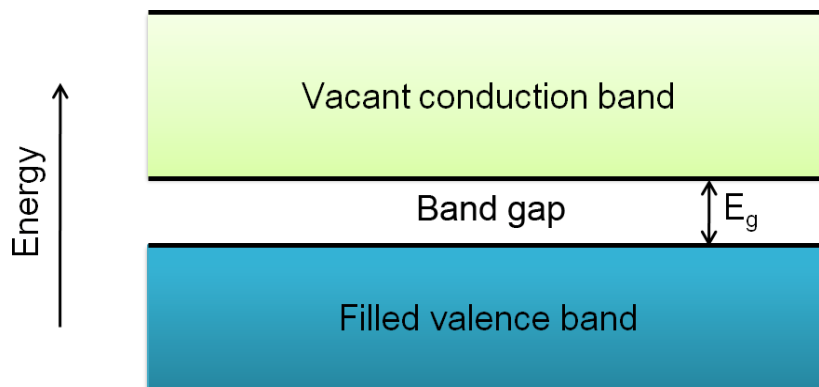


Figure 1.1 Schematic of energy bands for the intrinsic conductivity of a semiconductor.

semiconductors (the value is normally less than ~ 2 eV) than for insulators. Thus, electrons can be easily excited thermally from the valence band to the empty conduction band as temperature is increased, and the intrinsic conductivity is created [1].

The electronic properties and conductivity of a semiconductor can be modified in a controlled manner by introducing very small quantities of impurity atoms, usually called “dopants”, to the crystal lattice, making the semiconductor extrinsic. Thus, dopants can drastically affect the electrical behavior of the semiconductor. The introduction of dopants can be realized through different techniques: methods in the case of Si include doping of molten Si before Czochralski growth, diffusion from a gaseous doping substance into Si, ion implantation, epitaxial growth of a doped Si layer onto an existing substrate, and neutron doping [2].

Semiconductor electronics has progressed from the ordinary world of classical physics to the entirely different world of quantum mechanics. In reference to small systems, the term ‘Microscopic’ refers to individual atoms, and engineering on a scale of no more than about 10 \AA . The term ‘Mesoscopic’ refers to a much larger number of atoms or a larger scale, but where quantum effects are still crucial (say, 500 \AA to 1500 \AA). ‘Macroscopic’ systems have sizes in the range of microns or larger, and are expected to behave classically [3]. The following discussion refers mostly to mesoscopic systems.

Quantum effects arise in systems which confine electrons to regions comparable to their de Broglie wavelength. When the confinement occurs in one

dimension, a two-dimensional electron gas (2DEG) is created. The high-electron mobility transistor (HEMT) contains a triangular potential well, with close to zero width at the tip. In this case, the quantum-mechanical properties of electrons become important: energy levels are quantized, and the energy separation between energy levels (subbands) depends on the electron wavelength and the side slope of the potential well. The latter is directly related to the electric field that creates the triangular potential well. Electrons in the energy subbands do not move freely, and they are not randomly scattered in the direction of the potential well cross section (x -direction, as shown in Figure 1.2). In this direction, the electrons would appear as standing waves. In the other two directions (y and z), the potential well is much larger than the electron wavelength, the electrons can

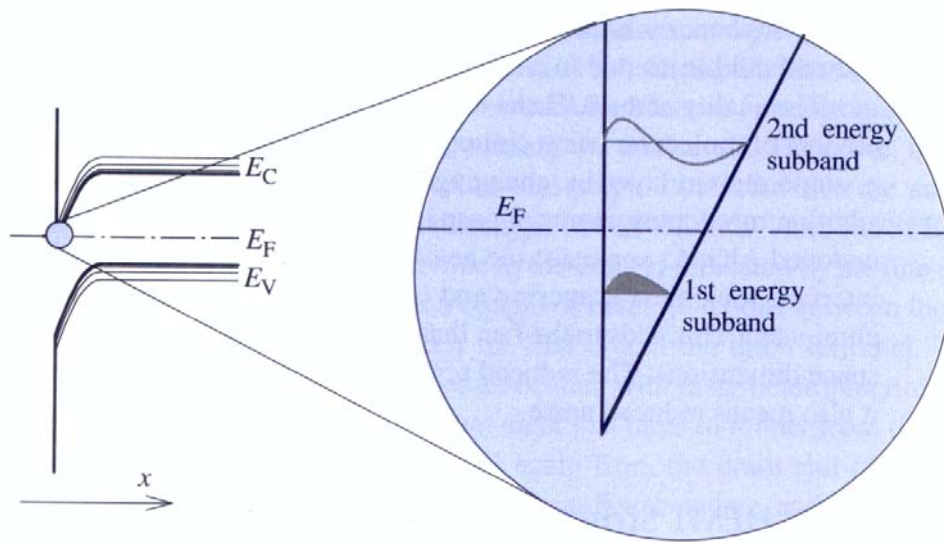


Figure 1.2 Illustration of energy level quantization, which creates a two-dimensional electron gas (2DEG) [4].

move freely and are randomly scattered. Thus, the concept of ‘electron gas’ can be applied only to these two dimensions [4].

Confinement in two dimensions (say, y and z) with free motion in the x -direction gives rise to a ‘one-dimensional electron gas’ (1DEG). Semiconductor nanowires (NWs) offer many opportunities for 1DEG formation through the bottom-up paradigm. Metal nanoparticles can be used as ‘catalysts’ for NW growth within the context of vapor-liquid-solid growth [5, 6], which is discussed in detail below, and the NW diameters can be controlled by the size of the nanoparticle ‘catalysts’ [7]. The controlled growth of radial heterostructures has been realized in Ge/Si, Si/Ge and Si/Ge/Si [8-10], n-GaN/InGaN/p-GaN [11], and p-Si/n-CdS [12] core/shell NWs. Due to the valence band offset of ~ 500 meV between the epitaxial Ge core and Si shell, free holes accumulate in the Ge channel when the Fermi level lies below the valence band edge of the Ge core. Low-temperature electrical transport studies have shown distinct conductance plateaus, and the conductance exhibits little temperature dependence, indicating ballistic transport at room temperature [9-10, 13].

Confinement in all three dimensions gives a ‘zero-dimensional electron gas’ (0DEG). Self-assembled quantum dots (QDs) are being intensively studied due to their capability of forming 0DEG [14]. Although there are several ways to fabricate *in situ* QD structures, most approaches fail to realize size uniformity of the dot ensemble and high interface definition of the individual dots [3]. The Stranski-Krastanov growth mode is widely utilized in formation of the small 3D

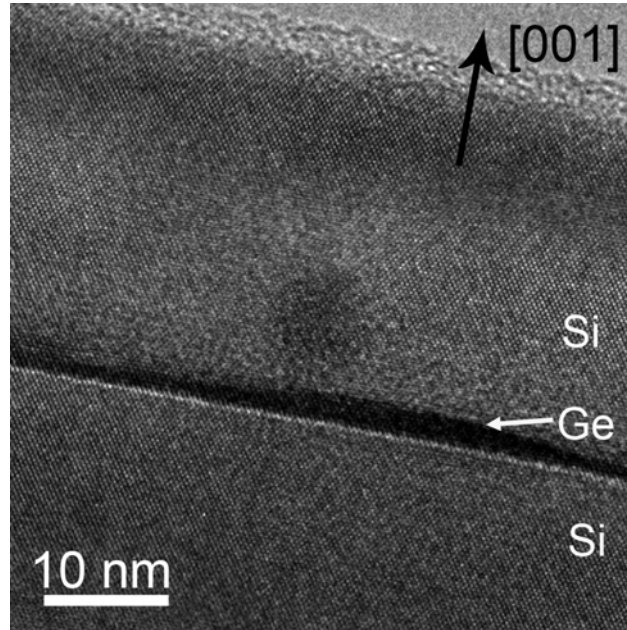


Figure 1.3 High resolution transmission electron micrograph of Ge quantum dot embedded in Si (001).

islands. The prototypical cases are InAs on GaAs (001) [15] and Ge on Si (001) [16], both being primarily produced using the growth technique of molecular beam epitaxy (MBE). Several other studies report QDs grown by metalorganic vapor phase epitaxy (MOVPE), which also exhibit this morphology [17-18]. As shown in Figure 1.3, when 3D Ge islands are embedded within epitaxial layers of Si (001), which has a wider band gap, the carriers within the islands are expected to be confined by the potential barriers that surround each island, forming the 0DEG. The electron holographic study of hole accumulation at Ge QDs is described in detail in Chapter 3.

1.2 Tailoring of Charge Distribution in Semiconductors

1.2.1 p - n junctions

A p - n junction is formed between two semiconductor regions having opposite types of doping. If the n - and p - regions are of the same semiconductor, then the junction is a homojunction. If the semiconductor materials are different, the junction is called a heterojunction. One of the most relevant characteristics of p - n junctions is that they rectify current, allowing electrons to flow easily in only one direction.

As sketched in Figure 1.4 (a), the two regions of p - and n -type semiconductor are normally uniformly doped and physically separated before the junction is

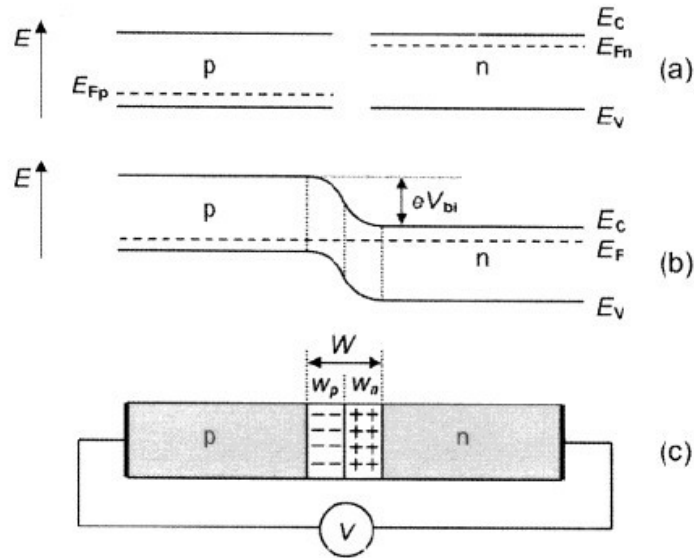


Figure 1.4 Schematic illustration of the p - n junction: (a) the energy diagram of a p - and n -type semiconductors before junction formation. (b) The energy diagram after junction formation in thermal equilibrium. (c) The depletion region of a p - n junction [19].

formed. The Fermi level E_F is near the valence band edge in the p -type material and near the conduction band edge in the n -type material. When the two regions are joined together, the electrons in n -type region and holes in p -type region diffuse across the junction. These electrons and holes recombine with each other, leading to the formation of the depletion region (W), as shown in Figure 1.4 (c), which is depleted of mobile carriers. As holes continue to leave the p -side, some of the negative acceptor ions (N_a) near the junction are left uncompensated, since the acceptors are fixed in the semiconductor lattice, whereas the holes are mobile. Consequently, a negative space charge forms near the p -side of the junction. For similar reasons, a positive space charge forms near the n -side due to the existence of the immobile positive donor ions (N_d). This space charge region creates an electric field that is directed from the positive charge to the negative charge, which effectively prevents further migration of free carriers. The internal (built-in) potential is formed as the result of the Fermi energy difference between the n - and p -type regions, as shown in Figure 1.4 (b). In thermodynamic equilibrium, the Fermi level of a p - n junction will be constant across the junction, which necessitates band bending through the junction [19-20].

The p - n junction is the fundamental building block of semiconductor devices, and its applications are based on the junction properties. The light emitting diode (LED) is basically a p - n junction that is forward biased to inject electrons and holes into the p - and n -sides respectively. The injected minority charge recombines with the majority charge in the depletion region or the neutral region. An electron in the conduction band must release some energy to drop down into

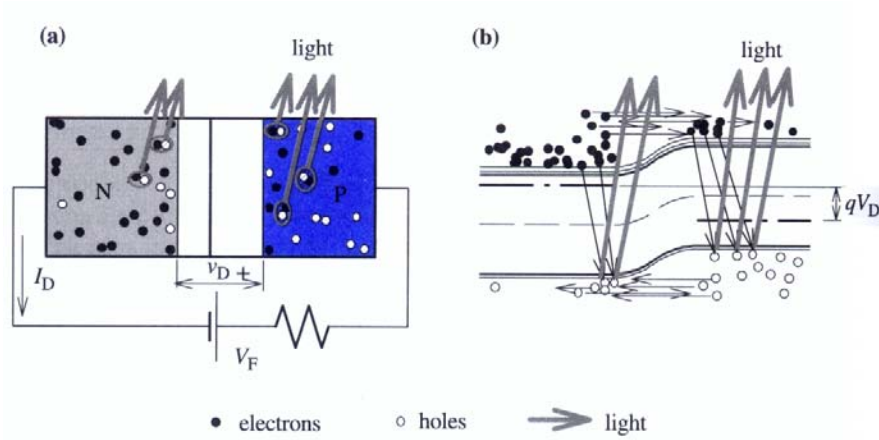


Figure 1.5 (a) Cross section, and (b) energy-band diagram, of a forward-biased LED, illustrating the emission of photons due to electron-hole recombination [4].

the valence band to recombine with a hole. The energy is released in the form of a photon, and the photon energy is approximately equal to the energy gap E_g [4, 21]. Figure 1.5 shows a schematic of the energy-band diagram and the emission of photons due to electron-hole recombinations. Besides LED applications, by absorbing incident photons of energy greater than the band gap, electron-hole pairs are separated at the junction, delivering an electric current to an external circuit, which is the basic principle for operation of a solar cell; The temperature dependence of the I-V characteristics of a p-n junction can be utilized for a temperature sensor, the non-linear nature of the I-V characteristic of a p-n junction can be used for frequency multipliers and mixers; and the p-n junction-based device can find applications as a switch in rectifiers, inverters, and power supplies [21].

1.2.2 Band-alignment-induced charge distribution

The junctions formed between two different semiconductors with different energy gaps are often referred to as heterojunctions. The main advantages of heterojunctions are better control of the charge carrier transport, which is achieved by controlling the energy barrier and potential variations across the interface, and the ability to confine the optical radiation, which is especially important in optoelectronic devices.

Combining different semiconductor materials within a single device and tailoring the shape of the energy bands to achieve certain properties is commonly referred to as “band gap engineering”. Figure 1.6 shows the bandgap energies for Si, Ge and different III-V compound semiconductors [22]. Arbitrary values of the bandgap energy can be obtained using ternary or even quaternary compounds,

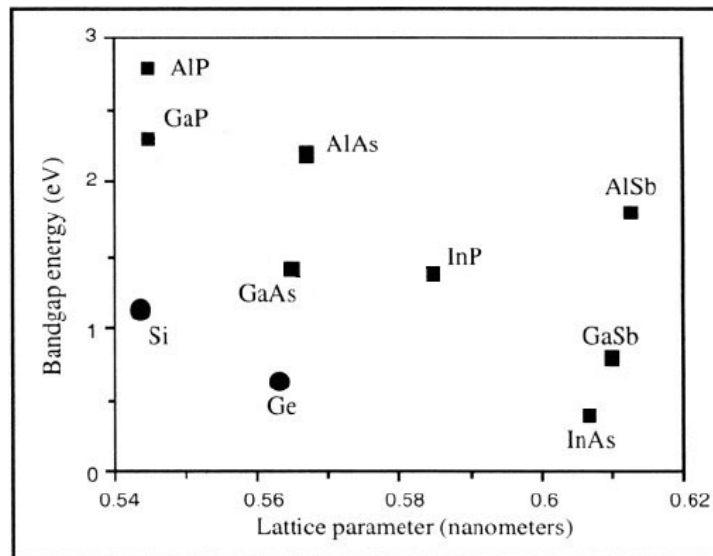


Figure 1.6 Energy bandgap of Si, Ge and several III-V compounds [22].

such as $\text{Ga}_x\text{Al}_{1-x}\text{As}$ and $\text{Ga}_x\text{In}_{1-x}\text{As}_y\text{P}_{1-y}$, by adjusting the x and y coefficients during growth [2].

The development of crystal growth techniques such as molecular-beam epitaxy [23-24] and metalorganic chemical vapor deposition [25] has made possible the growth of semiconductors with controlled composition as well as doping on a very fine scale. In order to obtain high-quality heterostructures, it is preferable to ensure that the crystal structures and lattice parameters of dissimilar materials are matched as closely as possible, in order to minimize the formation of defects. However, high-quality heterostructures can often be realized in pseudomorphic growth, when one of the semiconductor layers is sufficiently thin, so that the lattice mismatch is accommodated primarily by strain [19].

A major issue of band alignment is whether the band gap discontinuities are determined by the bulk properties of the constituent semiconductors or whether they are controlled by the interface properties. The earlier electron-affinity model [26] proposed the determination of the conduction band discontinuity from the difference between the electron affinities of the two semiconductors, i.e.,

$$\Delta E_c = e(\chi_1 - \chi_2) \quad (1.1)$$

Moreover, the Fermi levels of the two contacted semiconductors have to match at equilibrium conditions, which must result in band-bending at the interface. Thus, contact between such dissimilar materials in relation to their different electron affinities, and equalizing of their Fermi levels, results in the formation of conduction and valence band offsets. The valence band offset can be expressed as [19]:

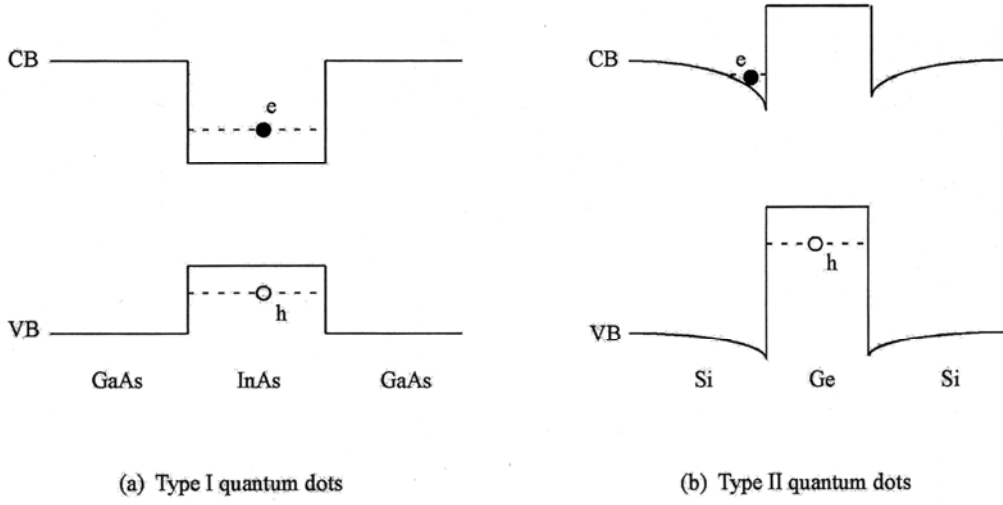


Figure 1.7 (a) Type I band alignment of GaAs-InAs quantum dot. (b) Type II band alignment of Si-Ge quantum dot [27].

$$\Delta E_v = (e\chi_2 + E_{g2}) - (e\chi_1 + E_{g1}) \quad (1.2)$$

There are two main types of band-edge alignment. For type I (straddling band alignment), the narrow-bandgap material lies entirely within the wide-bandgap material, and both electrons and holes are confined inside the same material, as shown schematically in Figure 1.7 (a). GaAs-InAs, GaAs-AlGaAs, HgCdTe-CdTe, InGaAs-AlInAs and InGaAs-InP all have type I band alignment. For type II (staggered band alignment), the electrons and holes are separated in the different materials, as shown in Figure 1.7 (b). Si-Ge and InGaAs-GaAs have type II band alignment.

1.2.3 Polarization-induced charge distribution

When a dielectric material is polarized, the sum of the dipole moments in a unit volume is nonzero, which thus defines the polarization as the dipole moments per unit volume. The polarization of a dielectric ordinarily results from an electric field, which lines up the atomic or molecular dipoles:

$$\vec{P} = \epsilon_0 \chi_e \vec{E} \quad (1.3)$$

The constant χ_e is called the electric susceptibility of the medium, which depends mainly on the microscopic structure of the substance, and also on external conditions such as temperature [28].

Spontaneous polarization is related to the non-centrosymmetry of certain crystal structures. There are 10 non-centrosymmetric classes which can theoretically show spontaneous polarization (1, 2, 3, 4, 6, m, mm2, 3m, 4mm, 6mm). Spontaneous polarization is temperature-dependent, so that when spontaneous polarization is already present, a change of temperature will alter it: this phenomenon is called pyroelectricity [29].

Piezoelectric polarization is related to strain-induced crystal structural change. In the linear regime, the piezoelectric polarization can be represented by the expression:

$$P_i = \sum_j e_{ij} \epsilon_j \quad (1.4)$$

which defines the piezoelectric tensor e_{ij} . In the absence of external fields, the total macroscopic polarization P of a solid is the sum of the spontaneous polarization P_{SP} in the equilibrium structure, and the strain-induced piezoelectric polarization P_{PE} [30].

For the nitride-based heterostructures, the electrostatic potential across the junctions usually consists of the combined contributions from both spontaneous polarization and piezoelectric polarization [31-32]. Figure 1.8 (a) shows a reconstructed phase image of a $n\text{-Al}_{0.1}\text{Ga}_{0.9}\text{N}/\text{In}_{0.1}\text{Ga}_{0.9}\text{N}/\text{Al}_{0.3}\text{Ge}_{0.7}\text{N}/p\text{-Al}_{0.1}\text{Ga}_{0.9}\text{N}$ heterojunction diode grown along [0001] direction [31]. Figure 1.8 (b) shows energy profiles across the junctions. The open circles represent the energy profile obtained after converting the potential to energy and subtracting the mean inner potential offset. The other four black lines correspond to energy profiles simulated for the $p\text{-}n$ junction, the spontaneous polarization and the piezoelectric polarization. It was found that the individual polarization contributions were insufficient to account for the observed energy profile [31]. Figure 1.8 (c) shows the experimental energy profile (open circles) and the simulated profile (dotted line) incorporating the effects of the $p\text{-}n$ junction, the spontaneous and piezoelectric polarization, and also additional charge accumulation, which gave the best fit with the experimental profile. Figure 1.8 (d) shows the charge density of the bound-polarization-induced interface charge (solid line) and additional charge (dotted line) [31]. For this specific example, both the spontaneous and piezoelectric polarization played important roles in forming the energy profile across the heterojunction.

Controlled growth of twinning or polytype superlattices also makes homogeneous heterostructure junctions possible [33-36]. For example, SiC exists as many different polytypes, namely the cubic zincblende (3C) structure, wurtzite

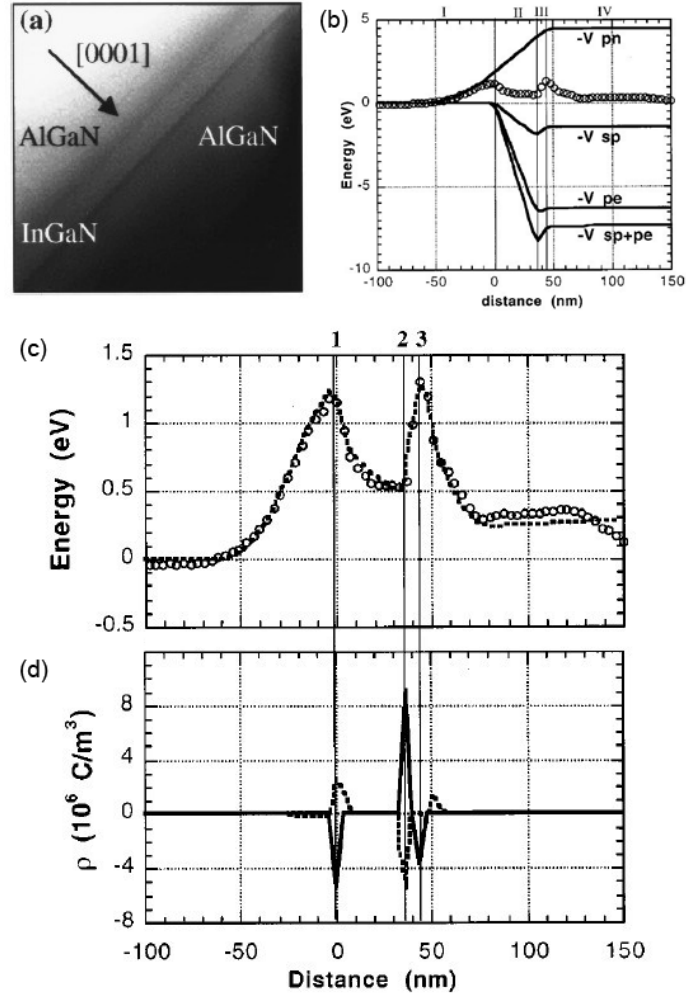


Figure 1.8 (a) Reconstructed phase image of an n -AlGaN/InGaN/AlGaN/ p -AlGaN heterojunction diode. (b) Experimental energy profile (open circles) and profiles (solid lines) correspond to the p - n junction, the spontaneous, piezoelectric polarization. (c) Experimental energy profile (open circles) and simulation (dotted line) incorporating spontaneous and piezoelectric polarization. (d) Bound polarization-induced surface charge (solid line) and additional charge for energy simulation [31].

(2H) structure, and the polytypes (4H), (6H), with many intermediate phases. These polytypes are generated by different sequences of stacking along the [111] direction of an otherwise perfect cubic structure. The wurtzite structure possesses intrinsic spontaneous polarization since the tetrahedral bonds do not have centrosymmetry. The zincblende structure has no bulk spontaneous polarization, and it can act as a perfect medium to form zincblende/wurtzite polytype heterostructures since the two structures are perfectly matched at the (111) interface. The surface and truncation effects can be neglected [37], and the piezoelectric polarization at the interface is expected to be insignificant.

The chains of Si-C bonds along the stacking direction for the zincblende/wurtzite superlattice are shown in Figure 1.9 (a). The corresponding average charge density (solid line) and average total potential (dashed line) of the zincblende/wurtzite superlattice are shown in Figure 1.9 (b) [38]: the arrow shows the direction of spontaneous polarization in the wurtzite region. The average potential along the polarization axis has a sawtoothlike shape, which results from the localization of polarization charge at the interfaces. Thus, charge distribution can also be tailored through the controlled growth of homogeneous polytype heterostructures: an example of polarization-induced charge distribution for ZnSe nanobelts has been studied by off-axis electron holography, as described in Chapter 5.

1.3 Growth of Semiconductor Nanostructures

1.3.1 Epitaxial growth

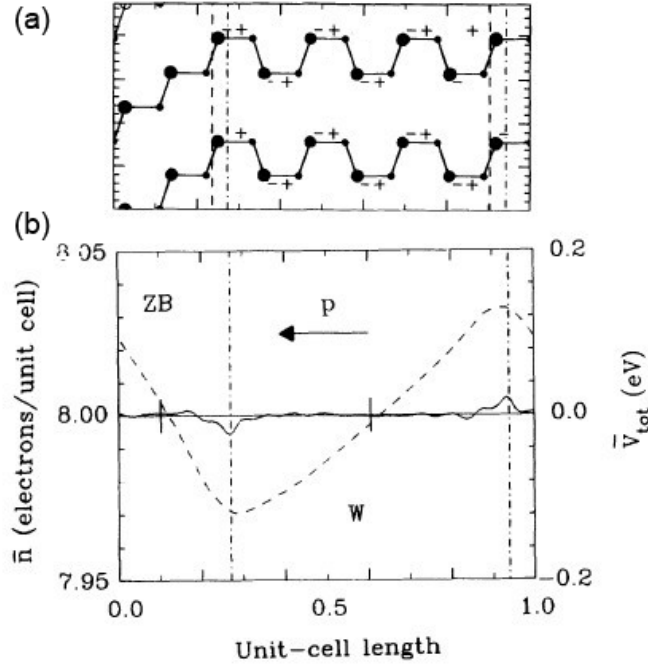


Figure 1.9 (a) Si-C bond chain along the stacking direction in the zincblende/wurtzite superlattice used for calculation. Small and large solid circles represent C and Si atoms, respectively. (b) Averaged charge density (solid line) and averaged total potential (dashed line) of the above superlattice. The arrow shows the direction of spontaneous polarization in the wurtzite region [38].

In the epitaxial growth process, the substrate wafer normally acts as the seed crystal. The most common epitaxial growth techniques include molecular-beam epitaxy (MBE) and chemical-vapor deposition (CVD).

MBE is an epitaxial process which requires ultrahigh-vacuum (UHV) conditions, and it can achieve precise control in both chemical composition and doping profiles [39]. MBE is essentially a two-step process: in the first step,

atoms or homoatomic molecules of the growing material are evaporated from solid sources in Knudsen cells, and then collimated into beams and directed toward the heated substrate which is typically several centimeters at least in diameter. Deposition onto the substrate is ballistic. The second step involves migration of the deposited species on the substrate surface before incorporation into the growing material: this is considered to be a nonequilibrium, or driven process [3].

CVD is also known as vapor-phase epitaxy (VPE), and it is a process whereby an epitaxial layer is formed by molecular beams originating from gas sources. The mechanism of CVD involves several steps: (a) the reactants such as gases and dopants are transported to the substrate region; (b) the reactants are transferred to the substrate surface where they are absorbed; (c) a chemical reaction occurs, catalyzed at the surface, and the epitaxial layer starts to grow; (d) gaseous by-products are desorbed by the main gas stream; and (e) the resultant products are transported out of the chamber [20].

For small amounts of one material deposited onto the surface of another material, epitaxial growth normally follows one of three principal growth modes [40-43]: Frank-van der Merwe (FvdM, layer-by-layer growth), Volmer-Weber (V-W, 3D island growth) and Stranski-Krastanov (S-K, layer-plus-island growth), as sketched in Figure 1.10. Which mode will be adopted for a specific system depends on the interfacial free energy (γ_{int}) between the substrate and the epilayer, the surface energy of the film (σ_{film}) and the surface energy of the substrate (σ_{sub}): these have been labeled for each growth mode in Fig. 1.10. The FvdM and V-W

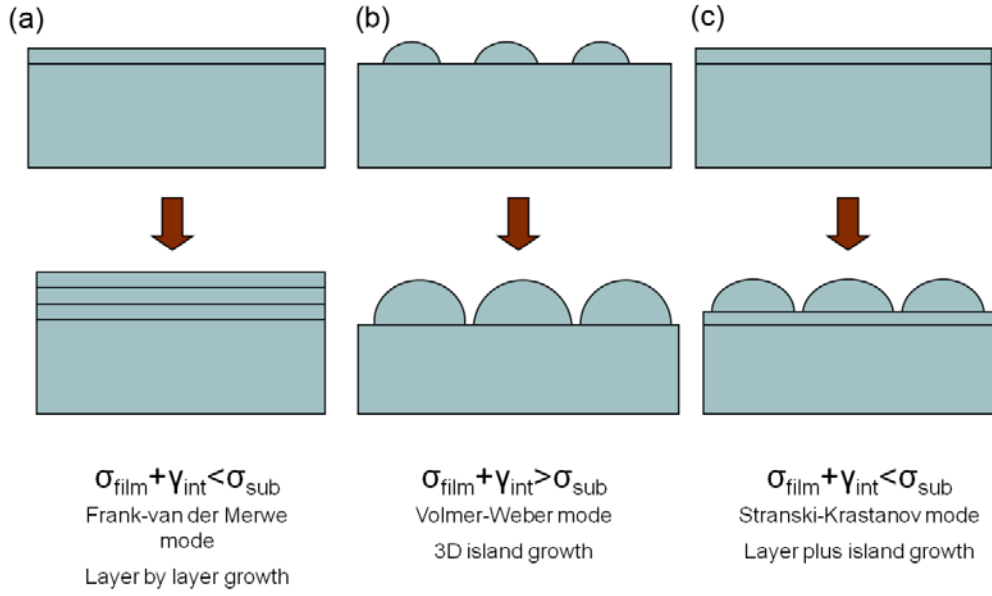


Figure 1.10 Sketch of the three primary growth modes. (a) Frank-van der Merwe growth mode. (b) Volmer-Weber growth mode. (c) Stranski-Krastanov growth mode.

modes are usually applicable to lattice-matched systems, while the S-K mode is observed in systems where there is appreciable lattice mismatch between the substrate and the epilayer. The increasing elastic energy during initial growth normally causes a transition from layered growth to 3D island growth after a certain “critical thickness”. The growth of Ge quantum dots on Si (100) substrates, which are discussed in detail in Chapter 3, follows the S-K growth mode.

There are several modes for growing freestanding nanowires (NWs) out of the substrate surface including vapor-liquid-solid (VLS) [44-48], vapor-solid-solid (VSS) [49] and solution-liquid-solid (SLS) [50-51] growth. The VLS growth mode has been the most extensively used method for NW growth. It was first

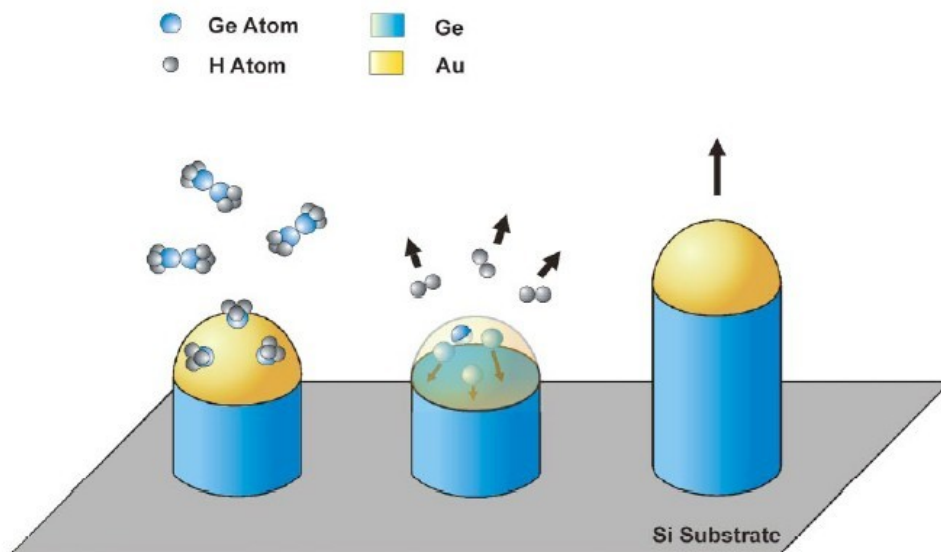


Figure 1.11 Sketch of the growth of Ge nanowires on Si substrate applying the vapor-liquid-solid growth mode. The Au seeds act as catalyst [46].

used by Wagner and Ellis for successfully depositing micrometer-sized silicon whiskers in the presence of gold impurities [44], and the growth mechanism is sketched in Figure 1.11. For the growth of Ge NWs on Si substrates, a precursor vapor transports the growth species (GeH_4) to the liquid metal (Au) seeds, where decomposition occurs and a liquid AuGe eutectic forms, with release of hydrogen and Ge atom diffusion to the liquid-solid interface under the influence of the concentration gradient. As more Ge is incorporated into the seed, it becomes supersaturated, prompting crystallization and NW growth at the interface between the GeAu eutectic and the Si substrate below. As growth continues, the incoming Ge atoms precipitate at the interface between the liquid droplet and the

Ge NW interface. The Au seeds act as catalyst and their sizes determine the diameter of the growing nanowires [48]. The Ge/Si core/shell nanowires studied in Chapter 4 were grown by CVD through the vapor-liquid-solid growth mechanism.

1.3.2 Thermal evaporation

Thermal evaporation is an economic and low toxicity method often used for growing nanostructures. A horizontal double-zone tube furnace can be utilized for synthesis, where the source material is loaded in the high temperature zone, and sublimated to obtain the vapor source. The substrate is placed downstream in the low temperature zone. The furnace is then pumped and purged with the carrier gas to remove residual oxygen. By Setting up the appropriate rate of the carrier gas, reaction pressure, and growth temperature, then the vapor-phase source material starts to precipitate and nucleate on the substrate. After a certain period of time, the furnace is cooled naturally to room temperature, and the nanostructure products are obtained. The resulting morphology and structure depend on several conditions: the source material, the evaporation and growth temperatures, the existence and type of catalyst, the reaction pressure, and the type and rate of carrier gas [52]. The ZnSe nanobelts studied in Chapter 5 were grown by the thermal evaporation method.

1.4 Outline of Dissertation

The research described in this dissertation involves determination of electrostatic potential and charge distributions in nanostructures using the technique of off-axis electron holography. The scanning transmission electron microscopy technique was also used in some of the research either to provide accurate information about sample thickness, or to determine atomic structures at interfaces. In terms of morphology, self-assembled quantum dots, core/shell nanowires and nanobelts have been studied; In terms of charge redistribution, the band-offset-induced charge redistribution and the spontaneous polarization-induced charge redistribution are presented.

In chapter 2, the theory of off-axis electron holography is briefly described, followed by an outline of the process used for reconstruction of electron holograms, the definition of mean inner potential and description of the experimental setup for off-axis electron holography. The basis of energy-dispersive X-ray spectroscopy and high-angle annular-dark-field imaging are also briefly discussed. The sample preparation methods involved in this research are also described.

In chapter 3, the electrostatic potential and accumulation of holes in individual Ge quantum dots embedded in *p*-type Si are characterized using off-axis electron holography. The corresponding hole density was calculated through polynomial fitting of the experimental data and application of the Poisson equation. C-V measurements for determining the average hole density in an ensemble of Ge QDs incorporated in a Schottky diode were also carried out in parallel. The reasonable agreement between the resulting hole densities illustrated

the capability for nanometer-scale charge density measurements by electron holography.

In chapter 4, structural and compositional information for Ge/Si core/shell nanowires were determined using high-resolution electron microscopy and energy-dispersive X-ray spectroscopy. High-angle annular-dark-field imaging was also utilized to determine the projected thicknesses for both the core and shell regions. The extra phase shift due to charge accumulation was calculated, and was then converted to hole density based on a simple cylindrical model. Comparison with estimates of hole densities based on published measurements showed reasonable agreement.

In chapter 5, the charge distribution across homogeneous ZnSe zincblende/wurtzite heterostructure junctions which is attributed to the spontaneous polarization in the wurtzite regions, is characterized by off-axis electron holography. The spontaneous polarization of ZnSe was calculated based on the experimental data, and compared with the value obtained from first-principles' calculations. The contributions from piezoelectric polarization were verified to be insignificant, and the atomic arrangement and polarity continuity across the zincblende/wurtzite interface were determined through aberration-corrected high-angle annular-dark-field imaging.

In chapter 6, the important results and achievements in this thesis are summarized, and possible studies that could be carried out in the future are described.

REFERENCES

- [1] C. Kittel, Introduction to Solid State Physics, John Wiley& Sons, Inc., New Jersey (2005).
- [2] Jean-Pierre Colinge, and C. A. Colinge, Physics of Semiconductor Devices, Kluwer Academic Publishers, New York (2002).
- [3] K. Barnham and D. Vvedensky, Low-dimensional Semiconductor Structures, Cambridge University Press, Cambridge (2001).
- [4] S. Dimitrijevic, Understanding Semiconductor Devices, Oxford University Press, New York (2000).
- [5] A. P. Levitt, Whisker Technology, Wiley, New York (1970).
- [6] R. S. Wagner and W. C. Ellis, Appl. Phys. Lett. **4**, 89 (1964).
- [7] A. M. Morales and C. M. Lieber, Science **279**, 208 (1998).
- [8] L. J. Lauhon, M. S. Gudiksen, D. Wang and C. M. Lieber, Nature **420**, 57 (2002).
- [9] W. Lu, J. Xiang, B. P. Timko, Y. Wu and C. M. Lieber, Proc. Natl. Acad. Sci. U.S.A. **102**, 10046 (2005).
- [10] J. Xiang, W. Lu, Y. Hu, Y. Wu, H. Yan and C. M. Lieber, Nature **441**, 489 (2006).
- [11] F. Qian, Y. Li, S. Gradečak, D. Wang, C. J. Barrelet and C. M. Lieber, Nano Lett. **4**, 1975 (2004).
- [12] O. Hayden, A. B. Greytak and D. C. Bell, Adv. Mater. **17**, 701 (2005).
- [13] Y. Li, F. Qian, J. Xiang and C. M. Lieber, Mater. Today **9**, 18 (2006).
- [14] A. I. Yakimov, N. P. Stepina, A. V. Dvurechenskii and A. I. Nikiforov and A. V. Nenashev, Phys. Rev. B **63**, 045312 (2001).
- [15] S. Guha, A. Madhukar and K. C. Rajkumar, Appl. Phys. Lett. **57**, 2110 (1990).
- [16] D. J. Eaglesham and M. Cerullo, Phys. Rev. Lett. **64**, 1943 (1990).
- [17] P. M. Petroff and S. P. DenBaars, Superlatt. and Microst. **15**, 15 (1994).

- [18] W. Seifert, N. Carlsson, M. Miller, M. -E. Pistol, L. Samuelson and L. R. Wallenberg, Prog. Crystal Growth and Charact. **33**, 423 (1996).
- [19] B. G. Yacobi, Semiconductor Materials: An Introduction to Basic Principles, Kluwer Academic Publishers, New York (2003).
- [20] S. M. Sze, Semiconductor Devices: Physics and Technology, John Wiley & Sons, Inc., New Jersey (2001).
- [21] U. K. Mishra and J. Singh, Semiconductor Device Physics and Design, Springer, Dordrecht (2008).
- [22] S. M. Sze, Physics of Semiconductor Devices, John Wiley & Sons, Inc., New Jersey (1981).
- [23] J. O. McCaldin and G. Somorjai, Progress in Solid State Chemistry, Pergamon, Oxford (1976).
- [24] L. Esaki and L. L. Chang, Thin Solid Films **36**, 285 (1976).
- [25] R. D. Dupuis and P. D. Dapkus, IEEE J. Quant. Electron. **QE-15**, 128 (1979).
- [26] R. L. Anderson, Solid State Electron. **5**, 341 (1962).
- [27] S. Ketharanathan, Ph. D. dissertation, Arizona State University (2007).
- [28] D. J. Griffiths, Introduction to Electrodynamics, Prentice Hall, New Jersey (1999).
- [29] J. F. Nye, Physical Properties of Crystals, Clarendon Press, Oxford (1957).
- [30] F. Bernardini, V. Fiorentini and D. Vanderbilt, Phys. Rev. B **56**, R10024 (1997).
- [31] M. R. McCartney, F. A. Ponce, J. Cai and D. P. Bour, Appl. Phys. Lett. **76**, 3055 (2000).
- [32] O. Ambacher, R. Dimitrov, M. Stutzmann, B. E. Foutz, M. J. Murphy, J. A. Smart, J. R. Shealy, N. G. Weimann, K. Chu, M. Chumbes, B. Green, A. J. Sierakowski, W. J. Schaff and L. F. Eastman, Phys. Stat. Sol. (b) **216**, 381 (1999).

- [33] R. E. Algra, M. A. Verheijen, M. T. Borgström, Lou-Fé Feiner, G. Immink, W. J. P. van Enkevort, E. Vlieg and E. P. A. M. Bakkers, *Nature* **456**, 369 (2008).
- [34] P. Caroff, K. A. Dick, J. Johansson, M. E. Messing, K. Deppert and L. Samuelson, *Nature Nanotech.* **4**, 50 (2009).
- [35] F. M. Ross, *Nature Nanotech.* **4**, 17 (2009).
- [36] D. Spirkoska, J. Arbiol, A. Gustafsson, S. Conesa-Boj, F. Glas, I. Zardo, M. Heigoldt, M. H. Gass, A. L. Bleloch, S. Estrade, M. Kaniber, J. Rossler, F. Peiro, J. R. Morante, G. Abstreiter, L. Samuelson and A. Fontcuberta i Morral, *Phys. Rev. B* **80**, No. 245325 (2009).
- [37] M. Posternak, A. Baldereschi and A. Catellani, *Phys. Rev. Lett.* **64**, 1777 (1990).
- [38] A. Qteish, V. Heine and R. J. Needs, *Phys. Rev. B* **45**, 6534 (1992).
- [39] M. A. Herman and H. Sitter, *Molecular Beam Epitaxy*, Springer-Verlag, Berlin (1996).
- [40] F. C. Frank and J. H. van der Merwe, *Proc. R. Soc. London A* **198**, 205 (1949).
- [41] M. Volmer and A. Weber, *Z. Phys. Chem.* **119**, 277 (1926).
- [42] I. N. Stranski and Von L. Krastanov, *Akad. Wiss. Lit. Mainz Math. –Natur. K1. IIb* **146**, 797 (1939).
- [43] J. A. Venables, G. D. T. Spiller and M. Hanbucken, *Rep. Prog. Phys.* **47**, 399 (1984).
- [44] R. S. Wagner and W. C. Ellis, *Appl. Phys. Lett.* **4**, 89 (1964).
- [45] Y. Wu and P. Yang, *Chem. Meter.* **12**, 605 (2000).
- [46] G. Gu, M. Burghard, G. T. Kim, G. S. Düsberg, P. W. Chiu, V. Krstic, S. Roth and W. Q. Han, *J. Appl. Phys.* **90**, 5747 (2001).
- [47] D. Wang and H. Dai, *Angew. Chem. Int. Ed.* **41**, 4783 (2002).
- [48] J. W. Dailey, J. Taraci, T. Clement, D. J. Smith, J. Drucker and S. T. Picraux, *J. Appl. Phys.* **96**, 7556 (2004).

- [49] T. I. Kamins, R. S. Williams, D. P. Basile, T. Hesjedal and J. S. Harris, J. Appl. Phys. **89**, 1008 (2001).
- [50] T. Hanrath and B. A. Korgel, J. Am. Chem. Soc. **124**, 1424 (2002).
- [51] J. R. Heath and F. K. LeGoues, Chem. Phys. Lett. **208**, 263 (1993).
- [52] L. Jin, Ph. D. dissertation, Wuhan University (2008).

Chapter 2

EXPERIMENTAL DETAILS

This chapter describes the background and experimental setup needed for the off-axis electron holography technique, and the process used to reconstruct electron holograms to obtain phase and amplitude images. The definition of mean inner potential is introduced, and several models for theoretically determining mean inner potential are presented. The energy-dispersive X-ray spectroscopy technique and the high-angle annular-dark-field imaging technique, which are involved in the experimental studies described in the following chapters, are also briefly introduced.

2.1 Off-axis Electron Holography

2.1.1 Background

Traditional transmission electron microscopy (TEM) imaging techniques can only provide information about intensity distributions, whereas electron holography is a powerful electron-interference technique that can provide information about both the amplitude *and* phase of the electron wave. This property is crucial for studying electrostatic and magnetic fields because the electron wave that goes through the sample will have phase differences relative to the coherent reference wave that just passes through vacuum.

The electron holography technique was first proposed by Gabor in 1948 as a means to overcome resolution limits imposed by the spherical aberration of the

objective lens of the TEM [1]. Because of the unavailability of highly coherent electron sources, applications of the holography technique were restricted until development of the field-emission-gun (FEG) in the 1970s [2]. Since then, electron holography has steadily developed into a widely used technique. The electron holograms were previously recorded on photographic plates, and reconstruction of the object was realized by illuminating the hologram with monochromatic light parallel to the reference wave, which is referred as to the off-line optical method [3]. Quantitative electron holography became possible owing to the emergence of the slow-scan charge-coupled-device (CCD) camera [4]. Compared to the nonlinear recording achieved with the photographic plate, the CCD camera provides digital recording with linear output for a wide dynamical range over several orders of magnitude, and the speed and accuracy of the reconstruction process are also greatly enhanced [5].

There are over twenty different approaches for realizing electron holography, containing in-line, off-axis, bright-field and dark-field operation in TEM mode, and also some other geometries in STEM mode [6]. Among all these possible schemes, off-axis electron holography in the conventional TEM is the approach that is mostly widely used, and it is also the setup that has been used in our experiments.

2.1.2 Experimental setup

The coherent electron wave that is produced by the FEG can be considered as

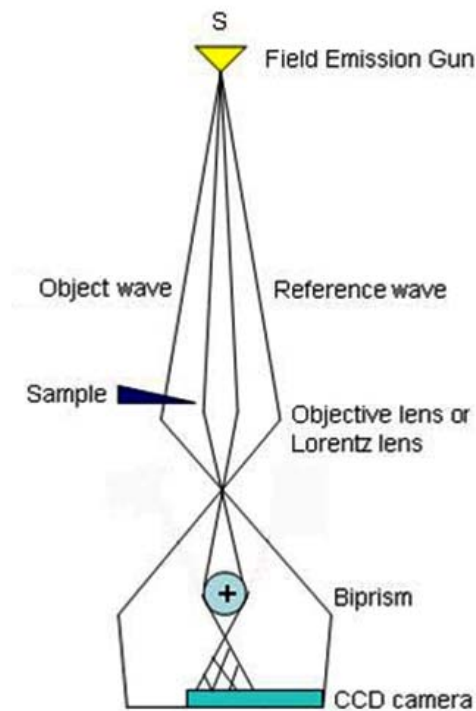


Figure 2.1 Geometry for off-axis electron holography in conventional TEM.

being split into two parts. One part, which is defined as the object wave, goes through the sample, and will contain both phase and amplitude information about the sample. The other part is transmitted through vacuum, defined as the reference wave, and can be utilized to eliminate Fresnel fringes originating from the biprism, as well as distortions caused by imperfections of the imaging/recording system [5]. Either the normal TEM objective lens or a special Lorentz mini-lens can be used. An electrostatic biprism, which is normally located at one of the selected area aperture positions, causes overlap of the object and reference waves, and the resulting interference fringes, or holograms, are recorded by CCD camera for later

quantitative analysis. The geometry for off-axis electron holography in the conventional TEM mode is shown in Figure 2.1.

2.1.3 Reconstruction of electron holograms

The electron wave that passes through the sample can be expressed as a plane wavefunction:

$$\Psi(\vec{r}) = A(\vec{r}) \exp(i\phi(\vec{r})) \quad (2.1)$$

where $A(\vec{r})$ is the amplitude, $\phi(\vec{r})$ is the phase, and \vec{r} is related to the objective exit plane. In practice, some loss of beam coherence is inevitable because of the finite gun brightness, the beam divergence due to the finite source size and the limited temporal coherence caused by energy spread. Thus, some contrast of the interference fringes would be lost. The amplitude can be expressed as: $A(\vec{r}) = |o(\vec{r}) \otimes t(\vec{r})|$, where $o(\vec{r})$ is the object function, and $t(\vec{r})$ is the point-spread function of the objective lens [7]. The total intensity of the electron hologram can then be written as:

$$I_h = 1 + A^2(\vec{r}) + 2\mu A(\vec{r}) \cdot \cos(2\pi\bar{q}_c \vec{r} + \phi(\vec{r})) \quad (2.2)$$

In this expression, μ is a constant characterizing the degree of coherence of the illumination, instabilities of the microscope, and properties of the detector. $\bar{q}_c = \alpha_c / \lambda$ is the spatial frequency of the interference fringes, and α_c is the deflection angle between the incident reference wave and specimen plane wave.

The process of electron hologram reconstruction is illustrated in Figure 2.2. The Fourier transform of the hologram gives the expression [8]:

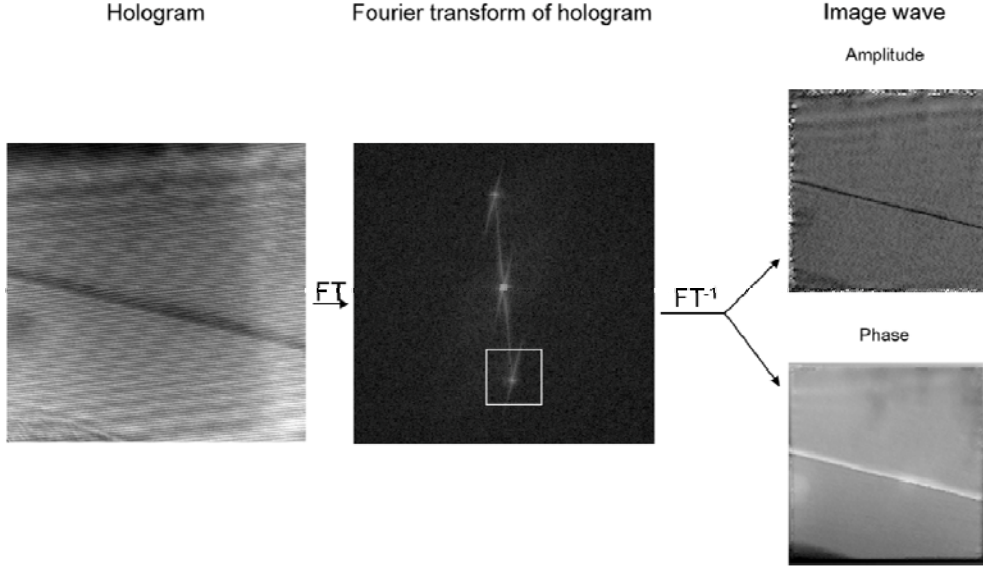


Figure 2.2 The schematic illustrating the procedure for reconstructing the electron hologram. The original hologram is Fourier-transformed to obtain three different bands, one of the side bands is cut out, re-centered, and inverse-Fourier-transformed to retrieve the complex image wavefunction, from which the corresponding amplitude and phase images can be obtained.

$$\begin{aligned}
 FT\{I_h(\vec{r})\} &= \delta(\vec{q}) + FT(A^2) && \text{center band} \\
 &+ \mu \cdot FT(A(\vec{r})\exp(i\phi(\vec{r}))) \otimes \delta(\vec{q} - \vec{q}_c) && + (\text{side band}) \\
 &+ \mu \cdot FT(A(\vec{r})\exp(-i\phi(\vec{r}))) \otimes \delta(\vec{q} + \vec{q}_c) && - (\text{side band})
 \end{aligned} \quad (2.3)$$

The central band corresponds to the conventional image intensity, often referred to as the auto-correlation function. Information about phase and amplitude is contained in the “+” and “-” side bands, which are complex conjugates of each other, and their separation depends primarily on the voltage applied to the biprism.

The distribution of intensities around these spots reflects any local phase shifts caused by the sample. For reconstruction purposes, one of the two side bands is cut out and re-centered around $\vec{q} = \vec{0}$. After an inverse Fourier transform, the complex image wavefunction is then obtained as:

$$I_{complex}(\vec{r}) = \mu \cdot A(\vec{r}) \exp(i\phi(\vec{r})) \quad (2.4)$$

The phase and amplitude of the complex image are given by:

$$phase = \arctan(i / r) = \phi(\vec{r}) \quad (2.5)$$

$$amplitude = \sqrt{r^2 + i^2} = \mu \cdot A(\vec{r}) \quad (2.6)$$

where r and i are the corresponding real and imaginary parts of the complex wavefunction.

The electron wave that passes through the sample will be modulated by the mean inner potential of the material. When the electron is attracted by the electrostatic field, the phase of the exit plane wave exceeds that of the vacuum reference wave; if it is repulsed by the electrostatic field, the phase of the exit plane wave will lag behind. An electron wave that passes through a magnetic material will be affected by the Lorentz force, which would also result in phase changes taking place.

The phase shift of the electron wave that passes through the sample, relative to the wave that only transmits in vacuum, is given (in one dimension) by:

$$\phi(x) = C_E \int V(x, z) dz - \frac{e}{\hbar} \iint B_{\perp}(x, z) dx dz \quad (2.7)$$

where z is along the incident beam direction, x is in the plane of the sample, V is the mean inner potential, and B_{\perp} is the component of the magnetic induction

perpendicular to both x and z . The interaction constant is dependent on the energy of the incident electron beam, and is given by:

$$C_E = \frac{2\pi}{\lambda E} \frac{E + E_0}{E + 2E_0} \quad (2.8)$$

where λ is the wavelength of incident electron wave, and E and E_0 are the kinetic and rest mass electron energies, respectively. For an electron energy of 200 keV, C_E has the value of 0.00728 rad/(V·nm).

For situations where neither V nor B vary within the sample thickness t along the incident beam direction, and if the electric or magnetic fringing fields outside the sample can be neglected, the relative phase shift can be simplified to:

$$\phi(x) = C_E V(x)t(x) - \frac{e}{\hbar} \int B_{\perp}(x)dx \quad (2.9)$$

A schematic illustration of the origins of phase shifts from electrostatic and magnetic fields is presented in Figure 2.3 [5].

In electron holography analysis, the sample thickness is usually obtained from the reconstructed amplitude image using the method proposed by McCartney [9]. The intensity distribution of an electron wave after passing through a sample is given by:

$$I_{tot} = I_u + I_e + I_i \quad (2.10)$$

where I_{tot} , I_u , I_e and I_i are the total, unscattered, elastic and inelastic scattering intensity, respectively. It is well established in Electron Energy Loss Spectroscopy (EELS) [10] that the thickness of the sample can be related to the inelastic intensity and the total incident intensity by the following expression:

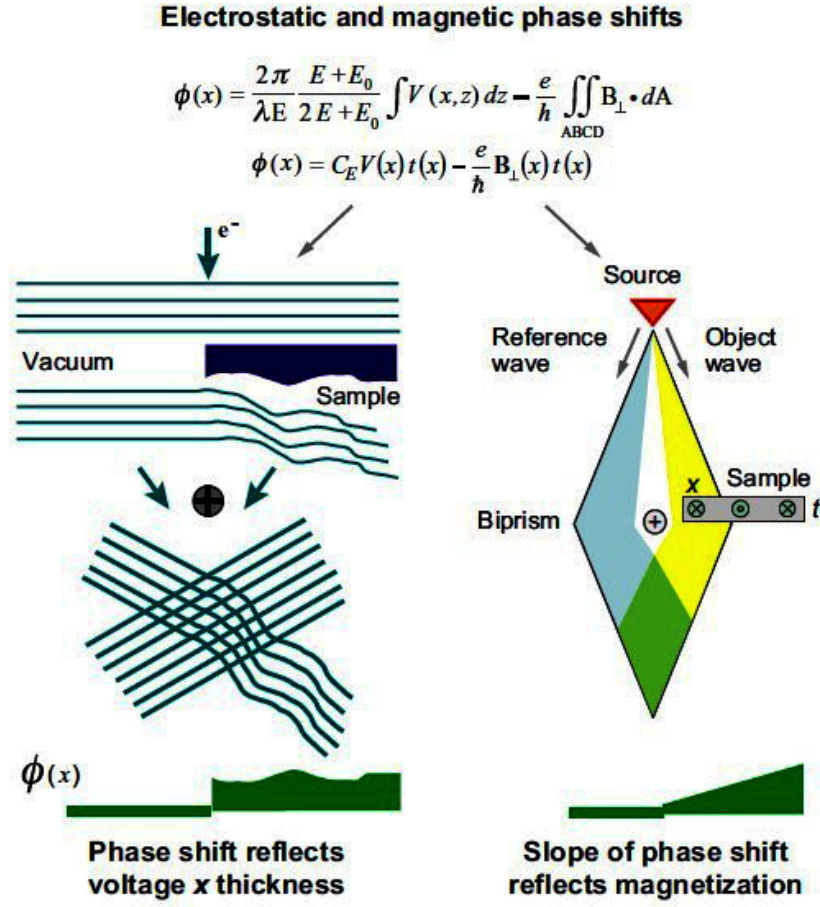


Figure 2.3 Schematic illustration of the origins of holographic phase shifts due to electrostatic and magnetic fields [5].

$$t / \lambda_i(\beta) = \ln(I_{tot} / I_{zero}) = \ln[I_{tot} / (I_{tot} - I_i)] \quad (2.11)$$

where β is the incident semi-angle of the scattering and $\lambda_i(\beta)$ represents the angular dependence of the inelastic mean free path.

In the off-axis holographic technique, two coherent electron waves are superimposed by means of a Möllenstedt biprism, to give the hologram intensity as:

$$\begin{aligned} H &= \left| \psi_{ref} + \psi_{obj} \right|^2 + B \\ &= A_r^2 + A_0^2 + 2A_r A_0 \cos(\phi_r - \phi_0) + B \end{aligned} \quad (2.12)$$

where H is the hologram intensity, $\psi_{ref} = A_r e^{i\phi_r}$ is the reference wave, $\psi_{obj} = A_0 e^{i\phi_0}$ is the modulated object wave, and B is the background intensity.

If the sideband (sb) of the Fast Fourier Transform (FFT) of the hologram associated with the cosine term is extracted, the modulus of its inverse FFT becomes:

$$\text{mod(sb)} = A_r A_0 \quad (2.13)$$

where A_r is a constant and A_0 is the energy-filtered amplitude. If the off-axis hologram contains vacuum at the edge of the sample, or if a hologram is obtained at identical illumination conditions by removing the sample from the field of view, the mean value for the reference image is:

$$\text{mod(sb)}|_{vac} = A_r^2 \quad (2.14)$$

Equation (2.11) is then transformed to:

$$t / \lambda_i = -2 \ln \{ \text{mod(sb)} / \text{mod(sb)}|_{vac} \} = -2 \ln(A_0 / A_r) \quad (2.15)$$

Thus, the sample thickness can be calculated based on the relative amplitude (A_0/A_r) provided that the inelastic mean free path λ_i for the specific material is known.

2.1.4 Mean inner potential

The mean inner potential (MIP) of a solid is defined as “measure of the volume-average electrostatic potential of a solid arising from incomplete screening of atomic cores”, which is mainly determined by the structure and composition of the specimen [11]. The MIP value is negative and usually in the range of -5~ -30V. The MIP has several important meanings that are related to physical properties of the material. For example, the MIP is the zero-order Fourier coefficient of the crystal potential for infinitely large perfect crystals. It is usually taken as the *ad hoc* zero of the crystal potential, and it is proportional to the second moment of the charge density for an atom [12-13]. The MIP for a crystal depends on the sum of dipole and quadrupole moments in the unit cell [14].

According to the definition of MIP, the general expression for MIP can be expressed as:

$$V_0 = \frac{1}{\Omega} \cdot \int_{\Omega} V(\vec{r}) d\vec{r} \quad (2.16)$$

where Ω is the volume of the unit cell for a perfect crystal, or the volume of the material for a disordered solid.

For theoretical determination of the MIP of a material, the simplest approximation is the non-binding approximation, which treats the solid as if it consisted of an array of neutral free atoms. The MIP is then related to the atomic scattering amplitudes as in the following [15-16]:

$$V_0 = \frac{h^2}{2\pi m_0 e \Omega} \cdot \sum_j f_j(0) \quad (2.17)$$

where $f_j(0)$ are the atomic scattering amplitudes for forward scattered electrons, and the sum is over the j atoms in the unit cell. The non-binding approximation generally overestimates the value of MIP since it ignores the redistribution of valence electrons due to bonding.

According to Radi [17], the non-binding approximation should be treated as an upper limit of the actual value for MIP, and a lower limit is obtained by treating the crystals as ions at the lattice points, while the valence electrons are distributed uniformly. The MIP is then expressed as:

$$V_0 = -\frac{3}{10} \cdot \frac{ep}{4\pi\epsilon_0 r_0} \quad (2.18)$$

The contribution of p perfect free electrons to V_0 has been given by Bethe [18], and the sphere of radius r_0 should have the same volume as the crystal atom.

Ross and Stobbs [19] have proposed an empirical rule for the compromise between the upper and lower limits of MIP. V_0 (*Doyle and Turner*) refers to the non-binding approximation using the Doyle-Turner scattering amplitudes of free neutral atoms [20]. V_0 (*Radi*) refers to the above-mentioned lower limit approximation proposed by Radi. The ratio between these two values follows a phenomenological dependence:

$$\frac{V_0(Radi)}{V_0(Doyle\ and\ Turner)} = 0.0325Z/\Omega + 0.6775 \quad (2.19)$$

Thus, by calculating V_0 using the non-binding approximation, and applying Equation (2.19), the value V_0 including the effect of binding can be easily calculated [11].

2.2 Scanning Transmission Electron Microscopy

Imaging in the conventional transmission electron microscope (TEM) can be considered as a two-step process: namely, scattering of the incident electron beam by the sample, and image formation by the imaging system, also applying the transfer function [21]. In scanning transmission electron microscopy (STEM), incoherent images can be obtained using inverted optical arrangements from that used in TEM.

A schematic illustrating the essential components needed for the STEM technique is shown in Figure 2.4. A partial plane wave in the cone of the coherent illumination is focused by the objective lens to form the electron probe incident on the specimen. The ideal electron probe is infinitesimally small and has very large probe current. In practice, electron probe sizes are in the range of 0.1~1 nm in diameter, and usually contain up to 1 nano-ampere of current. The focused beam passes through the sample and is then scattered in all directions. The transmitted beam can be used to form bright-field images, which resemble the normal high-resolution TEM images, or pass through energy spectrometers from which energy-filtered images and the electron-energy-loss spectrum can be obtained. The high-angle scattered electrons are incident on the high-angle annular detector, and high-angle annular-dark-field (HAADF) images are obtained, where the intensity is directly related to the atomic number of the material. Meanwhile, X-rays are also produced due to inelastic scattering of electrons by the sample, allowing the technique of energy-dispersive X-ray spectroscopy (EDS) to be used for element identification.

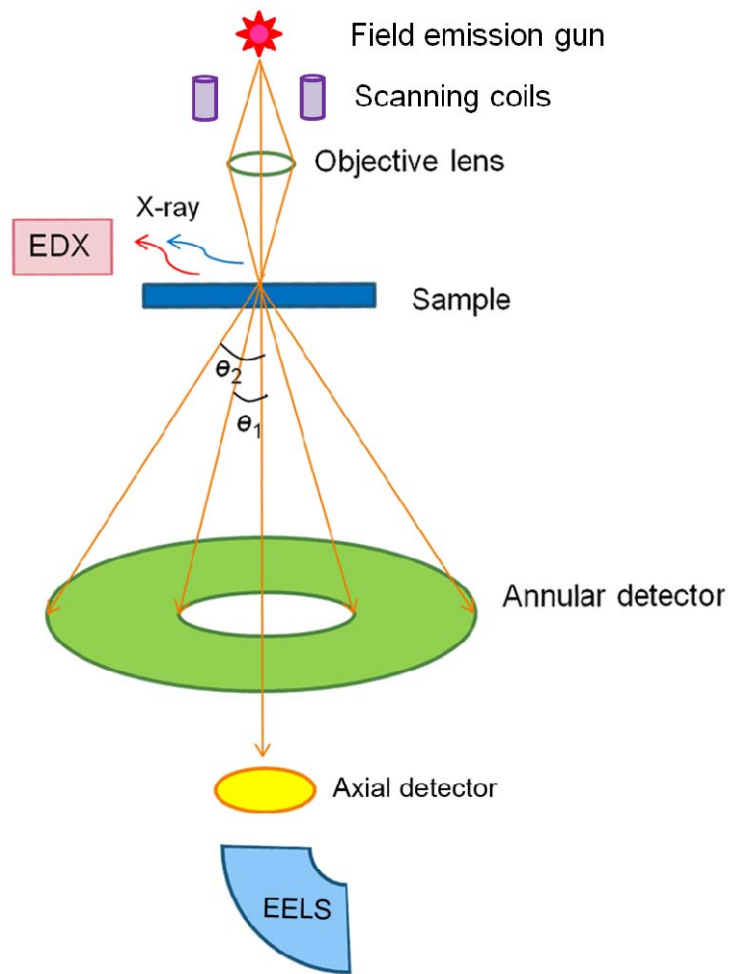


Figure 2.4 Schematic showing the essential components associated with the scanning transmission electron microscopy technique.

2.2.1 Energy-dispersive X-ray spectroscopy

When the high-energy incident electron beam interacts with inner shell electrons, those electrons may be ejected, leaving vacancies in the original shell locations. The excited outer shell electrons can then transit back to ground states with emission of X-rays. Thus, the corresponding energies of the emitted X-rays

carries characteristic information about the chemical species of the specimen. In addition to these characteristic X-rays, X-rays generated through Bremsstrahlung induce a continuous background in the X-ray spectrum, which must be removed before quantitative analysis can be carried out.

The spatial resolution of EDS is mainly determined by the probe size and the interaction volume within the sample, but smaller probe sizes correspond to lower counts. Although increasing acquisition time can alleviate this problem, specimen drift can seriously deteriorate the quality of the output. Thus, EDS has not generally been considered as suitable for sub-nanometer analysis [22].

The EDS technique can not only be used for obtaining spectrum for individual points, but also for two-dimensional elemental mapping or one-dimensional profiling of specific elements by scanning the electron probe across the specimen. The resultant mapping or profiling is then directly related to the spatial distribution of the selected element. This approach is widely used for determining the compositional structure of unknown materials.

2.2.2 High-angle annular-dark-field imaging

The phase shift factor for the objective pre-field with spherical aberration included can be expressed as [23]:

$$\chi(\theta) = \frac{2\pi}{\lambda} \left(-\frac{1}{2} \Delta f \theta^2 + \frac{1}{4} C_s \theta^4 + \dots \right) \quad (2.20)$$

The electron wavefunction at position x_p can then be expressed as [24]:

$$\psi_p(x, x_p) = A \int_0^{u_{\max}} \exp[-i\chi(u) - 2\pi i u(x - x_p)] d^2 u \quad (2.21)$$

where $u = \theta/\lambda$. Integration over the azimuthal angles gives an expression for the radially symmetric probe current distribution:

$$P(r) = A \left| \int_0^{u_{\max}} \exp[-i\chi(u)] J_0(2\pi u r) u du \right|^2 \quad (2.22)$$

If a crystal is oriented along a high symmetry zone axis, and the electron probe size is smaller than the spacing of individual atomic columns within the specimen, then atomic-resolution high-angle annular-dark-field (HAADF) images can be obtained. For a thin and weakly scattering object, the electron probe can be assumed to be an incident wave packet of amplitude $\Psi_p(R)$. For a sufficiently high-angle detector, the intensity measured in the annular dark-field detector $I(r_0)$ can be expressed as:

$$I(r_0) = c^2 \int \underbrace{[V^2(r') * D(r')]}_{\text{Object-detector term}} \underbrace{\psi_p^2(r' - r_0)}_{\text{Probe function}} dr' \quad (2.23)$$

where $D(r')$ is the Fourier transform of the detector function $d(u)$, which is unity over the detector region and zero elsewhere.

The function $d(u)$ has non-zero values only for very large values of u , and only the higher-order Fourier components of the objective potential contribute to the intensity in the HAADF image. Thus, the first term represents the potential of the atomic cores V'_{core} , and the second term is just the probe current distribution $P(r)$:

$$I(r_0) = c^2 \int V'_{\text{core}} P(r' - r_0) dr' = V'_{\text{core}} * P(r) \quad (2.24)$$

Equation (2.24) indicates that the HAADF image is just the convolution of the probe with the projected atom cores [25].

The Z-contrast imaging method was originally developed by Crewe and co-workers [26-27], who realized that an annular detector would collect a large fraction of the elastically scattered electrons with a total elastic scattering cross-section proportional to $Z^{3/2}$, whereas an axial electron spectrometer could detect a large fraction of the total inelastic scattering for small thicknesses, giving a signal proportional to thickness and showing only $Z^{1/2}$ dependence.

To exclude any contributions from diffraction contrast, Treacy and colleagues later suggested using an annular detector with a large inner collection angle since electrons scattered at high angles are incoherent, and diffraction contrast is lost [28]. In fact, the high-angle scattered electrons experience very small impact parameters, the scattering process is largely unscreened, and the corresponding cross-section resembles the Z^2 dependence of Rutherford scattering [29].

In practical cases, the image intensity can be expressed in the form $I \sim Z^\nu$, where ν is always smaller than 2 due to the atomic electron cloud screening of the Coulomb potential of the bare nucleus. In common cases, the value for ν is in the range between 1.6 and 1.9 depending on the inner and outer detection angles θ_1 and θ_2 [30], as illustrated in Figure 2.4. The plot for the θ dependence of the ν value is shown in Figure 2.5.

2.3 Sample Preparation

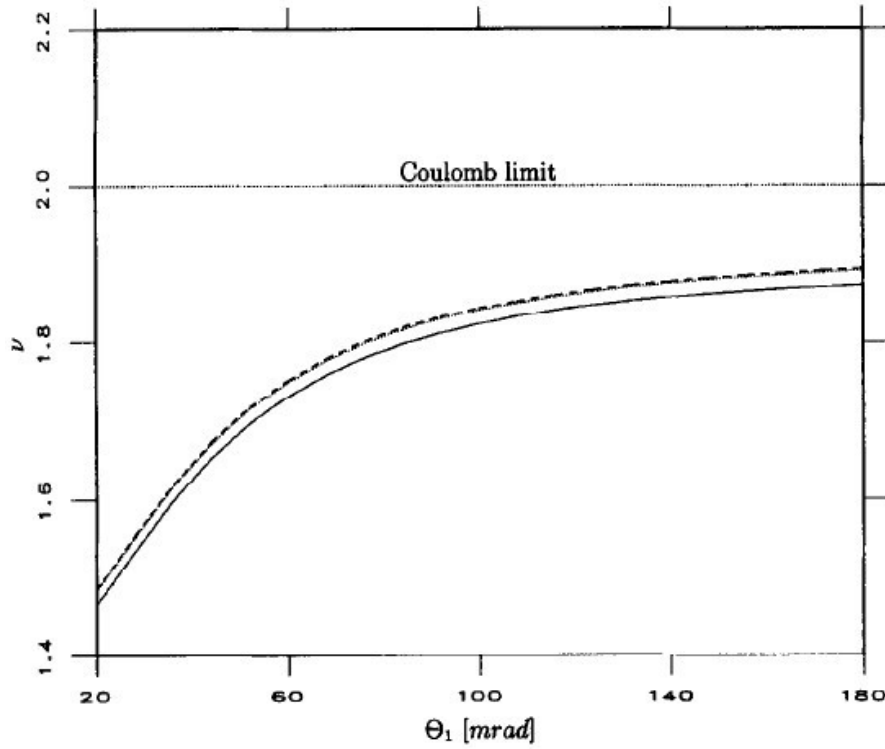


Figure 2.5 The parameter ν as a function of the inner detector angle for outer detector angles = 0.2 rad (solid line), 0.5 rad (dotted line) and 1.0 rad (dashed line), respectively [30].

In the research described in this dissertation, only wedge polishing has been utilized for sample preparation. By deliberately introducing a small angle ($\sim 2^\circ$) during polishing, a wedge-shaped sample can be obtained with the front edge representing the thinnest region. The angle adjustment is realized by adjusting the left front micrometer and the right rear micrometer to tilt the angle adjustment plate by certain amounts. The sample attached to the glass stub is fixed to be at

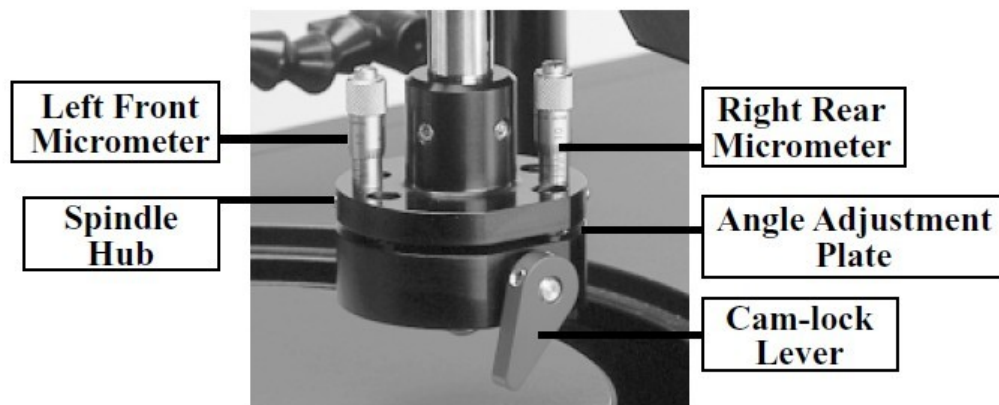


Figure 2.6 Image of the angle adjustment plate of the MultiPrepTM polishing device [31].

the bottom through the cam-lock lever, and can be tilted accordingly with the angle adjustment plate, as shown in Figure 2.6. The sample is directly polished to electron transparency by applying diamond lapping films of decreasing grain sizes, and any scratches on the sample surface are finally removed through cloth polishing. No ion-milling is applied at any time to avoid any possible ion implantation or uneven thicknesses. The MultiPrepTM apparatus of Allied High Tech Products has been utilized for this wedge polishing [31].

REFERENCE

- [1] D. Gabor, Proc. R. Soc. A **197**, 454 (1949).
- [2] A. V. Crewe, M. Isaacson, and D. Johnson, Rev. Sci. Inst. **40**, 241 (1969).
- [3] A. Tonomura, Rev. Mod. Phys. **59**, 639 (1987).
- [4] W. J. de Ruijter, Micron **26**, 247 (1995).
- [5] M. R. McCartney and D. J. Smith, Annu. Rev. Mater. Res. **37**, 729 (2007).
- [6] J. M. Cowley, Ultramicroscopy **41**, 335 (1992).
- [7] D. J. Smith and M. R. McCartney, Introduction to Electron Holography, Chapter 4, Kluwer Academic/Plenum Publishers, New York (1999).
- [8] H. Lichte, P. Formanek, A. Lenk, M. Linck, C. Matzeck, M. Lehmann, P. Simon, Annu. Rev. Mater. Res. **37**, 539 (2007).
- [9] M. R. McCartney and M. Gajdardziska-Josifovska, Ultramicroscopy, **53**, 283 (1994).
- [10] R. F. Egerton, Electron Energy-Loss Spectroscopy in the Electron Microscopy, Plenum Press, New York (1986).
- [11] M. Gajdardziska-Josifovska and A. H. Carim, Introduction to Electron Holography, Chapter 12, Kluwer Academic/Plenum Publishers, New York (1999).
- [12] S. Miyake, Proc. Phys.-Math. Soc. Japan **22**, 666 (1940).
- [13] J. A. Ibers, Acta Cryst. **11**, 178 (1958).
- [14] P. Becker, Acta Cryst. **A46**, 254 (1990).
- [15] L. Reimer, Transmission Electron Microscopy, Springer, Berlin (1989).
- [16] J. C. H. Spence and J. M. Zuo, Electron Microdiffraction, Plenum Press, New York (1992).
- [17] G. Radi, Acta Cryst. A **26**, 48 (1995).
- [18] H. Bethe, Ann. Phys. **87**, 55 (1928).

- [19] F. M. Ross and W. M. Stobbs, *Phil. Mag.* **63**, 37 (1991).
- [20] P. A. Doyle and P. S. Turner, *Acta Cryst.* **A24**, 390 (1968).
- [21] D. B. Williams and C. B. Carter, *Transmission Electron Microscopy*, Plenum Press, New York and London (1996).
- [22] Y. Lei, Ph. D. dissertation, University of Illinois at Chicago (2003).
- [23] D. J. Smith, *Fundamentals of High Resolution Transmission Electron Microscopy*, in “Surface and Interface Characterization by Electron Optical Methods”, Plenum Publishing Corporation, New York (1988).
- [24] E. J. Kirkland, *Advanced Computing in Electron Microscopy*, Plenum Press, New York (1998).
- [25] P. D. Nellist and S. J. Pennycook, *Ultramicroscopy* **78**, 111 (1999).
- [26] A. V. Crewe and J. Wall, *J. Mol. Biol.* **48**, 375 (1970).
- [27] A. V. Crewe, J. P. Langmore and M. S. Isaacson, *Physical Aspects of Electron Microscopy and Microbeam Analysis*, Wiley, New York (1975).
- [28] M. M. J. Treacy, A. Howie and C. J. Wilson, *Philos. Mag. A* **38**, 569 (1978).
- [29] S. J. Pennycook, *Ultramicroscopy* **30**, 58 (1989).
- [30] P. Hartel, H. Rose and C. Dinges, *Ultramicroscopy* **63**, 93 (1996).
- [31] The MultiPrepTM operating manual of Allied High Tech Products, Inc.

Chapter 3

STUDY OF HOLE ACCUMULATION IN INDIVIDUAL GERMANIUM QUANTUM DOTS IN P-TYPE SILICON

This chapter describes the study of hole accumulation in individual Ge quantum dots embedded in *p*-type Si substrates. The samples were grown by molecular beam epitaxy utilizing the Stranski-Krastanov growth mode, and were provided by Dr. S. Ketharanathan and Professor Jeff Drucker of Arizona State University. My role in this work involved preparation of specimens using wedge polishing and characterization of hole density using off-axis electron holography. The major results of this study have been published [\[1\]](#).

3.1 Introduction

The Ge/Si (100) system is considered to be a prototype for investigating strained-layer heteroepitaxy [\[2\]](#), as well as being a prominent candidate for device applications [\[3-5\]](#). Epitaxial Ge/Si (100) growth follows the Stranski-Krastanov (S-K) growth mode with about 3 atomic layers of pseudomorphic growth of Ge followed by the formation of three-dimensional (3D) Ge quantum dots (QDs). When encapsulated in an Si matrix, the electronic structure of the Ge QDs exhibits a staggered type-II band lineup, and the large (~ 0.7 eV) valence-band offset leads to the confinement of holes in the Ge dot [\[6\]](#).

3.1.1 Hut, pyramid and dome structures

Both Ge and Si have the diamond-cubic crystal structure consisting of two interpenetrating face-centered-cubic (fcc) Bravais lattices, displaced along the body diagonal direction by 1/4 of the total length of the diagonal. This geometry is illustrated in Figure 3.1. Ge has a larger lattice constant than Si ($a_{\text{Ge}} = 5.65\text{\AA}$, $a_{\text{Si}} = 5.43\text{\AA}$), and thus there is a misfit ε between the two lattices, which can be defined as:

$$\varepsilon = \frac{a_{\text{Ge}} - a_{\text{Si}}}{a_{\text{Si}}} = 4.2\% \quad (3.1)$$

As mentioned above, the epitaxial growth of Ge/Si (100) system follows the S-K scheme: the first three monolayers (ML) (1ML refers to the bulk-terminated Si (100) surface = $6.78 \times 10^{14} \text{ atoms/cm}^2$) of deposited Ge grow on Si substrate forming a flat wetting layer (WL), while subsequent growth of Ge accommodates into 3D islands in order to relieve the strain due to the 4.2% lattice mismatch [7].

The growth of the Ge islands starts with formation of small 2D platelets on the 3ML wetting layer: these platelets are basically ‘prepyramid’ Ge islands

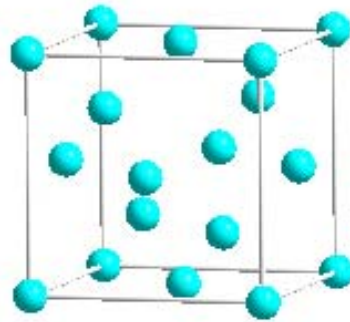


Figure 3.1. Diamond crystallographic structure of Ge and Si.

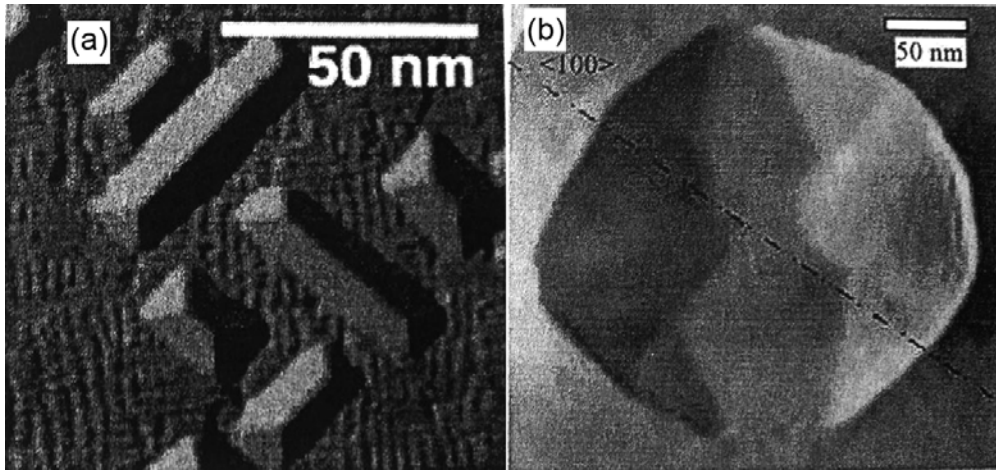


Figure 3.2. (a) Elevated temperature STM image of hut and pyramid structures [10]. (b) Image of Ge multifaceted dome structure obtained using AFM [14].

with steps orientated along $\langle 110 \rangle$. These have a lower aspect ratio than $\{105\}$ faceted pyramids, and they normally exist between 3.5~4.0ML of Ge coverage [8]. These non-faceted clusters increase their aspect ratio with additional Ge coverage, and eventually form $\{105\}$ faceted pyramids.

The faceted islands that form right after these 2D platelets, are bounded by four $\{105\}$ planes which have contact angles of 11.3° with the substrate plane. These islands are either rectangular-based, prism-shaped ‘huts’ or square-based ‘pyramid’ shape, and the principal axes are strictly along two orthogonal $\langle 100 \rangle$ directions [9]. The Scanning Tunneling Microscopy (STM) image shown in Figure 3.2(a) illustrates the typical morphology of these huts and pyramids [10]. It is assumed that these hut and pyramid structures are metastable phases that provide an easier and faster way to accommodate arriving atoms than direct

nucleation of 3D clusters, also indicating that the formation barrier is lower for huts and pyramids than 3D clusters. Moreover, the hut structure has been observed to transform into the pyramid structure during annealing [11].

Beyond 5ML of Ge coverage, huts and pyramids are replaced by 3D domes. The dome structure is octagonal-based and multifaceted, and the facets make a contact angle of $\sim 25^\circ$ with the base, which is steeper compared to huts or pyramids [2]. The dome facets that intersect the (001) surface along $\langle 110 \rangle$ are $\{113\}$, those that intersect along lines close to $\langle 100 \rangle$ are assumed to be $\{15\ 3\ 23\}$, although other possibilities such as $\{5\ 1\ 8\}$ or even $\{1\ 0\ 2\}$ have been suggested by some investigators [12-13]. The Atomic Force Microscopy (AFM) image of a typical dome structure is shown in Figure 3.2(b) [14]. As the Ge coverage is increased to 7ML, the smaller coherent domes transform to larger incoherent domes, which are also known as dislocated domes. Once a dislocation has formed in a dome, the chemical potential of the dome decreases, resulting in an increase of the island growth rate [15-16].

3.1.2 Composition and shape transition for capped Ge quantum dots

The interdiffusion of Si into the Ge QDs is inevitable using the current MBE growth method (the method will be introduced in detail in the next section), and the composition of Ge in contrast to Si (X_{Ge}) depends on several growth conditions, among which growth temperature and deposition rate are more responsible for the X_{Ge} change. X_{Ge} decreases, and the Ge/Si interface becomes

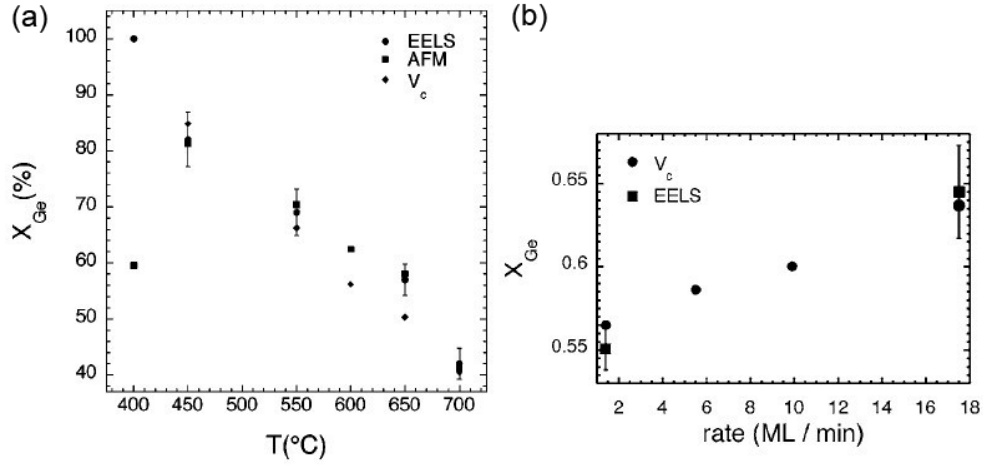


Figure 3.3 (a) The average Ge concentration in dome structure vs substrate temperature [17]. (b) Ge concentration in dome structure vs deposition rate [18].

more diffuse, as the growth temperature is increased from 400 to 700°C, as shown in Figure 3.3(a) [17]. On the other hand, the value of X_{Ge} increases with deposition rate, and is controlled by the ratio between the Ge deposition and Si interdiffusion rates, as shown in Figure 3.3(b) [18].

The octagonal-base multifaceted model mentioned above is for uncapped dome structures, whereas the top of the dome is suppressed when the Ge QDs are capped with Si layers, and the shape transforms into flat truncated pyramids. The angle between the side facets and the base is decreased to 16°. The structural model for capped Ge QDs is shown in Figure 3.4 [19].

3.1.3 Electron charging behavior of Ge quantum dots

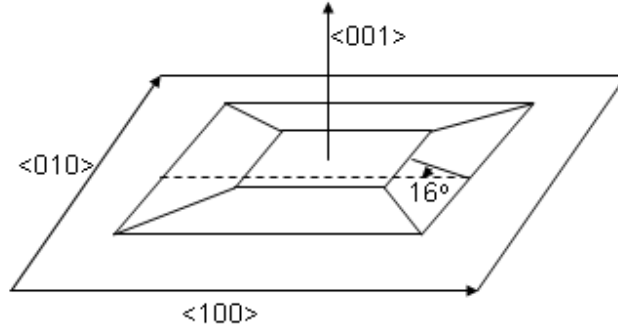


Figure 3.4 Schematic of the flat, truncated-pyramid island model.

Ge QDs embedded in n-type Si substrate were incorporated into Schottky diodes to investigate their charging behavior using capacitance-voltage (C-V) measurements [20]. The results are as follows: electrons are confined to the strained region adjacent to the Ge QDs. Huts and pyramids in the range of 20-40 nm in diameter confine ~ 0.7 electron per dot; domes in the range of 60-80 nm in diameter confine ~ 6 electrons per dot [20]. Theoretical calculations based on path-integral Monte Carlo simulations were also performed giving different results: pyramids of 40 nm in diameter confine ~ 0.4 electrons per dot and domes in the range of 70-80 nm in diameter confine $\sim 2.2-3$ electrons per dot [21]. However, experimental results based on C-V measurements can only give electron charging averaged over a large number of QDs, while conditions of electron charging would be different for QDs of slightly different sizes. Theoretical simulations can be performed on a single dot, but several uncertainties and approximations exist, which could induce appreciable deviation from the

experimental conditions. Electron holography, which is based on measurement of the relative phase shift, could potentially give information about electron charging from a typical individual quantum dot, and would then be a prominent method for studying charging induced by strain and band-edge alignment.

3.2 Experimental Details

The self-assembled Ge QDs were grown on Si (100) substrates using molecular-beam epitaxy (MBE) [20]. For *n*-type Ge QDs, the QDs were grown to a coverage of ~ 7.8 ML using a growth rate of 3.0 ML/min. The growth temperatures were set at 550°C for huts and pyramids, and 600°C for domes. There were two intrinsic spacer layers of thickness 60 nm below and above the Ge dot layer, a 10^{16} cm^{-3} Sb-doped Si spacer layer of thickness 100 nm below, and a 10^{16} cm^{-3} Sb-doped Si cap layer of thickness 340 nm on the top [20]. The *p*-type Ge QDs were grown with a Ge coverage of 8.4 ML at a substrate temperature of 550° using a growth rate of 1.2 ML/min. Under these growth conditions, most QDs should be either huts or pyramids that are bound by {105} facets, with diameters near 20 nm. Fewer dots would be much larger domes or dislocated domes bound by steeper facets. The Ge dots were sandwiched in a 10^{17} cm^{-3} B-doped layer that extended about 300 nm above and 100 nm below the Ge dots [1]. The schemes for the layered growth of the *n*-type and *p*-type Ge QDs on Si (100) substrate are shown in Figures 3.5 (a) and (b), respectively.

The samples were prepared for holography observation by wedge-polishing using a MultiPrepTM wedge-polishing apparatus, and a wedge angle of $\sim 2^\circ$ was

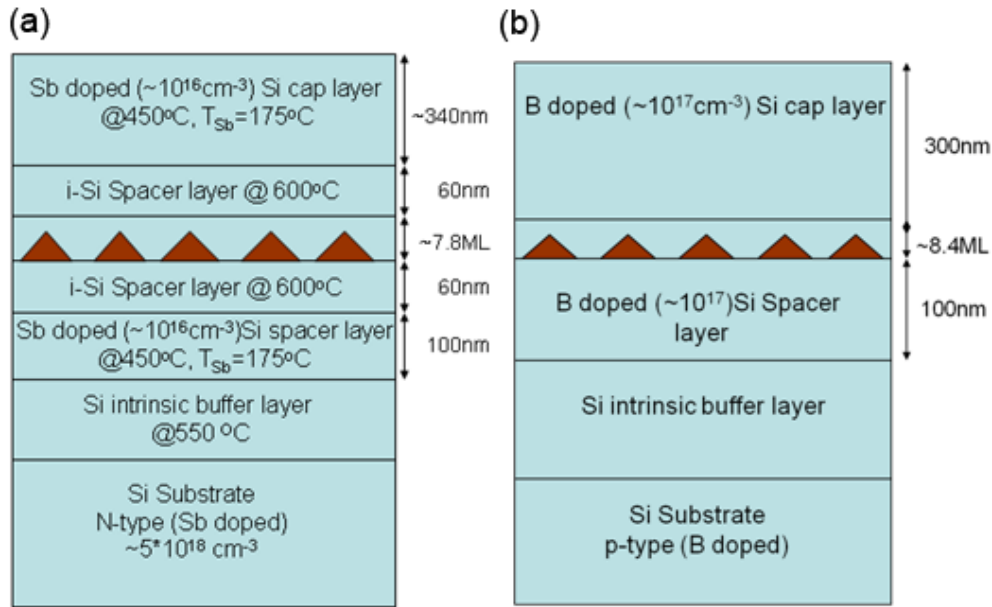


Figure 3.5 Schemes of layered growth for: (a) *n*-type; and (b) *p*-type; Ge QDs on Si (100) substrate.

introduced. No ion milling was used to avoid any possible ion implantation and uneven thickness. Before sample preparation, the top Si surface layer was etched away to leave only ~60 nm of the Si cap above the QD layer so that the region of interest would be close to vacuum, which is a necessary requirement for off-axis electron holography.

The off-axis electron holography analysis was performed using a Philips CM200-FEG transmission electron microscope (TEM) equipped with an electrostatic biprism and a 1024×1024 Gatan 794 charge-coupled device camera. The biprism bias voltage was set at ~35 V, and the magnification was ~200 kX

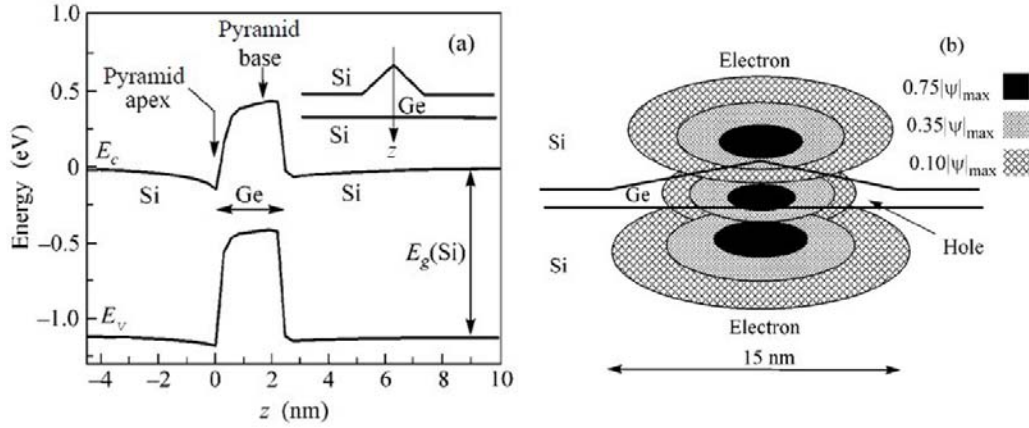


Figure 3.6 (a) Calculated profile of conduction and valence bands along the z axis [22]. (b) Calculated structure of the wave functions of two electrons and a hole localized in the vicinity of a Ge pyramid [23].

when the sample was imaged in the microscope diffraction mode but with the diffraction lens turned off.

3.3 Results and Discussion

3.3.1 Charge distribution in n -type and p -type Ge quantum dots

When encapsulated in an Si matrix, the electronic structure of the Ge QDs exhibits a staggered type-II band lineup, where the conduction band of Si is close to the valence band of Ge. The calculated profiles for conduction and valence bands along the z axis are shown in Figure 3.6 (a) [22], and the corresponding charge distributions are shown in Figure 3.6 (b). The holes are expected to be concentrated in Ge in the vicinity of the base of the pyramid due to the large valence band offset of $\sim 0.7\text{eV}$. The electrons are expected to be localized in Si

either in the vicinity of the apex of the Ge pyramids or near the boundary between Si and the Ge wetting layer due to comparatively large strain-induced conduction band bending in these regions [23].

Theoretical modeling of phase shift and projected potential distribution induced by charge accumulations at the QDs was performed for *n*-typed Ge QDs applying a path integral quantum Monte Carlo technique, and the results are shown in Figures 3.7 (a) and (b). The QD was assumed to be in the center of the supercell, and projected along the [110] direction. The negative phase shifts and projected potentials are located above and below the QD, indicating electron localization in these regions. The color bars on the right hand side give the maximum phase shift to be -4.5×10^{-3} rad, and the maximum projected potential to be -0.6 V·nm, which results from the accumulated electrons. Since the phase shift resolution for CM200 is limited to ~ 0.01 rad, it is quite possible that the weak signals from electron accumulation could not be identified under the current experimental conditions. Moreover, this calculation was performed at a temperature of 77K, and there are expected to be even less phase shifts due to electron accumulation at room temperature. (The calculations provided by S. Sinha from the group of Prof. J. Shumway at ASU)

In comparison, the valence band offset at the Si/Ge interface is much larger than the smaller dips due to band bending at the conduction band, as can be seen from Fig. 3.6 (a). Thus, it might be anticipated that there should be much higher density of holes accumulated in the Ge dots than electrons located in the peripheral Si layers.

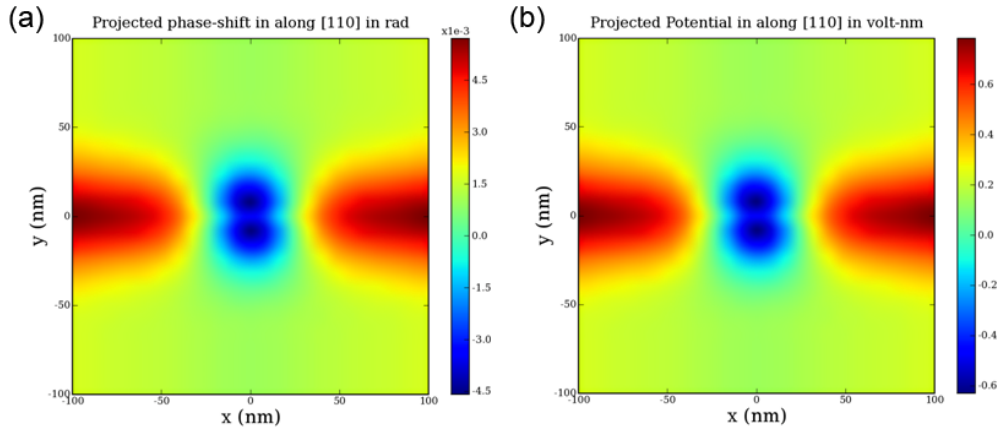


Figure 3.7 Theoretical modeling of: (a) phase shift distribution; and (b) projected potential distribution, induced by electron accumulation at *n*-type Ge QDs.

3.3.2 Electron holography study of *n*-type Ge quantum dots

The *n*-type Ge QDs were studied first by electron holography. Since the expected information was likely to be quite weak, as mentioned before, ten serial holograms of the same QD were obtained and carefully aligned in order to enhance the signal-to-noise level. Figure 3.8 (a) shows the reconstructed phase image, where the color bar has been added to indicate the magnitude of the phase shift at each point. The Ge QD region has a larger phase shift than the surrounding Si substrate due to the larger MIP of Ge than Si ($\text{MIP}_{\text{Ge}} = 14.3(2) \text{ V}$ [25], $\text{MIP}_{\text{Si}} = 12.0 \text{ V}$). The Ge wetting layer had an even greater phase shift than the dot region since the wetting layer has a larger projected thickness than the dot region, while the latter has decreasing thicknesses approaching the top. Figure 3.8 (b) is the corresponding thickness image. The regions below and above the QD

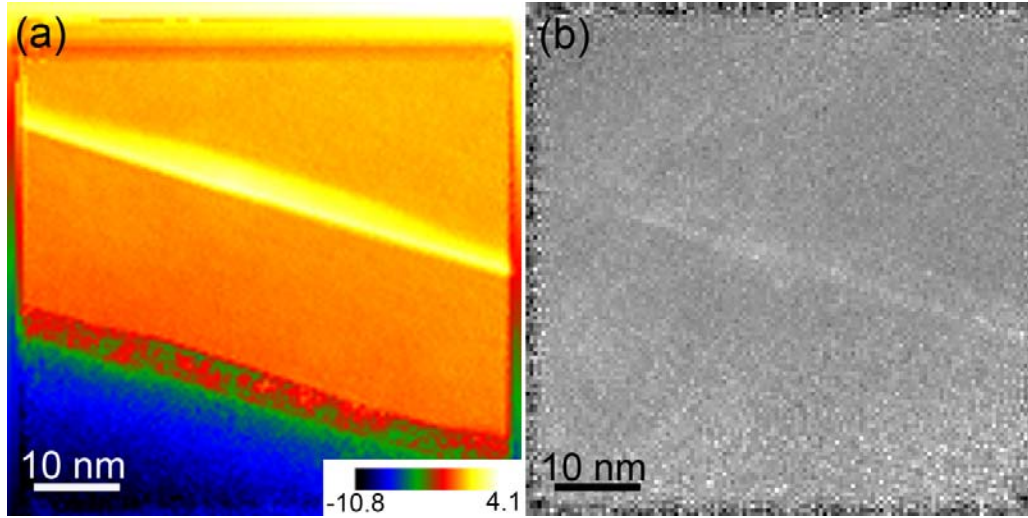


Figure 3.8 *n*-type Ge quantum dot studied by electron holography. (a) The reconstructed phase image averaged from ten serial holograms. (b) The corresponding thickness image.

are flat, indicating no serious thickness fluctuations and no diffraction contrast, which would otherwise contribute to the relative phase shift. Close inspection of the phase shift distribution just above the top of the Ge QD and at the interface region between the Ge wetting layer and underlying Si substrate reveals no abrupt changes. Based on this result, it is not appropriate to conclude that there was no electron accumulation in these regions, but rather that the signals were simply too weak to be detected under the current experimental conditions.

3.3.3 Electron holography study of *p*-type Ge quantum dots

Figure 3.9 (a) shows an electron hologram of an individual Ge/Si (100) QD, viewed in the [110] projection, on which the following reconstruction and calculations are based. The Si cap layer extends to ~50 nm above the dot, and the darker line corresponds to the Ge wetting layer. The sample was slightly tilted around the interface normal to avoid diffraction contrast, while the dot layer and the substrate surface were still kept edge-on. According to the growth temperature (550 °C) and QD size under study (base width: 25 nm), it is quite likely that the QD possesses square-based pyramidal shape. Figure 3.9 (b) is the sketch of the pyramid-shaped dot and wetting layer, with the locations of the line profiles in the following figures as indicated.

Figure 3.9 (c) shows the reconstructed phase image of the same Ge QD, and has been rotated so that the Ge/Si interface is horizontal. In order to improve the signal-to-noise ratio of the reconstructed phase image, ten individual phase images were averaged. The region occupied by the pyramidal QD is outlined in white. The apex appears to be somewhat flattened in the experimental phase image, which might be expected for capped QDs [18]. The phase bar at bottom right shows the relationship between color and phase shift in radians. Due to the larger MIP for Ge compared with Si, the 3D Ge dot and Ge planar wetting layer show larger phase shifts than the surrounding Si matrix.

The thickness of the sample cross-section in the beam direction was determined to be 100 ± 5 nm based on the holographic amplitude image. The maximum phase shift, relative to the Si matrix, within the wetting layer away

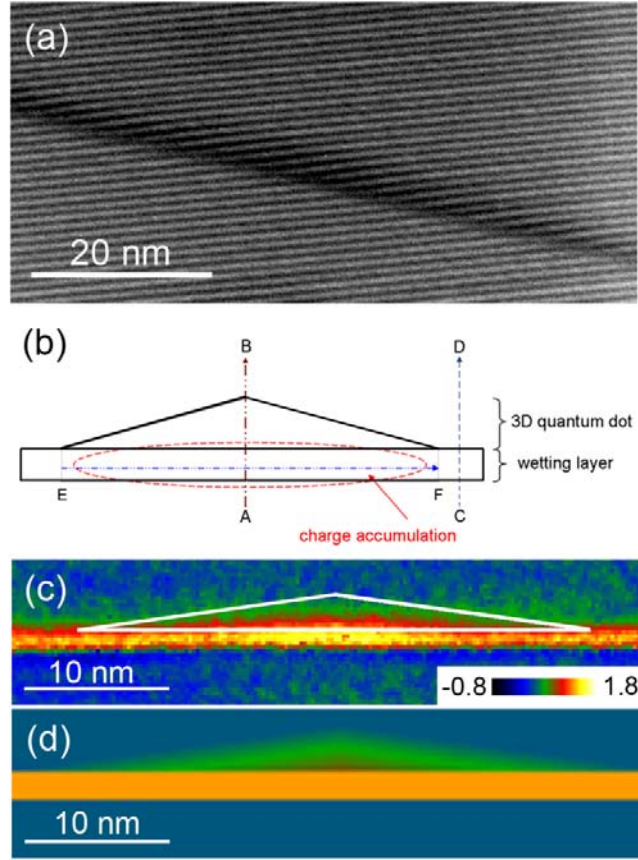


Figure 3.9 (a) Electron hologram of individual Ge QD, embedded in Si [001] substrate, recorded in [110] projection. (b) Sketch of the pyramid-shaped dot and wetting layer, with locations of line profiles in Fig. 3.10 indicated. (c) Reconstructed phase image of the Ge QD. Phase bar calibrated in radians shown at bottom right. (d) Simulated phase image of Ge QD based on the pyramid model sketched in (b), the same phase bar in (c) is applied [1].

from the QD indicated that its Ge content was near 70%, assuming that the MIP varied linearly with composition. This amount of Si intermixing during Ge

deposition is to be expected for these growth conditions [17], and may explain the unexpectedly large thickness of the Ge wetting layer.

Using the measured Ge concentration and the known shape of Ge(Si) pyramid clusters, the two-dimensional phase shift to be expected was calculated based on the SiGe thickness projected along the [110] beam direction, producing the model shown in Figure 3.9 (d). The experimentally measured pyramid base width of 25 nm was used.

By comparing Figures 3.9 (c) and (d), a region of excess positive phase shift is identified that appears centered below the pyramid apex, close to the base of the Ge(Si) dot. There are several possible reasons for excess phase shift to be observed at the dot base. Artifacts in holographic phase images could arise from strong diffraction features, especially those associated with extinction contours and thickness fringes. However, this excess phase shift was observed in several QDs without any visible strain or extinction contrast. Another scenario resulting in excess positive phase shift could be compositional inhomogeneities in this region. The maximum excess positive phase shift would be found if that specific region of the dot was comprised of pure Ge. However, this maximum value can account for only 1/3 of the excess phase found experimentally in Figure 3.9 (c). In what follows, it is assumed that the excess positive phase shift is due solely to positive charge, and the associated charge necessary to account for the experimentally observed excess is then calculated. In fact, accumulation close to the base of the island is expected. The 0.7 eV valence band offset leads to hole confinement in the Ge dot. The calculated band diagram indicates a slightly

higher energy at the bottom of the dot, corresponding to a higher probability of hole accumulation in the region of the pyramid base [22].

We begin by quantifying the excess shift. Figure 3.10 (a) shows a line profile from the bottom to the top of the QD. The red line with squares is the line profile, averaged over 10 horizontal pixels (1 pixel = 0.268 nm), from A to B, across the center of the dot, as sketched in Fig. 3.9 (b), and the blue line with open circles is the line profile from C to D in Fig. 3.9 (b) across the wetting layer only. It can be seen in this profile that the wetting layer has an abrupt onset, reaching a maximum value, and then decreasing gradually, suggesting increased Si content toward its top. Finally, the dark yellow line with triangles is the *difference* between phase shifts across the center of the dot and the wetting layer. The maximum excess phase shift of ~ 0.4 rad is visible close to the base of the dot. The line profile from A to B goes through the wetting layer (1.6 nm thick) below the dot and the whole dot to the top (which is 2.7 nm from the bottom). The line profile from C to D goes only through the wetting layer. Thus, the first 1.6 nm for both profiles shown in Fig. 3.10 (a) are measurements of the wetting layer, which goes through the entire thickness of the TEM sample. The extra phase shift visible in the first 1.6 nm of the difference profile is attributed to hole accumulation.

The black squares plotted in Figure 3.10 (b) represent a scan through the region of excess positive phase shift parallel to the Si/Ge interface along the line joining E and F, as shown in the schematic of Fig. 3.9 (b). The red line is a fit to a fourth-order polynomial from which the projected potential of accumulated holes

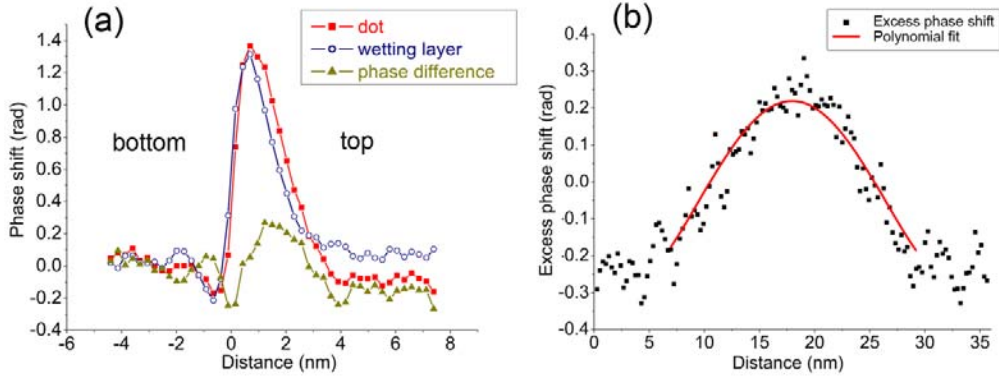


Figure 3.10 (a) Line profile from A to B in Fig. 3.9 (b), shown as red line with squares. Blue line with open circles is the line profile across wetting layer only from C to D, as indicated in Fig. 3.9 (b). The dark yellow line with triangles is the *difference* between phase shift across the dot center and across wetting layer only. (b) Line profile from E to F across the center of the accumulated charges with the average phase shifts for the wetting layer subtracted (excess phase shifts), as shown in Fig. 3.9 (b), the fourth-order polynomial fitting is overlapped in red [1].

can be obtained. It is assumed that the charge density occupies the entire base of the pyramid and the SiGe region below.

The projected thickness-averaged electrostatic potential V_{hole} due to the confined holes can be calculated using $V_{\text{hole}} = \phi_{\text{excess}}/(C_E t)$, where $C_E = 0.00728$ rad/ (V nm) for an accelerating voltage of 200 kV, t is the projected thickness of the pyramid along the incident electron beam and ϕ_{excess} is the measured excess phase shift due to the confined positive charge density [26]. The result shows a

maximum in the electrostatic potential due to the confined holes of about 1 V at the center of the dot, near 20 nm in Fig. 3.10 (b).

The one-dimensional Poisson equation allows the charge density to be obtained:

$$\rho_{hole} = -(\epsilon_0 \epsilon_r) \frac{d^2 V_{hole}(x)}{d^2 x} \quad (3.2)$$

where $\epsilon_0 = 8.854 \times 10^{-12}$ C/N m² and $\epsilon_r = 16.0$ (for Ge) [27]. ρ_{hole} is calculated for the range 12-26 nm and an average volume charge density of 0.03 /nm³ is found. Multiplying this average charge density by the volume over which the excess positive phase shift is observed in Fig. 3.9 (c), provides an estimate of the number of holes confined to this Ge(Si) pyramid cluster. Assuming that the holes occupy a volume that is 25 nm square and 1.6 nm thick, then a total confined charge of 5×10^{-18} C is obtained, corresponding to about 30 holes for this particular pyramid.

The error bars for the holographic measurement can be estimated as follows. The thickness of the area under study is determined to be 100 ± 5 nm from the holographic amplitude image using $\lambda_i = 85$ nm for Si. Note that care has been taken to avoid diffraction effects by slightly tilting the sample off the zone axis to minimize diffraction contrast. The standard deviation for fitting of the phase profile to the fourth-order polynomial is 0.054 rad, with $R^2 = 0.92$. Through error propagation, the standard deviation of potential is 0.18 V. Using a one-dimensional Poisson equation, the standard deviation of the number of holes is finally determined to be 3. Additionally, the simplified assumption of a uniform

distribution and a square box for the shape of the accumulated holes may result in an overestimate of the overall number of holes.

3.3.4 Comparison of hole density with C - V measurement

C - V measurements were performed using a standard lock-in technique with a 40 mV modulation voltage at 1 MHz [1]. Figure 3.11 displays the C - V curve obtained by incorporating the Ge QDs discussed above in a Schottky diode using a Ti Schottky gate and an Au Ohmic back contact [1]. The solid line is the experimental measurement and the dashed line is a simulated C - V curve for a device with identical B-doping levels without the Ge dot layer. The inset displays the valence-band at zero bias. As the reverse bias was increased, the Fermi energy was pinned at the dot level until the dots discharge, producing the experimental

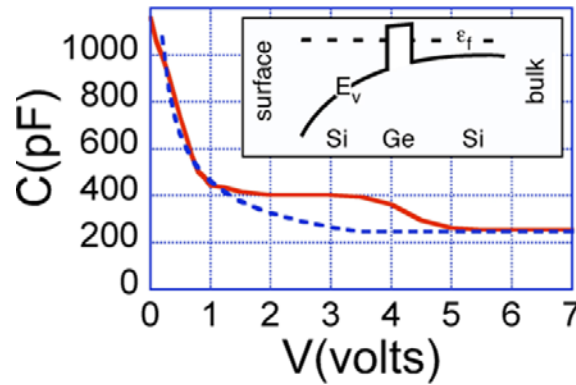


Figure 3.11 Experimental C - V plots in red with theoretical reference C - V plot of conventional p -type Schottky diode without any Ge dots shown in blue dashed line. Holes are discharged between 1-4 V. The inset displays the valence-band at zero bias [1].

capacitance plateau for $1 \text{ V} \leq V \leq 4 \text{ V}$. The difference between the experimental measurement and the simulated curve, ΔC , is related to the holes confined to the dots at zero bias [20] through $Q_{\text{dot}} = \int \Delta C dV$, giving $Q_{\text{dot}} = 3.4 \times 10^{-10} \text{ C}$. The average number of holes per dot is found using $N_h = Q_{\text{dot}} / (eAN_{\text{dot}})$ where e = electronic charge, A = contact area of the gate electrode ($1.13 \times 10^{-2} \text{ cm}^2$), N_{dot} = dot density ($5 \times 10^9 \text{ dots/cm}^2$, determined using atomic force microscopy on a similarly prepared sample that was not capped with Si). A value of $N_h \sim 40$ holes/dot was found, which agrees reasonably well with the value found using electron holography when considering potential sources of error in the two measurements. These include the noise inherent in the reconstructed phase image of Fig. 3.9 (c) and a significant contribution from a low density of very large dislocated dome clusters that were not sampled by the holography measurements. Although these clusters were present at very low density ($\sim 5 \times 10^8 \text{ dots/cm}^2$), their large sizes would represent a significant contribution to the average charge per dot in the ensemble. Thus, it is believed that the discrepancy between the two measurements points out the benefit of a technique such as electron holography that is capable of nanometer-scale charge density measurements.

3.4 Conclusions

Self-assembled Ge QDs grown on Si (100) have been studied by off-axis electron holography. The *n*-type Ge QDs were embedded in an Sb-doped Si matrix, and the *p*-type Ge QDs were embedded in a B-doped Si matrix.

Theoretical modeling of phase shift distributions induced by charge accumulation at the QDs was performed for the *n*-typed Ge QDs by applying a path integral quantum Monte Carlo technique. The maximum phase shift was -4.5×10^{-3} rad, which is considerably smaller than the attainable phase shift resolution using the CM200 (~ 0.01 rad). For *n*-type Ge QDs, the reconstructed phase shift just above the top of the Ge QD and the interface region between Ge wetting layer and underline Si substrate revealed no abrupt changes, indicating that the signals from electron accumulation was too weak to be detected by this microscope. For *p*-type Ge QDs, holes were found to be confined near the base of the pyramidal, 25-nm-wide Ge QDs. The resulting estimate of charge density was 0.03 holes/nm³, which corresponded to about 30 holes localized to the investigated dot. For comparison, the average number of holes confined to each Ge dot was found to be about 40, using a capacitance-voltage measurement. The difference emphasizes the value of using electron holography to measure charges confined to individual nm-scale regions of a heterogeneous sample.

REFERENCES

- [1] L. Li, S. Ketharanathan, J. Drucker and M. R. McCartney, Appl. Phys. Lett. **94**, 232108 (2009).
- [2] J. Drucker, IEEE J. Quantum Electron. **38**, 975 (2002).
- [3] T. Brunhes, P. Boucaud, S. Sauvage, F. Aniel, J. M. Lourtioz, C. Hernandez, Y. Campidelli, O. Kermarrec, D. Bensahel, G. Faini, and I. Sagnes, Appl. Phys. Lett. **77**, 1822 (2000).
- [4] A. I. Yakimov, A. V. Dvurechenskii, A. I. Nikiforov, and Y. Y. Proskuryakov, J. Apply. Phys. **89**, 5676 (2001).
- [5] P. S. Fodor and J. Levy, J. Phys.: Condens. Matter **18**, S745 (2006).
- [6] J. H. Seok and J. Y. Kim, Appl. Phys. Lett. **78**, 3124 (2001).
- [7] A. Rastelli, M. Kummer and H. von Känel, Phys. Rev. Lett. **87**, 256101 (2001).
- [8] A. Vailionis, B. Cho, G. Glass, P. Desjardins, D. G. Cahill and J. E. Greene, Phys. Phys. Lett. **85**, 3672 (2000).
- [9] Y. W. Mo, D. E. Savage, B. S. Swartzentruber and M. G. Lagally, Phys. Rev. Lett. **65**, 1020 (1990).
- [10] Y. T. Zhang, Ph. D. dissertation, Arizona State University (2002).
- [11] G. Medeiros-Ribeiro, T. I. Kamins, D. A. A. Ohlberg and R. S. Williams, Phys. Rev. B **58**, 3533 (1998).
- [12] R. S. Williams, G. Medeiros-Ribeiro, T. I. Kamins and D. A. A. Ohlberg, J. Phys. Chem. **102**, 9605 (1998).
- [13] F. M. Ross, R. M. Tromp and M. C. Reuter, Science **286**, 1931 (1999).
- [14] E. McDaniel, Ph. D. dissertation, Arizona State University (2005).
- [15] J. Drucker, Phys. Rev. B **48**, 18203 (1993).
- [16] M. Krishnamurthy, J. S. Drucker and J. A. Venables, J. Appl. Phys. **69**, 6461 (1991).

- [17] M. Floyd, Y. T. Zhang, K. P. Driver, J. Drucker, P. A. Crozier and D. J. Smith, *Appl. Phys. Lett.* **82**, 1473 (2003).
- [18] E. P. McDaniel, Q. Jiang, P. A. Crozier, J. Drucker and D. J. Smith, *Appl. Phys. Lett.* **87**, 223101 (2005).
- [19] O. G. Schmidt, K. Eberl and Y. Rau, *Phys. Rev. B* **62**, 16715 (2000).
- [20] S. Ketharanathan, S. Sinha, J. Shumway and J. Drucker, *J. Appl. Phys.* **105**, 044312 (2009).
- [21] S. Ketharanathan, Ph. D. dissertation, Arizona State University (2007).
- [22] A. I. Yakimov, N. P. Stepina, A. V. Dvurechenskii and A. V. Nenashev, *Semicond. Sci. Technol.* **15**, 1125 (2000).
- [23] A. I. Yakimov, N. P. Stepina, A. V. Dvurechenskii and A. I. Nikiforov and A. V. Nenashev, *Phys. Rev. B* **63**, 045312 (2001).
- [24] A. I. Yakimov, A. V. Dvurechenskii and A. I. Nikiforov, *JETP Lett.* **73**, 529 (2001).
- [25] J. Li, M. R. McCartney, R. E. Dunin-Borkowski and D. J. Smith, *Acta Crystallogr., Sect. A* **55**, 652 (1999).
- [26] L. Reimer, *Transmission Electron Microscopy*, Springer, Berlin (1989).
- [27] J. A. Van Vechten, *Phys. Rev.* **182**, 891 (1969).

Chapter 4

OBSERVATION OF HOLE ACCUMULATION IN Ge/Si CORE/SHELL NANOWIRES

In this chapter, the study of hole accumulation in Ge/Si core/shell nanowires using off-axis electron holography is described. The Ge/Si core/shell nanowires were grown by chemical vapor deposition following the vapor-liquid-solid growth mode, and were provided by the group of Professor Jeff Drucker of Arizona State University. My contributions to this work have been determination of projected thickness of the nanowires using high-angle annular-dark-field imaging, and measurement of the hole density in the Ge core by applying electron holography. The results of this study have been published [\[1\]](#).

4.1 Introduction

In common with carbon nanotubes, which are potential building blocks for nanodevices [\[2\]](#), semiconducting Ge/Si core/shell nanowires (NWs) can be prepared with high yield and uniformity, with reproducible electronic properties [\[3\]](#). The Ge/Si core/shell system has Type-II band alignment with a valence band offset of several hundred meV between the Ge core and the Si shell [\[4\]](#), which drives hole accumulation inside the Ge core, while the Si shell serves to provide chemical passivation. With the much higher carrier mobility of Ge to Si, the intrinsic Ge core can achieve ballistic transport of up to a few hundred

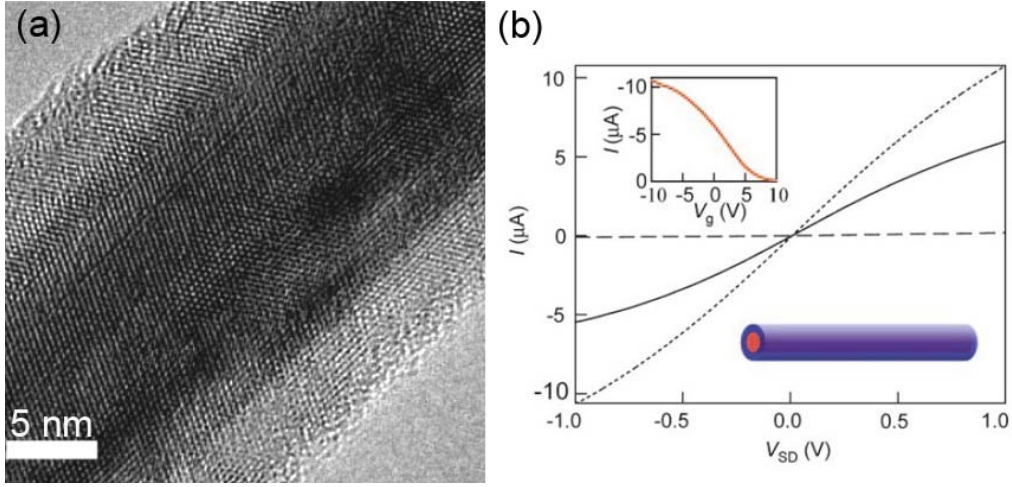


Figure 4.1 (a) HREM image of a Ge/Si core/shell NW with core diameter of 15 nm and shell thickness of 5 nm. (b) Room temperature electrical transport in Ge/Si core/shell NWs. The dashed line, solid line and dotted line of the I - V_{SD} curves correspond to back-gate voltages of +10V, 0, and -10V, respectively. The upper inset shows the I - V_g curve for the same device at $V_{SD} = -1$ V [5].

nanometers in length [5], so that the Ge/Si core/shell NW geometry is promising for future device applications.

It has been reported that field-effect transistors (FETs) incorporating i-Ge/i-Si core/shell NWs exhibit substantial current at zero gate voltage ($V_g = 0$), validating their behavior as p-type depletion-mode FETs [3, 5]. Figure 4.1 (a) shows a high-resolution electron microscopy (HREM) image of a Ge/Si core/shell NW with 15-nm Ge core diameter and 5-nm Si shell thickness. Figure 4.1 (b) shows room temperature electrical transport measurements for Ge/Si core/shell NWs [5]. The I - V_{SD} curves were recorded on a 10-nm core diameter Ge/Si NW with source

drain separation $L = 1 \mu\text{m}$. The dashed line, solid line and dotted line correspond to back-gate voltages of +10V, 0, and -10V, respectively. The inset shows the I - V_g curve for the same device at $V_{\text{SD}} = -1 \text{ V}$, which exhibits a decrease in current as V_g is increased from -10 to 10 V, and current $\sim 5 \mu\text{A}$ at zero gate voltage ($V_g = 0$), indicating the accumulation of hole charge carriers [5].

The direct detection of holes in Ge/Si core/shell NWs through enhanced Raman scattering has been reported [6], and the recent literature focuses on FET behavior and transconductance measurements [3, 5]. This current work presents a study of the i-Ge/i-Si core/shell NW system, concentrating on direct observation of static charge accumulation inside individual core/shell NWs using off-axis electron holography, and calculations of the corresponding charge densities.

4.2 Experimental Details

Epitaxial $\langle 110 \rangle$ -orientated Ge/Si core/shell NWs were grown on Si (111) substrates following the vapor-liquid-solid (VLS) growth mode [1]. The sample was grown by depositing 0.7 \AA of Au onto Si (111) which was heated to 450°C . The Ge cores were grown by heating the Au-coated Si (111) to 300°C followed by exposure to 5mTorr of digermane for 700 s. The digermane pyrolysis evolves hydrogen, which causes the half-monolayer-thick Au/Si (111) layer between three-dimensional Au seeds to dewet and to form small Au islands. These islands then facilitate the growth of epitaxial Ge NWs in $\langle 110 \rangle$ orientation with diameters $\sim 10 \text{ nm}$ [7]. The Si shells of $\sim 12\text{-nm}$ thickness were grown by heating the Ge cores to 540°C and exposing them to 3 mTorr of disilane for 400 s. Since

no seed particles were observed on the final Ge/Si core/shell NWs, they are presumed to have been dislodged during heating of the Ge cores before growth of the Si shells.

The NWs were removed from the Si substrate through sonication in isopropanol and then deposited on copper grids with holey carbon support films for electron microscopy observation. The high-resolution electron microscopy (HREM), energy-dispersive X-ray spectroscopy (EDS), and off-axis electron holography observations were carried out using a Philips CM200-FEG transmission electron microscope (TEM) equipped with an electrostatic biprism and a $2.8\text{k} \times 2.6\text{k}$ Gatan Orius SC200W charge-coupled-device camera. The off-axis electron holography was set up in the normal TEM geometry with a biprism voltage of ~ 130 V and a fringe contrast of $\sim 60\%$ in vacuum, and the magnification setting was ~ 300 kX. High-angle annular-dark-field (HAADF) images were obtained using a JEOL 2010F electron microscope with focused probe sizes in the range of 0.2-1 nm. In these experiments, the electron holography analysis was done first, followed by plasma cleaning of the sample for a few minutes, and then STEM intensity data was obtained from the same NW. This procedure provided a clean sample for electron holography observation before any damage or contamination of the specific NW was caused by the focused electron beam used for STEM analysis.

4.2.1 Determination of crystallographic and compositional structure

Figure 4.2 (a) is a HREM image of a Ge/Si core/shell NW, viewed along a $\langle 111 \rangle$ zone-axis projection, which clearly shows the Ge core (~ 10 nm) with darker contrast and the Si outer shell; both the core and shell regions are generally of excellent crystallinity. Figure 4.2 (b) shows a HAADF image of another Ge/Si core/shell NW. As expected for the HAADF imaging mode, the Ge core region shows brighter contrast than the Si shell. The results of EDS line profiles across the region indicated by the dashed black arrow in Fig. 4.2 (b), are shown in Figure 4.2 (c). The red line with squares shows the intensity for silicon, which peaks at the shell region and reaches a local minimum at the center of the core region. The blue line with disks corresponds to germanium, and peaks at the center of the core and decreases toward the wire edges. The green line with triangles is for carbon, and comes from some residual contamination on the NW surface. Overall, these results confirm the crystallographic and compositional structure of the core/shell NWs.

4.2.2 Determination of projected thicknesses

In order to use phase changes measured by off-axis electron holography to determine whether charge accumulation is present in Ge/Si core/shell NWs, it is first necessary to accurately measure contributions to the electron phase shift due to the projected thicknesses of both the Ge core and Si shell.

The initial approach to this project involved preparing cross-sections of the NWs, which would clearly show the core and shell regions with constant

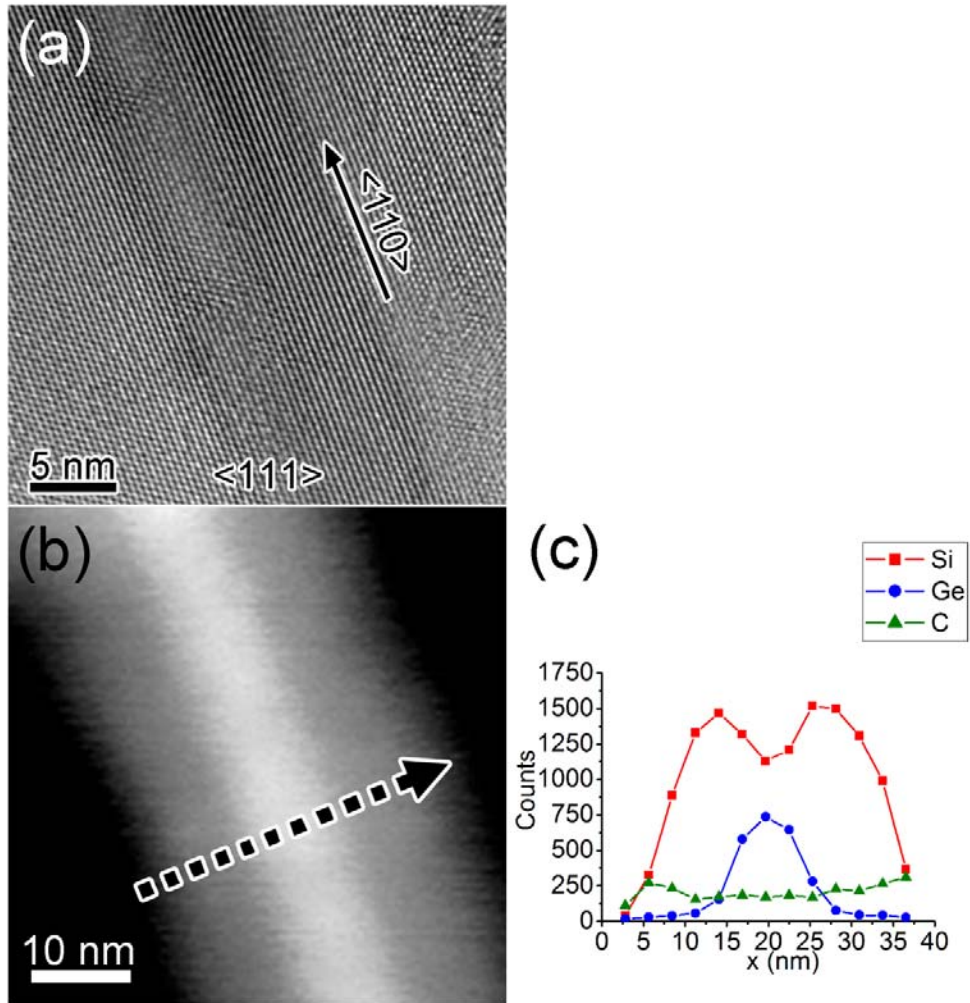
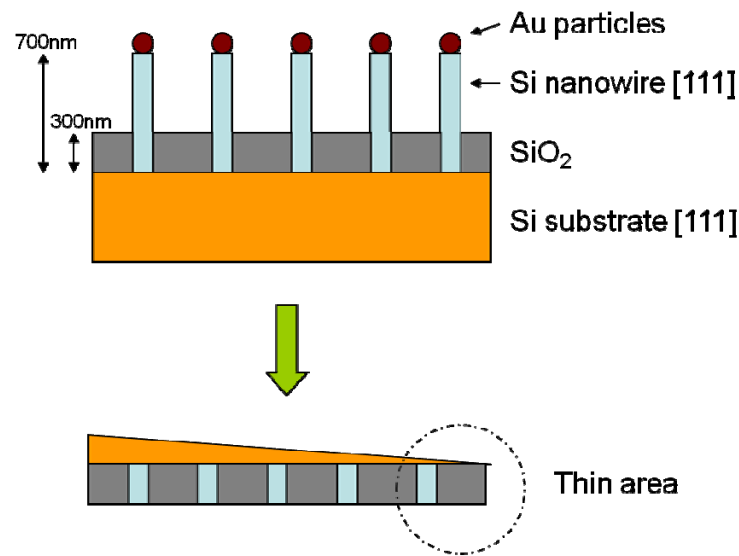


Figure 4.2 (a) HREM image confirming Ge/Si core/shell NW growth with good crystallinity. (b) HAADF image of Ge/Si core/shell NW showing brighter contrast in the core. Region used for EDS line profile is shown by the dashed black arrow. (c) EDS line profile: red line with squares is for Si, the blue line with disks is for Ge, and the green line with triangles is for C [1].

thickness. Figure 4.3 sketches the process that was used for preparing samples in this geometry. The trial experiments were performed on Si NWs grown along [111] direction, standing on Si substrates with normal axis also along [111]. The NWs were embedded inside 300-nm-thick SiO_2 layers to hold the NWs together during the sample preparation. Wedge polishing was used, and an angle of about 2° was introduced during sample thinning from the substrate side, with the thin area close to one edge.

As shown in Figure 4.4, the cross section of the Si NW grown along [111] direction showed close to an hexagonal shape, and was bounded by dark lines, which possibly originated from Au deposition on the side surface during NW



Only wedge polishing is applied for sample preparation.

Figure 4.3 Sketch of cross-sectional sample preparation for Si NWs.

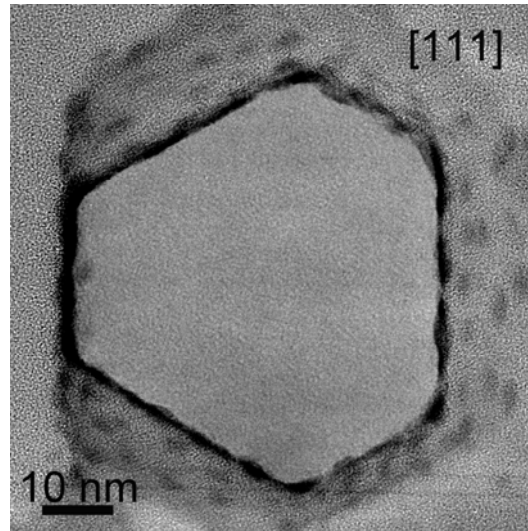


Figure 4.4 HREM image showing cross section of Si NW orientated along [111] zone axis.

growth. The amorphous region surrounding the NW is SiO₂ that was used to hold the NWs together during polishing. Here, the NW diameter is as large as ~50 nm.

This preparation method initially appeared to be promising for electron holography since the thickness determination would not be too difficult. However, there were several underlying problems to this approach. In particular, although the amorphous SiO₂ would be useful at the sample preparation stage, it would introduce serious charging problems under electron beam illumination, making any charge density determination in the NWs inaccurate. Moreover, Si(Ge) NWs grow along $\langle 110 \rangle$ directions on Si (111) substrates, as is the case for our holography study, are not perpendicular to the substrate. Figure 4.5 shows

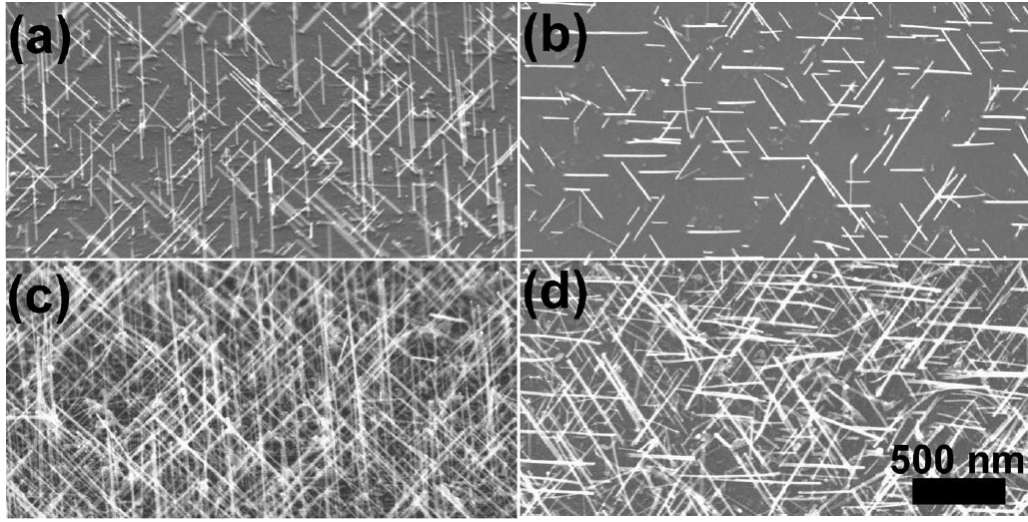


Figure 4.5 <110> Ge NWs formed by seedless VLS growth at $T = 300\text{ }^{\circ}\text{C}$ and $P = 5\text{ mtorr}$ digermane imaged using SEM. (a) and (b) grown with $\theta_{Au} = 1/2\text{ ML}$. (c) and (d) grown with $\theta_{Au} = 1\text{ ML}$. (a) and (c) were imaged 60° away from normal toward [112]. (b) and (d) are plan-view images [7].

a SEM image of <110> Ge NWs formed by seedless VLS growth at $T = 300\text{ }^{\circ}\text{C}$ and $P = 5\text{ mtorr}$ digermane. (a) and (b) show NWs grown with $\theta_{Au} = 1/2\text{ ML}$, which is the case for the samples studied by electron holography. (c) and (d) show NWs grown with $\theta_{Au} = 1\text{ ML}$, which possess much higher density of NWs. (a) and (c) were imaged 60° away from normal toward [112], while (b) and (d) are plan-view images [7]. These results establish that the NW growth deviates from the substrate normal. Moreover, when the NWs are embedded in SiO_2 , they may be suppressed to have even larger angles away from the direction of the substrate normal. Thus, tilting the NWs to align along the growth direction became very

difficult, sometimes even impossible, because the specimen holder of the microscope reached its limit of tilting.

Returning to plan-view orientation with the NW axes normal to the incident beam direction, the NWs can be loaded onto a carbon-film-coated copper grid, so that any charging is greatly relieved. However, the projected thicknesses obviously change from point to point across the NWs. Especially in the central regions, the Si shell and Ge core will have different thicknesses which contribute to the overall phase shift, making the problem even more challenging. The intensities of EDS line profiles for Si and Ge shown in Fig. 4.2 (c) are roughly proportional to the corresponding projected thicknesses, but they cannot be used to provide accurate information about the local thicknesses, since the step sizes used for the EDS line-profile analysis were as large as 2.8 nm, while the diameter of the Ge core was just ~ 10 nm. Thus, intensity profiles from HAADF images obtained with much smaller step size must be utilized for accurate thickness determination.

For a sample of thickness t , with N atoms per unit volume, the scattered intensity I_s for annular-dark-field imaging can be expressed as:

$$I_s = \sigma N t I \quad (4.1)$$

where σ is the cross section of the electrons scattered in the annular-dark-field aperture, which depends on the electron wavelength, scattering angle, and the atomic number of the material; and I is the incident beam current. Thus,

$$I_s = Z^\alpha N t \cdot C \quad (4.2)$$

where Z is the atomic number, and the exponent α should have a value between 1 and 2 depending on the specific microscope geometry [8]. C is a constant related to the incident beam current, the electron wavelength, and the inner and outer angles of the annular-dark-field detector. If α and C can be determined for the experimental conditions, then the projected thicknesses across the Ge/Si core/shell NW can be obtained for both the Si shell and Ge core regions. For example, the projected thickness for GaN quantum dots deposited on SiO_x substrates has been determined using HAADF intensity profiles [9].

In the current study, the widths for both the Ge core (8.7 nm) and the entire wire (25.7 nm) were first measured from HREM images, with the assumption that the maximum projected thicknesses for both the core and the entire wire have the same values as their widths measured from HREM images: this would certainly be the case for NWs with co-axial cylindrical shape.

HAADF images were obtained with a focused probe of ~ 0.2 nm using the JEOL 2010F. The region outlined in the box in Figure 4.6 (a) was used for the electron holography analysis which is described in detail below. The dashed black arrow shows the region selected for intensity line profile, as presented in Figure 4.6 (b). The white circles are experimental data obtained using a step size of 0.19 nm, which is more than an order of magnitude smaller than the step sizes used previously for EDS analysis. To reduce the signal-to-noise level, the shell region was fitted with a polynomial, which was then extrapolated to the NW core region to emphasize the different contributions of Ge and Si to the image intensity, as shown by the red squares.

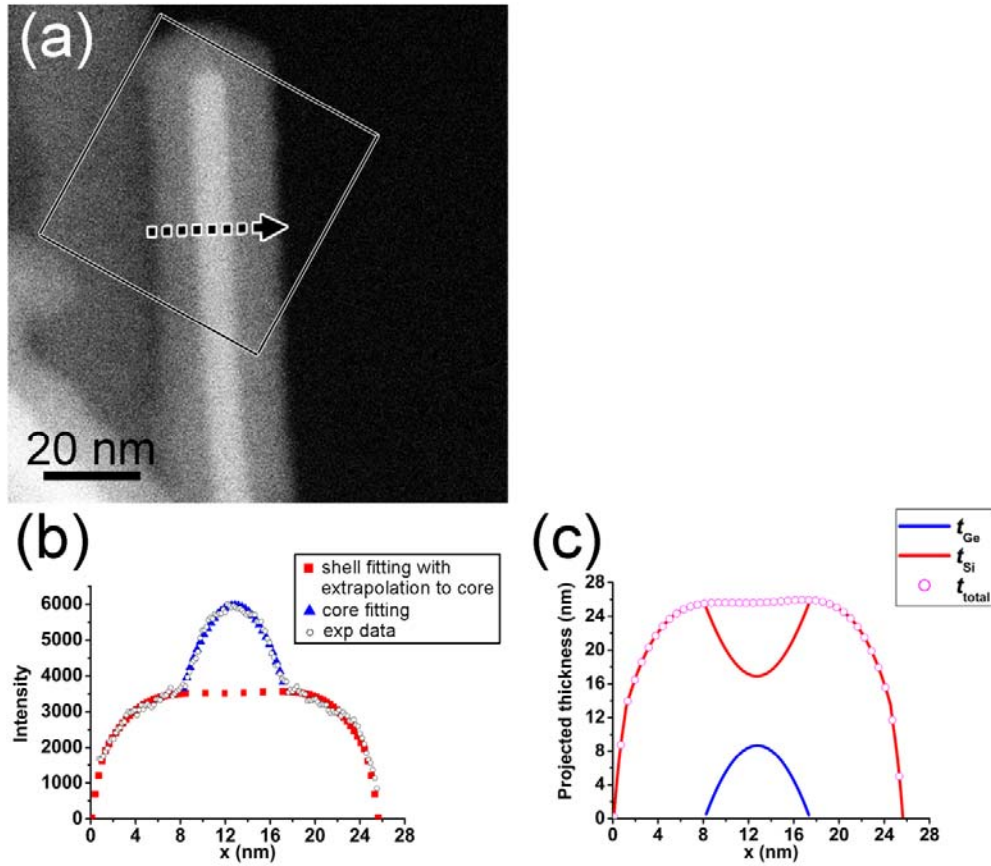


Figure 4.6 (a) HAADF image of Ge/Si core/shell NW with region used for intensity line profile analysis indicated by dashed black arrow. The outlined region inside the box was the region used for the electron holography analysis. (b) Corresponding intensity line profile results shown by white circles; core region shown by blue triangles is fitted with a polynomial, and the shell region shown by red squares is also fitted with a polynomial, which is extrapolated to the core region to emphasize the different contributions of Ge and Si to the image intensity. (c) Calculated projected thicknesses for Si shell (red line) and Ge core (blue line). The total thickness is represented by pink circles [1].

The profile from the core region, which is the actual intensity of the central overlap region for both Ge core and Si shell, as shown by blue triangles, was fitted with a polynomial. Thus, for the center of the NW, which corresponds to the maximum projected thickness, the following applies:

$$\frac{Z_{Si}^{\alpha} N_{Si} t_{tot}}{Z_{Si}^{\alpha} N_{Si} t_{Si} + Z_{Ge}^{\alpha} N_{Ge} t_{Ge}} = \frac{I_{red}}{I_{blue}} \quad (4.3)$$

where

$$t_{tot} = t_{Si} + t_{Ge} \quad (4.4)$$

$$\frac{N_{Si}}{N_{Ge}} = \frac{8/(a_{Si})^3}{8/(a_{Ge})^3} \quad (4.5)$$

The ratio of atomic densities was calculated to be 1.13 assuming $a_{Si}=5.431 \text{ \AA}$, and $a_{Ge}=5.657 \text{ \AA}$, and the exponent α was then found to be ~ 1.5 based on the above three equations. The constant is then calculated according to I_{blue} ,

$$I_{blue} = (Z_{Si}^{\alpha} N_{Si} t_{Si} + Z_{Ge}^{\alpha} N_{Ge} t_{Ge}) \cdot C \quad (4.6)$$

where $C=0.05 \text{ nm}^2$ for our case. The values for α and C are plugged into equation (4.3), so that the projected thicknesses for Si shell and Ge core across the NW are separately obtained. The results are presented in Figure 4.6 (c), with the red line corresponding to Si and the blue line to Ge. The total thicknesses, defined as the sum of Ge thicknesses and Si thicknesses, are shown by pink circles.

4.3 Results and Discussion

4.3.1 Calculation of hole density

Figure 4.7 (a) shows a hologram of the same NW, and Figure 4.7 (b) is the corresponding reconstructed phase image. The dashed black arrow in Fig. 4.7 (b) indicates the region used for phase-shift line profile analysis, and corresponds to the same region used for the HAADF intensity line profile. The result is represented by the white squares in Figure 4.7 (c), which is fitted with a polynomial for the Ge core shown in blue and also a polynomial for the Si shell shown in red. The green triangles show the calculated phase shift across the NW using the projected thickness data obtained from the HAADF intensity line profile. Mean inner potential (MIP) values of 15.5 V for Ge and 12.0 V for Si were used to calculate the expected phase shifts according to the projected thicknesses. The calculated phase shifts were close to the experimental phase shifts in the shell region, but they were much reduced relative to the experimental data in the core region.

For nonmagnetic materials, in the absence of fringing fields and phase shifts due to diffraction, the phase shift measured by electron holography has only electrostatic contributions and can be expressed as:

$$\phi(\vec{r}) = C_E (V_{MIP}(\vec{r}) + \Delta V(\vec{r}))t(\vec{r}) \quad (4.7)$$

Where C_E is an interaction constant that depends on the energy of the incident electron beam, with the value 0.00728 rad/(V nm) for 200 keV electrons, V_{MIP} is the mean inner potential defined as the volume-averaged electrostatic potential of a solid due to incomplete screening of atomic cores [10], ΔV is the potential due to accumulation of either positive or negative charges, and t is the projected thickness along the electron beam direction. The MIP values for nanostructures

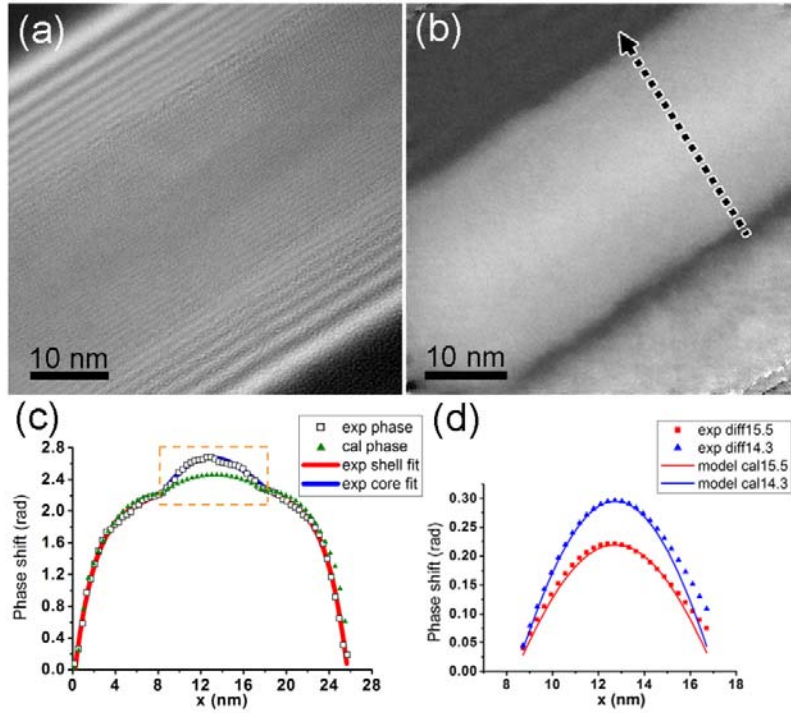


Figure 4.7 (a) Electron hologram of the Ge/Si core/shell NW observed by HAADF. (b) Reconstructed phase image of NW with the area used for HAADF intensity line profile labeled with dashed black arrow for phase-shift line profile. The result is shown by white squares in (c). The core region is fitted with a polynomial shown in blue and shell region is also fitted with a polynomial shown in red. The green triangles are the calculated phase shift using the projected thickness obtained from HAADF intensities. (d) Difference between the experimental and calculated phase shifts from the projected thicknesses. Mean inner potential values of 15.5 (red squares) and 14.3 V (blue triangles) for Ge, and 12.0 V for Si were used in the calculation. The blue line and red line are the corresponding calculated excess phase shifts based on the coaxial cylindrical model [1]

might be anticipated to be different from their bulk values because of the larger proportion of surface atoms [11]. For example, Chung *et al.* reported the MIP of Ge to be 15.5 V based on electron holographic measurements of Ge NWs of diameter ~ 110 nm with oxide shells [12], whereas Li *et al.* reported MIP of Ge to be 14.3(2) V for a cleaved Ge wedge [13]. For our core/shell NW system, the Ge cores are embedded inside Si shells, meaning that the core regions are also likely to be compressed [14], so that a higher MIP than for the bulk material might reasonably be expected. Thus, 14.3 V was taken as the lower boundary value for the MIP of Ge in our experiments.

The differences between the experimental and calculated phase shifts, based on projected thicknesses and applying two different MIP values for Ge, are presented as red squares and blue triangles in Figure 4.7 (d). The positive phase differences between the experimental and expected phase shifts due to thicknesses would seem to indicate accumulation of holes in the core regions. Values of 15.5 (red squares) and 14.3 V (blue triangles) for Ge, and 12.0 V for Si were used in calculating the differences between the experimental and calculated phase shifts, with red squares labeled as “exp diff 15.5” and blue triangles labeled as “exp diff 14.3”. The lower Ge MIP value results in slightly larger excess phase shifts in the core region.

Because of the large valence band offset between the Ge core and the Si shell, it is reasonable to expect hole accumulation in the Ge core, whereas negative charges may distribute throughout the surface regions of the shell. The presence of negative charge in the surface oxide has been reported previously for n-type

doped single Si NWs [15]. For our case, the origin of these negative charges could be either ionized surface states or adventitious ionized surface dopants. The calculation of charge densities in the NW core regions based on phase-shift measurements is difficult because the excess phase shift in the central regions has contributions from the projected charge densities of any surface oxide (negative charges) as well as the Ge core (positive charges).

In order to make an estimation of the hole density in the core, a coaxial cylindrical core/shell model was assumed for simplicity, and charge densities in the core and surface oxide regions were taken to be uniform. The constant C' is assigned to the ratio of ρ^+/ρ^- , where ρ^+ and ρ^- are the positive and negative charge densities. The constant C'' is a scaling factor that needs to be determined from experimental data. Thus,

$$\rho^+ = C' C'' \frac{1}{nm^3}, \rho^- = C'' \frac{1}{nm^3} \quad (4.8)$$

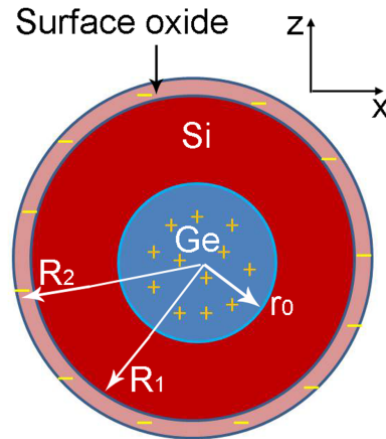


Figure 4.8 Sketch of the co-axial cylindrical model of Ge/Si core/shell nanowire: the charge distributions in the core and shell surface regions are indicated [1].

Gauss's Law can be applied to all three regions to obtain the electrostatic field distribution as a function of r (where r is the distance from center of the core):

$$(1) 0 \leq r \leq r_0$$

$$\oint \vec{E}_1 \cdot d\vec{S} = E_1 \cdot 2\pi rh = \pi r^2 h \rho^+ / \epsilon_0 \epsilon_{Ge} \quad (4.9)$$

$$\Rightarrow E_1 = \rho^+ r / 2\epsilon_0 \epsilon_{Ge}$$

$$(2) r_0 \leq r \leq R_1$$

$$\oint \vec{E}_2 \cdot d\vec{S} = E_2 \cdot 2\pi rh = \pi r_0^2 h \rho^+ / \epsilon_0 \epsilon_{Si} \quad (4.10)$$

$$\Rightarrow E_2 = \rho^+ r_0^2 / 2r\epsilon_0 \epsilon_{Si}$$

$$(3) R_1 \leq r \leq R_2$$

$$\oint \vec{E}_3 \cdot d\vec{S} = E_3 \cdot 2\pi rh = \pi h [r_0^2 \rho^+ - (r^2 - R_1^2) \rho^-] / \epsilon_0 \epsilon_{SiO_2} \quad (4.11)$$

$$\Rightarrow E_3 = [\rho^+ r_0^2 - \rho^- (r^2 - R_1^2)] / 2r\epsilon_0 \epsilon_{SiO_2}$$

Assuming that the electrostatic potential of the NW surface has the value of 0, then by integrating $E(x, z)$ along the radial direction to the NW surface, the electrostatic potential $\Delta V(x, z)$ can be obtained for each (x, z) point.

$$(1) 0 \leq r \leq r_0$$

$$\Delta V_1 = \int_r^{R_2} \vec{E} \cdot d\vec{l} = \int_r^{r_0} \vec{E}_1 \cdot d\vec{l} + \int_{r_0}^{R_1} \vec{E}_2 \cdot d\vec{l} + \int_{R_1}^{R_2} \vec{E}_3 \cdot d\vec{l} \quad (4.12)$$

$$(2) r_0 \leq r \leq R_1$$

$$\Delta V_2 = \int_r^{R_2} \vec{E} \cdot d\vec{l} = \int_r^{R_1} \vec{E}_2 \cdot d\vec{l} + \int_{R_1}^{R_2} \vec{E}_3 \cdot d\vec{l} \quad (4.13)$$

$$(3) R_1 \leq r \leq R_2$$

$$\Delta V_3 = \int_r^{R_2} \vec{E} \cdot d\vec{l} = \int_r^{R_2} \vec{E}_3 \cdot d\vec{l} \quad (4.14)$$

With a change from cylindrical coordinate system to a Cartesian coordinate system, and integrating along the beam direction (z direction), keeping x as variable, and keeping in mind that $r^2 = x^2 + z^2$, then the projection of the electrostatic potential $\Delta V(x, z) \cdot t(x)$ can be obtained as a function of x . This can then be converted into a phase shift according to the second part of Equation 4.7. The calculated excess phase shifts are presented in Fig. 4.7 (d) as the red line (model cal15.5) and the blue line (model cal14.3), and include scaling factors appropriate for the two different MIP values for Ge.

Note that the constant C' is determined according to the experimental result that the excess phase shifts at the core/shell interface are close to 0. The calculated phase shift plots are scaled (determination of constant C'') according to the experimental phase shift at the center of the wire. The hole density is calculated to be $0.5/\text{nm}^3$ when 15.5 V is used for Ge MIP, and the hole density is calculated to be $0.6/\text{nm}^3$ when 14.3 V is used. For comparison, the charge density for accumulated holes under Ge quantum dots embedded in Si has been found to be $0.03/\text{nm}^3$ [16], which is much smaller than the value measured here for the Ge/Si core/shell NW.

These calculations focused only on the core regions, and only hole densities were calculated. One reason was that a simplified coaxial cylindrical model was used for calculation, which seemed reasonable for the core but may not be the case for the shell. Another reason was that the decreasing thicknesses became more and more sensitive to local variations in surface roughness as the outer edges were approached, and this may result in unreasonable results for charge

accumulation.

This approach of combining measurements from HAADF and electron holography observations has been applied to several other Ge/Si core/shell NWs. For those NWs having core diameters of ~ 10 nm, the differences between experimental and calculated phase shifts show similar excess positive phase shifts in the core attributable to hole accumulation. Calculations for several different NWs provide rough estimates of error bars for the charge densities, giving a hole density of $(0.4 \pm 0.2)/\text{nm}^3$. However, for NWs having considerably smaller core diameters (~ 6 nm), it is interesting that the differences do not show excess positive phase shift in the Ge core.

4.3.2 Comparison with published measurements

Estimates of hole densities inside Ge/Si core/shell NWs have been made based on published measurements. The differential conductance G for Ge/Si core/shell NWs of core diameter ~ 10 nm and length ~ 170 nm has been found to be of the order of $\sim 2e^2/h$ [5], and the corresponding conductivity σ is calculated to be $\sim 1.67 \times 10^{-4} \text{ C/V}\cdot\text{s}\cdot\text{nm}$. Moreover, the hole density n is related to conductivity σ and hole mobility μ as follows:

$$n = \frac{\sigma}{e\mu} \quad (4.15)$$

The hole mobility for back-gate Ge nanowire transistors of 20-nm diameter has also been measured as a function of V_g [17]. The highest possible hole mobility, corresponding to $V_g \sim -0.8 \text{ V}$, was close to $600 \text{ cm}^2/\text{V}\cdot\text{s}$, and the hole

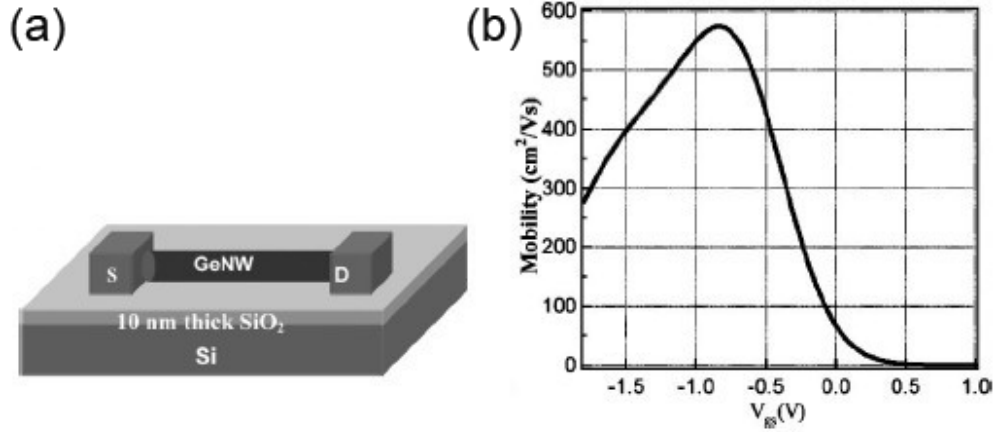


Figure 4.9 (a) Schematic side view of the Ge NWs FETs with back-gates and 10-nm-thick SiO₂ as the gate insulator. (b) Hole mobility vs gate voltage estimated from the transconductance of the device [17].

density using Equation 4.15 would then be $\sim 0.02/\text{nm}^3$. However, when $V_g = 0$ V (which corresponds to the experimental condition for the current work), the hole mobility is $\sim 70 \text{ cm}^2/\text{V}\cdot\text{s}$, and the corresponding hole density is then calculated to be $\sim 0.2/\text{nm}^3$, which is in reasonable agreement with the hole density measured here.

4.4 Conclusions

{110}-oriented Ge/Si core/shell nanowires with core diameters of ~ 10 nm have been grown by CVD on Si (111) substrates using the VLS growth mode. Si nanowires of trial samples were embedded in SiO₂ layers, and polished from the substrate side using wedge polishing. Cross-sectional images of the Si nanowires

were obtained, which looked promising from the sample preparation point of view, but this approach had several drawbacks which would have made accurate determination of charge densities inside the nanowires impossible. Intensity line profiles from HAADF images were utilized to determine the projected thicknesses of both Si shell and Ge core, and electron holography measurements from the same regions of the nanowire indicated hole accumulation in the Ge core region. Calculations based on a coaxial cylindrical model gave estimated hole densities, which were in reasonable agreement with hole density estimated based on published measurements. This combined approach of using HAADF and electron holography should provide useful insights in future studies of other NW systems.

REFERENCES

- [1] L. Li, D. J. Smith, E. Dailey, P. Madras, J. Drucker and M. R. McCartney, *Nano Lett.* **11**, 493 (2011).
- [2] P. L. McEuen, M. S. Fuhrer and H. K. Park, *IEEE Trans. Nanotechnol.* **1**, 78 (2002).
- [3] J. Xiang, W. Lu, Y. Hu, Y. Wu, H. Yan and C. M. Lieber, *Nature* **441**, 489 (2006).
- [4] F. Schäffler, *Semicond. Sci. Technol.* **12**, 1515 (1997).
- [5] W. Lu, J. Xiang, B. P. Timko, Y. Wu and C. M. Lieber, *Proc. Natl. Acad. Sci. U.S.A.* **102**, 10046 (2005).
- [6] S. Zhang, F. J. Lopez, J. K. Hyun and L. J. Lauhon, *Nano Lett.* **10**, 4483 (2010).
- [7] E. Dailey and J. Drucker, *J. Appl. Phys.* **105**, 064317 (2009).
- [8] P. Hartel, H. Rose and C. Dinges, *Ultramicroscopy* **63**, 93 (1996).
- [9] P. A. Crozier, J. Tolle, J. Kouvetakis and C. Ritter, *Appl. Phys. Lett.* **84**, 3441 (2004).
- [10] M. R. McCartney and D. J. Smith, *Annu. Rev. Mater. Res.* **37**, 729 (2007).
- [11] R. Popescu, E. Müller, M. Wanner and D. Gerthsen, *Phys. Rev. B* **76**, 235411 (2007).
- [12] J. Chung and L. Rabenberg, *Appl. Phys. Lett.* **88**, 013106 (2006).
- [13] J. Li, M. R. McCartney, R. E. Dunin-Borkowski and D. J. Smith, *Acta Crystallogr.* **A55**, 652 (1999).
- [14] I. A. Goldthorpe, A. F. Marshall and P. C. McIntyre, *Nano Lett.* **8**, 4081 (2008).
- [15] M. I. d. Hertog, H. Schmid, D. Cooper, J. Rouviere, M. T. Björk, H. Rivallin, S. Karg and W. Riess, *Nano Lett.* **9**, 3837 (2009).
- [16] L. Y. Li, S. Ketharanathan, J. Drucker and M. R. McCartney, *Appl. Phys. Lett.* **94**, 232108 (2009).

- [17] D. Wang, Q. Wang, A. Javey, R. Tu, H. Dai, H. Kim, P. C. McIntyre, T. Krishnamohan and K. C. Saraswat, Appl. Phys. Lett. **83**, 2432 (2003).

Chapter 5

CHARACTERIZATION OF CHARGE DISTRIBUTION ACROSS HOMOGENEOUS ZINC-BLENDE/WURTZITE HETEROSTRUCTURE JUNCTIONS IN ZnSe NANOBELTS INDUCED BY SPONTANEOUS POLARIZATION

In this chapter, the charge distribution present across homogeneous zincblende/wurtzite heterostructure junctions in ZnSe nanobelts due to spontaneous polarization is characterized quantitatively using off-axis electron holography. The ZnSe nanobelts were fabricated via thermal evaporation of ZnSe powder, and provided by Dr. Lei Jin and Professor Jianbo Wang in Wuhan University, and the growth work was completed in the laboratory of Professor Wallace C.H. Choy in University of Hong Kong. My major contribution was the electron holography characterization, the strain map calculation was performed by Lei Jin, the aberration-corrected high-angle-annular dark-field imaging was provided by Jianbo Wang, and the first principles' calculations were performed by Dr. Wan-Jian Yin and Professor Yanfa Yan at the National Renewable Energy Laboratory. The work has recently been submitted for publication [\[1\]](#).

5.1 Introduction

Tailoring of charge distribution has been an increasingly important topic for semiconductor-based materials ever since the discovery of Si *p-n* junctions in the

1940's. Such p - n junctions can be created in semiconductor single crystals by doping, thereby introducing impurity levels into the band gap, and forming a depletion region with built-in potential difference across the junction. Heterostructures consisting of materials of different band gaps can have considerable valence or conduction band offsets at the interfaces, which will cause electrons or holes to reside in the same material [2] (for type I band alignment), or to become separated in different materials [3] (for type II band alignment). The strain due to lattice mismatch at the interface also introduces band-bending, which can facilitate higher density of charge localization at the interfaces [4].

The controlled growth of twinned structures and polytype superlattices in Group III-V (InP, InAs, GaAs) nanowires leads to homogeneous heterostructural junctions [5-8]. As shown in Figure 5.1 (a), redshift of the photoluminescence emission energy is observed for GaAs nanowires when the percentage of wurtzite (WZ) material as compared to zincblende (ZB) material is increased [8]. Blueshift of the photoluminescence of the rotationally twinned heterostructure in InP nanowires is dependent on the excitation power [9], as shown in Figure 5.1 (b). These novel optical properties are attributed to the comparatively large band offsets between the ZB and WZ polytypes, which lead to charge redistribution along the nanowires.

In this study, ZB/WZ heterostructural junctions in ZnSe nanobelts have been fabricated using controlled growth conditions. Direct observation of the

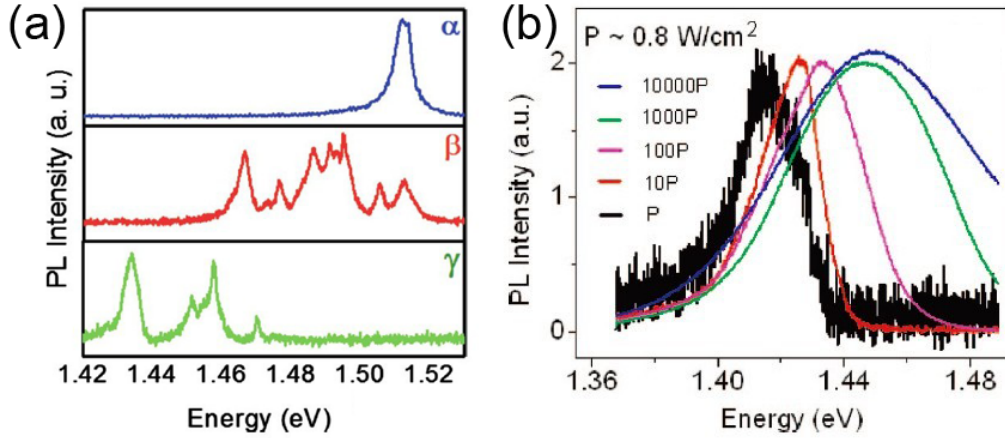


Figure 5.1 (a) Typical photoluminescence spectra obtained from three types of GaAs nanowires at $T = 4.2$ K. The percentage of wurtzite compared to zincblende structure increases from α to γ , while the corresponding emission energy shifts from 1.51 eV down to 1.43 eV [8]. (b) Photoluminescence from an InP nanowire with rotational twins under different excitation intensities at 7 K [9].

electrostatic fields and charge redistribution across the homogeneous interfaces, which is attributed to the spontaneous polarization (SP) present in the WZ regions, has been achieved using off-axis electron holography. ZnSe was selected for investigation since the ZB/WZ interface in ZnSe nanobelts should have close to zero valence and conduction band offsets [10], as indicated by the empty squares in Figures 5.2 (a) and (b) for the case of ZnSe. Thus, contributions from band offsets can be eliminated, which makes possible the measurement of the SP-related electrostatic field.

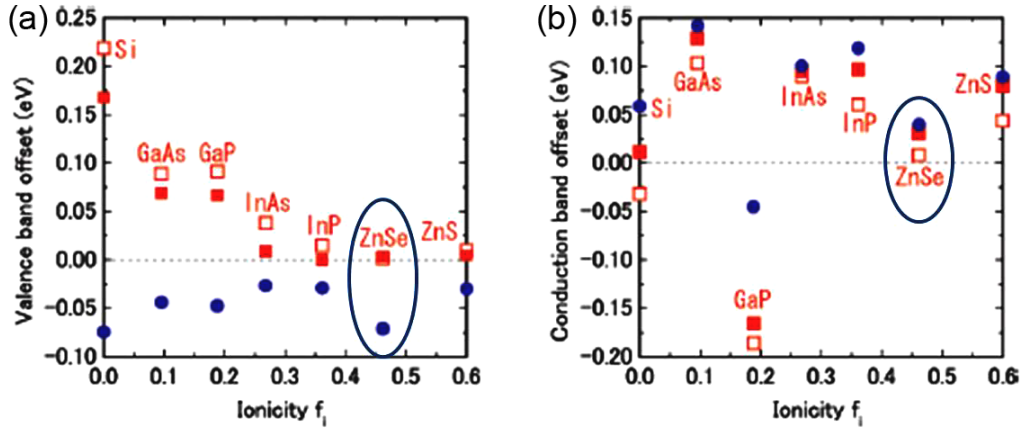


Figure 5.2 Calculated (a) valence band and (b) conduction band offsets as a function of ionicity f_i . Empty and filled squares and circles represent the band offsets at ZB- $\{111\}$ /WZ- $\{0001\}$, 6H- $\{0001\}$ /WZ- $\{0001\}$ interfaces, respectively. Circles represent the band offsets at 6H/WZ interface in nanowires [10].

5.2 Experimental Details

The homogeneous ZnSe ZB/WZ heterostructure junctions were fabricated via thermal evaporation of ZnSe powder. ZnSe vapor, which was generated in the high temperature zone (1000 °C), was transported by the Ar premixed 5% H₂ carrier gas and deposited on Au-sputtered Si (100) substrates in the low temperature zone (800 °C). The whole growth procedure lasted for 30 min. Further information about the materials growth has been published elsewhere [11]. The products were scratched off the Si substrate, sonicated in ethanol, and then deposited on copper grids with holey carbon support films for electron microscopy observation.

The off-axis electron holography observation and high-resolution electron microscopy (HREM) imaging were carried out using a Philips CM200-FEG transmission electron microscope (TEM) equipped with an electrostatic biprism and a 2.8 k×2.6 k Gatan Orius SC200W charge-coupled-device (CCD) camera. The sample was imaged with the microscope in the diffraction mode but with the diffraction lens turned off in order to gain a larger field of view. The fringe spacing was ~ 0.57 nm, and the overall image magnification was set at ~ 120 kX. The HREM images used for strain-map calculations were obtained using a JEOL JEM-2010 FEF (UHR) TEM. The aberration-corrected high-angle-annular dark-field (HAADF) imaging was performed using a JEOL ARM200F TEM. All of the microscopes were operated at an accelerating voltage of 200 kV.

5.3 Results and Discussion

5.3.1 Phase shift across WZ/ZB/WZ interfaces

Figure 5.3 (a) shows an off-axis electron hologram of a ZnSe nanobelt which includes WZ/ZB/WZ regions. The nanobelt was first tilted to the closest ZB[-110]/WZ[-2110] zone axis, and then rotated slightly around the axis normal to the ZB[111]/WZ[0001] junctions in order to avoid diffraction contrast while the junctions were kept edge-on to the incident beam. Figure 5.3 (b) shows a high-resolution image of the same nanobelt, with the bottom left corner corresponding to the amorphous layer along the edge of the nanobelt. There is a WZ region of width ~ 7 nm to the right of the amorphous layer, then a ZB region of width ~ 22 nm, and a wider region of WZ that is only partly visible in the HREM image.

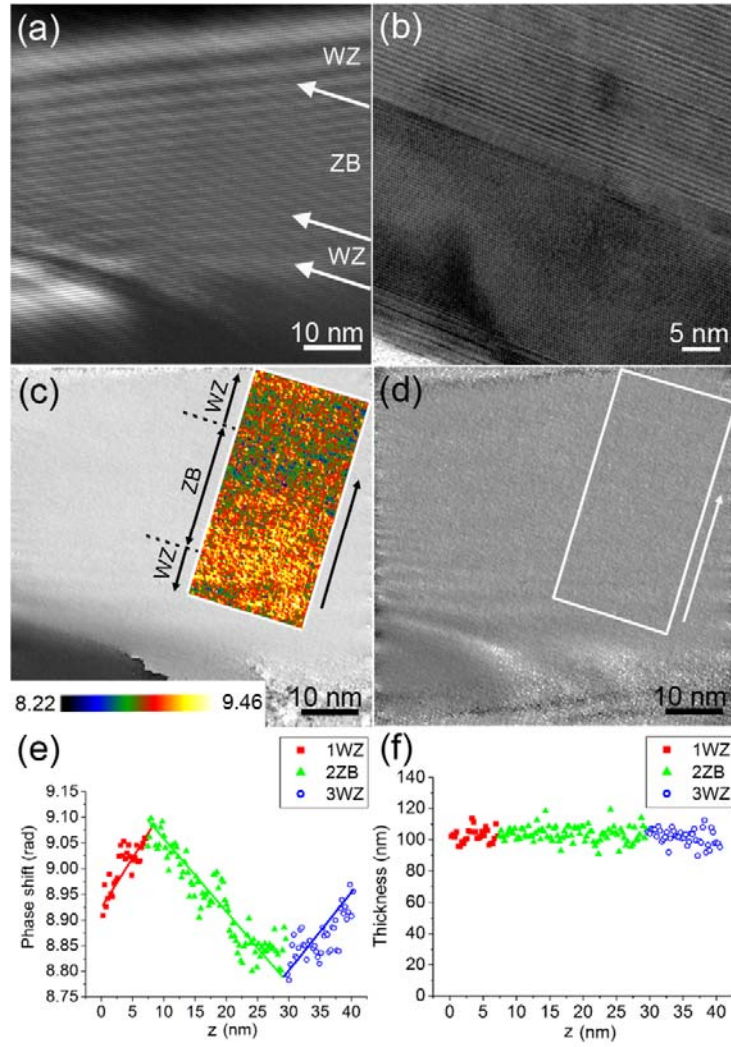


Figure 5.3 (a) Electron hologram from ZnSe nanobelt location including WZ/ZB/WZ junctions. (b) HREM image of the same nanobelt at higher magnification. (c) Corresponding reconstructed phase image. The box region used for profiling is shown in color with the WZ and ZB regions labeled. Color bar calibrated in radians is also shown. (d) Thickness image of the same region. (e) Phase shift profile of the box region labeled in (c). (f) Thickness profile of the box region labeled in (d), which is the same region used for phase shift line profile [1].

Figures 5.3 (c) and 5.3 (d) are the corresponding reconstructed phase and thickness images, respectively. The thickness image was calculated based on the reconstructed amplitude image assuming a value of 67 nm (for GaAs) [12] for the inelastic mean free path (MFP) for ZnSe [13], since the MFP value for ZnSe was not known. However, it seems reasonable to use the MFP for GaAs since ZnSe and GaAs have equal average atomic numbers, which is the major factor in determining the magnitude of the inelastic MFP.

Line profiles for the phase shift and thickness perpendicular to the WZ/ZB/WZ junctions are shown in Figures 5.3 (e) and 5.3 (f), respectively. The boxed region used for line profiling is outlined in Figs. 5.3 (c) and (d), starting from the interface of the amorphous layer and the bottom WZ region. The box region in Fig. 5.3 (c) is shown in color with the WZ and ZB regions labeled, and the color bar calibrated in radians is also shown in the bottom left corner. The red squares in Figs. 5.3 (e) and 5.3 (f) represent the experimental data for the bottom WZ region, the green triangles correspond to the sandwiched ZB region, and the blue circles correspond to the top WZ region. The phase shifts in Fig. 5.3 (e) increase almost linearly in the WZ region, and decrease linearly in the ZB region, while the turning points coincide with the junction positions. Linear fits to the experimental data are added as red, green and blue lines. The thickness profile, on the other hand, is basically flat across the whole region, which means that the thickness is effectively constant, and that local changes in diffraction contrast are not causing significant contributions to the phase shifts. Thus, the decreasing (ZB region) and increasing (WZ region) phase shifts indicate that opposite

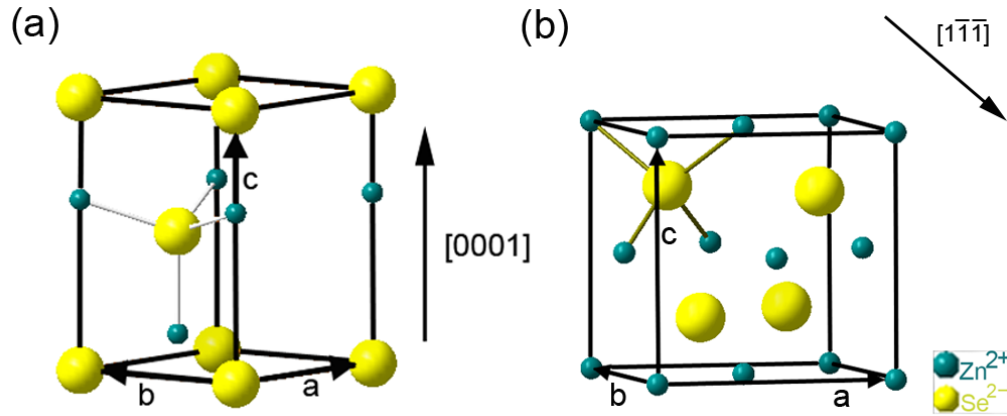


Figure 5.4 Sketches of: (a) unit cell of wurtzite structure; and (b) unit cell of zincblende structure.

electrostatic fields are present in these regions, meaning that charges of opposite signs must be located at the adjacent junctions.

The WZ structure is expected to possess an intrinsic spontaneous polarization (SP) since the four tetrahedral bonds do not have equivalent bond-to-bond charge transfer, and ionic relaxation can also cause SP along the (c axis) stacking direction [14]. Conversely, the tetrahedral bonds are symmetric for the ZB structure, and thus the cubic ZB structure has no bulk SP. Moreover, the cubic lattice grown along $\langle 111 \rangle$ provides perfect interface matching with the WZ $\langle 0001 \rangle$, i.e., surface and truncation effects can be avoided [13], which makes it a perfect medium for determination of SP in the WZ region. Sketches of unit cell models for both WZ and ZB structures are shown in Figures 5.4 (a) and (b), respectively. Theoretical calculation of potential profiles across the ZB/WZ SiC

interface and charge densities at the junctions have been reported for BeO [15], [14, 16-17], BN and GaN [16], and these show very similar features as the results presented in Fig. 5.3 (e).

5.3.2 Piezoelectric polarization across ZB/WZ interface

For nitride-based heterostructures, the electrostatic potential across junctions is usually induced by a combination of both spontaneous polarization and piezoelectric polarization [18-19]. Thus, it is necessary to take possible contributions from piezoelectric polarization (PE) into consideration for our holography observations. In the linear regime, PE is related to strain by the piezoelectric tensor via the expression [20]:

$$P_i = \sum_j e_{ij} \epsilon_j \quad (5.1)$$

Due to symmetry, the piezoelectric tensor for the WZ structure has three non-zero independent components: e_{33} , e_{31} , e_{15} , and only e_{33} and e_{31} are related to PE in the $\langle 0001 \rangle$ direction [20]. The piezoelectric tensor of the ZB structure has only one independent component e_{14} contributing to PE in the $\langle 111 \rangle$ direction [21]. Thus, the axial component of the PE can be expressed as [22-23]:

$$P_z = \begin{cases} -\frac{e_{14}}{\sqrt{3}}(\epsilon_{xx} + \epsilon_{yy} - 2\epsilon_{zz}) & ZB \\ e_{31}(\epsilon_{xx} + \epsilon_{yy}) + e_{33}\epsilon_{zz} & WZ \end{cases} \quad (5.2)$$

where the z axis is $[111]$ for ZB structure and $[0001]$ for WZ structure, which are aligned in the same direction, and the x and y axes are located in the ZB/WZ interface plane.

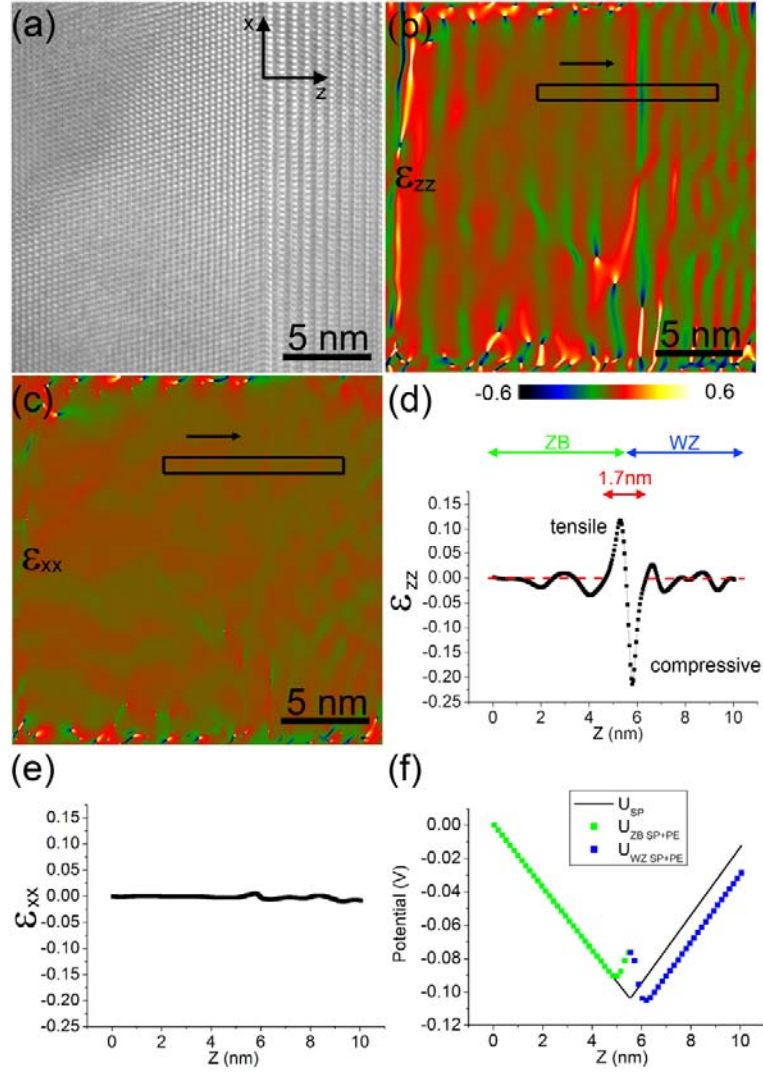


Figure 5.5 (a) HREM image of the ZB/WZ interface as used for strain map calculation. (b) Strain map for ϵ_{zz} and (c) strain map for ϵ_{xx} of the same region of HREM imaging. (d) Line profile of ϵ_{zz} of the boxed region labeled in (b). (e) Line profile of ϵ_{xx} of the same region. (f) The black line is the potential due to spontaneous polarization only, and the green and blue dots represent the potential due to mutual contributions from spontaneous and piezoelectric polarizations, where green and blue correspond to ZB and WZ regions, respectively [1].

Figure 5.5 (a) is an HREM image showing the ZB/WZ interface of another ZnSe nanobelt, and the x and z axes are labeled. The geometric phase analysis (GPA) technique for mapping displacement fields and strain fields from HREM images was utilized [24], and a GPA program compatible with Digital Micrograph was used for calculation of the strain map. Figures 5.5(b) and (c) show strain maps for ϵ_{zz} and ϵ_{xx} respectively, using the same color scale. The reference lattice was taken from the ZB region. The corresponding line profiles across the ZB/WZ interface, which are averaged over the boxed region in the strain map, are shown in Figure 5.5 (d) and (e). The strain component ϵ_{zz} has a positive peak in the ZB region, and a negative peak in the WZ region. Closer inspection reveals that the strain component ϵ_{zz} away from the interface is approximately zero, as shown by the red dashed line in Fig. 5.5 (d). Normally, the strain component ϵ_{zz} across a heterostructural interface would give a step-like profile [24-25]. Thus, the close to zero values in the ZB and WZ regions indicate very low levels of strain in both regions, and hence very small PE contributions to the electrostatic fields. The sharp abrupt peaks at the interface may be due to phase shifts that originate from the deviation from periodicity of the crystal lattices at the interface.

In comparison, the strain component ϵ_{xx} is close to zero across the interface, so that normal strain in the x direction can be ignored. Since the normal strain in the interface plane is usually treated as isotropic [20], it is reasonable to assume that ϵ_{yy} would also be close to zero. Thus, according to Equation (5.2), only the

third terms remain for both the ZB and WZ regions, and only ε_{zz} contributes to the PE along the interface normal.

It has been reported that $e_{33} = 0.04 \text{ C/m}^2$, and $e_{14} = (\sqrt{3}/2 e_{33})$ for ZnSe [20]. Thus, the PE along the interface normal p_z can be calculated applying Equation (5.2). The corresponding electrostatic field E_z is then obtained using: $E_z = p_z / [(\varepsilon_r - 1) \varepsilon_0]$, where $\varepsilon_r = 9.25$ (at $T = 296\text{K}$) is used [26], and $\varepsilon_0 = 8.85 \times 10^{-12} \text{ C}^2/(\text{N m}^2)$. By integrating the resulting electrostatic field along the interface normal, the electrostatic potential due to PE can be calculated. The starting point for the integration is assumed to be at zero potential.

Since ε_{zz} is localized to a narrow region close to the interface, the long-range linear slopes as shown in Fig. 5.3(e) should be mainly due to SP present in the WZ regions. The phase shift profile in Fig. 5.3(e) can be converted to electrostatic potential using: $\phi = C_E (V_{\text{MIP}} + V_{\text{SP}}) t$, where $C_E = 0.00728 \text{ rad}/(\text{V nm})$ for an accelerating voltage of 200 kV, ϕ is the phase shift, t is the projected thickness, V_{MIP} is the mean inner potential (MIP) of the material, and V_{SP} is the electrostatic potential due to SP [27]. Only the latter term would contribute to the electrostatic field via a slope of the electrostatic potential profile since the MIP would be constant for a specific structure. Thus, the electrostatic field E can be calculated for both ZB and WZ regions based on linear fits of experimental phase shift data: $E_{\text{ZB}} = 0.0189 \text{ V/nm}$, $E_{\text{WZ}} = -0.0204 \text{ V/nm}$.

The black line presented in Figure 5.5(f) is the potential due to SP only (U_{SP}), and the green and blue dots represent the potential due to contributions from the SP and PE ($U_{\text{SP+PE}}$), where green and blue correspond to the ZB and WZ regions,

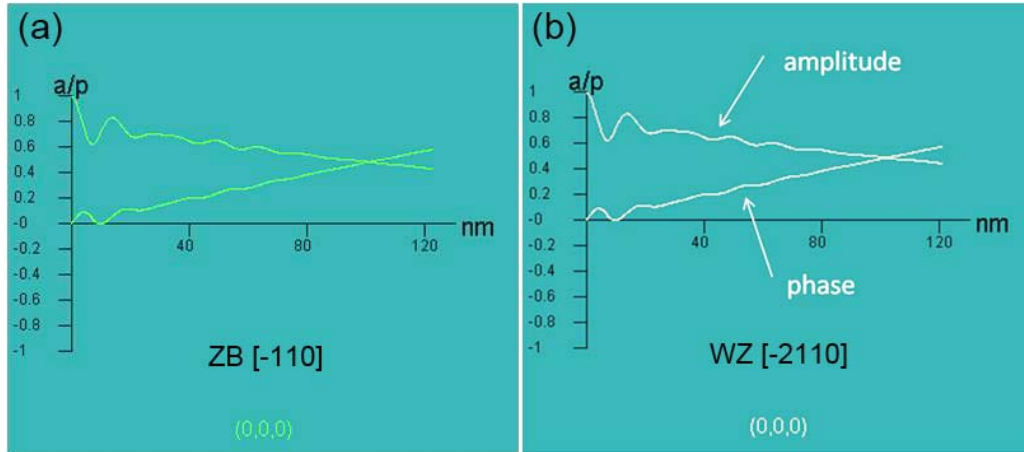


Figure 5.6 Simulations of the amplitude/phase VS. thickness relations for the transmitted beam (the (000) beam) for (a) ZB structure at $[-110]$ zone axis and (b) WZ structure at $[-2110]$ zone axes.

respectively. While the ZB region looks exactly the same, the U_{SP+PE} begins to deviate from U_{SP} close to the ZB/WZ interface, and maintains constant difference throughout the WZ region, with a maximum potential difference of ~ 0.027 V. On the other hand, the average noise level of the experimental phase shift is ~ 0.026 rad as compared to the linear fit, which can be converted to ~ 0.035 V as an estimate for the noise level of electrostatic potential. Since the maximum potential difference between U_{SP+PE} and U_{SP} is less than the experimental noise level of the electrostatic potential, it can be concluded that the contributions from PE are not significant.

5.3.3 Mean inner potential of ZB and WZ ZnSe

The possibility of a difference between the MIP for the ZnSe ZB and WZ structures also needs to be considered. Since the MIP is determined mostly by the structure and composition of the specimen [28], simulations of the amplitude/phase vs. thickness relations for the transmitted beam (the (000) beam) for both ZB and WZ structures at corresponding zone axes have been performed using the program JEMS [29]. The results are shown in Figures 5.6 (a) and (b). The amplitude/phase vs. thickness profiles show exactly the same relationship for ZB and WZ structures, indicating that the ZB[-110] and WZ[-2110] have very similar atomic structures. Thus, the ZB and WZ structures, which have the same composition, should have similar MIP values.

Theoretical calculations of MIP for both ZB and WZ structures have also been performed based on the theory discussed in 2.1.4. The Doyle-Turner scattering amplitudes were used: $f_{\text{Zn}}(0) = 6.065 \text{ \AA}$, $f_{\text{Se}}(0) = 7.205 \text{ \AA}$ [30]. For the ZB structure of ZnSe: $a = b = c = 5.687 \text{ \AA}$, and the unit cell has 4 Zn and 4 Se atoms. By applying Equations (2.17) and (2.19), the range of MIP is calculated to be: 9.991~13.824V. For the WZ structure of ZnSe: with $a = b = 3.974 \text{ \AA}$, $c = 6.506 \text{ \AA}$, the unit cell has 2 Zn and 2 Se atoms, and the range of MIP is calculated to be: 10.348~14.288V. Thus, the calculations reveal that the ranges of MIP values for the ZB and WZ structures are close to each other. Meanwhile, any MIP difference between the ZB and WZ structures would just result in small steps at the interfaces, but should not cause slopes in the different regions. Thus, any contribution of the MIP difference to the observed electrostatic field can be excluded.

5.3.4 Aberration Corrected HAADF imaging of ZnSe ZB/WZ interface

To understand the SP-induced electrostatic fields from a structural point of view, an investigation of atomic arrangements and polarity continuity was made using aberration-corrected HAADF imaging at the ZB/WZ interface of a specific ZnSe nanobelt, as shown in Figure 5.7 (a). The left region is the ZB projected along $[-110]$, and the right region is the WZ projected along $[-2110]$. The intensity line profiles along an array of Zn-Se atomic columns in the ZB region (labeled as 1), and along two dumbbells in two directions in the WZ region (labeled as 2 and 3) are shown on the right. Although the atomic number of Zn and Se are close together (Zn: 30, Se: 34), it is still apparent that the intensity peak on the right is higher than the closest peak on the left, indicating that the heavier atoms are located on the right. Moreover, it is significant that the crystal polarity maintains the same direction across the ZB/WZ interface, as can be observed from the conformity from regions 1 to 2 and 3. Thus, no charge accumulation due to polarity reversal would be anticipated at the interface.

Based on these observations, atomic models for the WZ/ZB/WZ interfaces are presented in Figure 5.7 (b). The blue and yellow balls represent Zn^{2+} and Se^{2-} , respectively. Due to the asymmetric tetrahedral bonding in the WZ unit cell, dipoles would be accumulated along the $[000-1]$ direction, leaving positive charge at the WZ/ZB junction, and negative charge at the ZB/WZ junction. Thus, there should be linearly increasing electrostatic potential and negative electrostatic field in the WZ region, and linearly decreasing electrostatic potential and positive

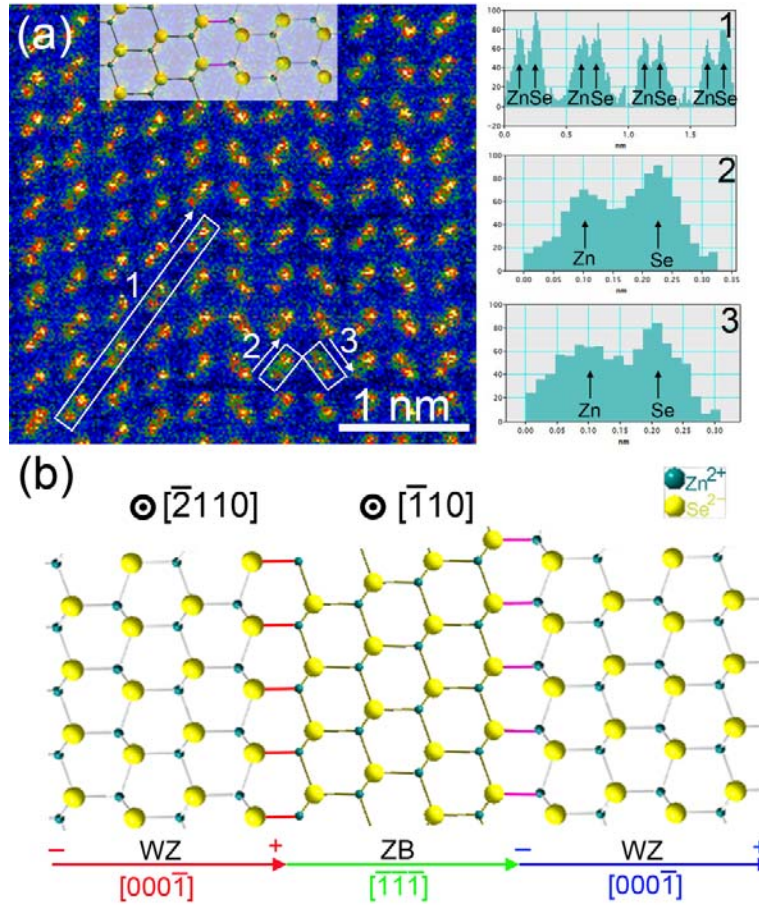


Figure 5.7 (a) Aberration-corrected HAADF image of ZB/WZ interface: the separate Zn-Se atomic columns are clearly observed. The intensity line profiles along an array of Zn-Se atomic columns in ZB region (labeled as 1), and along two dumbbells in two directions in WZ region (labeled as 2 and 3) are shown on the right. The peaks on the right are always higher than the adjacent peaks on the left. (b) Atomic model for the WZ/ZB/WZ heterostructures: the ZB region projected along $[\bar{1}10]$, and the WZ region is projected along $[\bar{2}110]$. The directions along the interface normal are also labeled [1].

electrostatic field in the ZB region induced by those polarization charges, which is in agreement with the electron holography observations.

5.3.5 Spontaneous polarization for ZnSe

The SP in the WZ region can be calculated using [14]:

$$p_{sp} = -\epsilon_0(\epsilon_r - 1)\Delta E = -\epsilon_0(\epsilon_r - 1)\left(\frac{\partial V_{WZ}}{\partial z} - \frac{\partial V_{ZB}}{\partial z}\right) \quad (5.3)$$

where $-\frac{\partial V_{WZ}}{\partial z}$ and $-\frac{\partial V_{ZB}}{\partial z}$ correspond to the electric fields in the WZ and ZB regions, which are $E_{WZ} = -0.0204$ V/nm, and $E_{ZB} = 0.0189$ V/nm for our specific case. Thus, the SP present in the WZ region is calculated to be $p_{sp} = -0.0029$ C/m². The error in potential measurement is estimated to be $\Delta V = \pm 0.035$ V, and $\Delta z = \pm 0.2565$ nm (the pixel size). Through error propagation, the error for p_{sp} is calculated to be $\Delta p_{sp} = \pm 0.00013$ C/m². There are no calculated or experimental SP values available for ZnSe. Thus, the bulk SP values of WZ-ZnSe and ZB-ZnSe have been calculated using the Berry phase expression [31-32] based on first-principles' calculations implemented in VASP [33-34]. The calculated bulk SP values for WZ-ZnSe and ZB-ZnSe are -0.0063 and 0.0 C/m², respectively. Using the same method, the calculated SP value for WZ-ZnO is about -0.064 C/m², consistent with the reported value of -0.058 C/m² [35]. Our measured SP value for WZ-ZnSe (-0.0029 C/m²) is about half of the theoretical value (-0.0063 C/m²): possible reasons for the discrepancy are discussed below.

Determination of crystal polarity by electron holography has been reported

for ZnO thin films, which showed a large fringing field in nearby vacuum due to accumulation of surface polarization charge [36]. Figures 5.8 (a) and (b) show the electron hologram, and corresponding reconstructed phase image, of the ZnO thin film. Figure 5.8 (c) is the one-dimensional phase change profile averaged from the box region labeled in (b). In that study, the amorphous layer on the surface was deliberately removed by low-energy ion-milling before electron holography observation. In our current study, an amorphous layer is present possibly due to contamination during sample growth as well as during TEM observation, and the corresponding HREM image shows a layer thickness of ~ 5

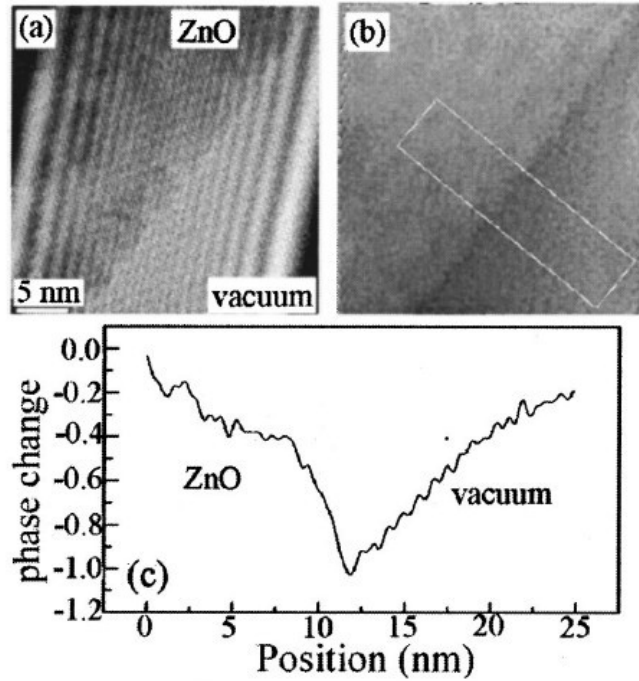


Figure 5.8 (a) Electron hologram of ZnO film. (b) Phase image reconstructed from the hologram. (c) Averaged one-dimensional phase change profile obtained from the box region in (b) [36].

nm on the edge. The actual thickness of the surface amorphous layer is about 5~10 nm. The electron holography results show very flat phase shift in vacuum, indicating no significant fringing field. Any possible secondary electrons would distribute uniformly on the sample surface, but not affect the electric field. Thus, it seems possible that any electrons or ions in the amorphous layer selectively reside at the regions of higher density of polarization charges, partly neutralizing the charges and screening the fringing field. The observed opposing electrostatic fields indicate that neutralization and screening is not complete, and this screening effect could possibly explain the lower SP value calculated from our electron holography data compared to the theoretical value.

5.4 Conclusions

The homogeneous zincblende/wurtzite heterostructure junctions in ZnSe nanobelts have been characterized using off-axis electron holography. The observation of electrostatic fields and charge accumulation is attributed to spontaneous polarization present in the wurtzite regions, and the spontaneous polarization of ZnSe is calculated to be $p_{sp} = -(0.0029 \pm 0.00013) \text{ C/m}^2$. The first-principle calculation is also performed which gives $p_{sp} = -0.0063 \text{ C/m}^2$ for the ZnSe wurtzite structure. The reduced experimental SP value is possibly due to the screening effect of the surface amorphous layer. The contributions from piezoelectric polarization at the ZB/WZ interface are shown to be insignificant based on the geometric phase analysis. The atomic structure and polarity continuity across a ZnSe ZB/WZ interface have been determined using

aberration-corrected HAADF imaging. There is no polarity reversal at the interface, which would otherwise result in charge accumulation. By controlling growth conditions, polytype heterostructures which are unstable in the bulk, can be formed in nanostructures. These results suggest a possible different path for tailoring charge distribution in semiconductor nanostructures, which is likely to have future applications for electronic devices.

REFERENCES

- [1] L. Li, L. Jin, J. Wang, D. J. Smith, W. Yin, Y. Yan, W. C. H. Choy and M. R. McCartney, Phys. Rev. Lett. (submitted).
- [2] H. Drexler, D. Leonard, W. Hansen, J. P. Kotthaus and P. M. Petroff, Phys. Rev. Lett. **73**, 2252 (1994).
- [3] W. Lu, J. Xiang, B. P. Timko, Y. Wu and C. M. Lieber, Proc. Natl. Acad. Sci. U.S.A **102**, 10046 (2005).
- [4] L. Li, S. Ketharanathan, J. Drucker and M. R. McCartney, Appl. Phys. Lett. **94**, No. 232108 (2009).
- [5] R. E. Algra, M. A. Verheijen, M. T. Borgström, Lou-Fé Feiner, G. Immink, W. J. P. van Enkevort, E. Vlieg and E. P. A. M. Bakkers, Nature **456**, 369 (2008).
- [6] P. Caroff, K. A. Dick, J. Johansson, M. E. Messing, K. Deppert and L. Samuelson, Nature Nanotech. **4**, 50 (2009).
- [7] F. M. Ross, Nature Nanotech. **4**, 17 (2009).
- [8] D. Spirkoska et al., Phys. Rev. B **80**, No. 245325 (2009).
- [9] J. Bao, D. C. Bell, F. Capasso, J. B. Wagner, T. Mårtensson, J. Trägårdh and L. Samuelson, Nano Lett. **8**, 836 (2008).
- [10] T. Akiyama, T. Yamashita, K. Nakamura and T. Ito, Nano Lett. **10**, 4614 (2010).
- [11] L. Jin, J. Wang, S. Jia, H. Sang, L. Deng, X. Yan, Y. Cai, P. Lu and W. C. H. Choy, CrystEngComm **12**, 150 (2010).
- [12] S. Chung, D. J. Smith and M. R. McCartney, Microsc. Microanal. **13**, 329 (2007).
- [13] M. R. McCartney and M. Gajdardziska-Josifovska, Ultramicroscopy **53**, 283 (1994).
- [14] A. Qteish, V. Heine and R. J. Needs, Phys. Rev. B **45**, 6534 (1992).
- [15] M. Posternak, A. Baldereschi, A. Catellani and R. Resta, Phys. Rev. Lett. **64**, 1777 (1990).

- [16] S. Ke, K. Zhang and X. Xie, *J. Phys.: Condens. Matter* **8**, 10209 (1996).
- [17] F. Bechstedt, P. Käckell, A. Zywietz, K. Karch, B. Adolph, K. Tenelsen and J. Furthmüller, *phys. stat. sol. (b)* 202, **35** (1997).
- [18] M. R. McCartney, F. A. Ponce, J. Cai and D. P. Bour, *Appl. Phys. Lett.* **76**, 3055 (2000).
- [19] O. Ambacher, R. Dimitrov, M. Stutzmann, B. E. Foutz, M. J. Murphy, J. A. Smart, J. R. Shealy, N. G. Weimann, K. Chu, M. Chumbes, B. Green, A. J. Sierakowski, W. J. Schaff and L. F. Eastman, *phys. stat. sol. (b)* **216**, 381 (1999).
- [20] F. Bernardini, V. Fiorentini and D. Vanderbilt, *Phys. Rev. B* **56**, R10024 (1997).
- [21] S. de Gironcoli, S. Baroni and R. Resta, *Ferroelectrics* **111**, 19 (1990).
- [22] J. F. Nye, *Physical Properties of Crystals*, Oxford Univ. Press, Oxford (1985).
- [23] F. Boxberg, N. Søndergaard and H. Xu, *Nano Lett.* **10**, 1108 (2010).
- [24] M. J. Hytch, E. Snoeck and R. Kilaas, *Ultramicroscopy* **74**, 131 (1998).
- [25] F. Hüh, M. Hytch, F. Houdellier, E. Snoeck and A. Claverie, *Mater. Sci. Eng., B* **154-155**, 221 (2008).
- [26] I. Strzalkowski, S. Joshi and C. R. Crowell, *Appl. Phys. Lett.* **28**, 350 (1976).
- [27] L. Reimer, *Transmission Electron Microscopy*, Springer, Berlin (1989).
- [28] M. Gajdardziska-Josifovska and A. H. Carim, *Introduction to Electron Holography*, Chapter 12, Kluwer Academic/Plenum Publishers, New York (1999).
- [29] P. A. Stadelmann, *Ultramicroscopy*, **21**, 131 (1987).
- [30] P. A. Doyle and P. S. Turner, *Acta Cryst.* **A24**, 390 (1968).
- [31] R. D. King-Smith and D. Vanderbilt, *Phys. Rev. B* **47**, 1651 (1993).
- [32] R. Resta, *Rev. Mod. Phys.* **66**, 899 (1994).

- [33] G. Kresse and J. Furthmüller, Phys. Rev. B **54**, 11169 (1996).
- [34] G. Kresse and J. Furthmüller, Comput. Mater. Sci. **6**, 15 (1996).
- [35] T. Ogawa, J. Phys. Soc. Jpn. **25**, 1126 (1968).
- [36] Q. Y. Xu, Y. Wang, Y. G. Wang, X. L. Du, Q. K. Xue and Z. Zhang, Appl. Phys. Lett. **84**, 2067 (2004).

Chapter 6

SUMMARY AND FUTURE WORK

6.1 Summary

The research described in this dissertation has involved quantitative determination of electrostatic potentials and charge distributions in semiconductor nanostructures primarily using the technique of off-axis electron holography.

Epitaxial Ge quantum dots (QDs) embedded in boron-doped Si have been studied [1]. The number of holes associated with a single QD has been estimated based on the excess phase shifts observed close to the base of the Ge dot. The resulting estimate of charge density was (0.03 ± 0.003) holes/nm³, which corresponded to about 30 holes localized to a pyramidal, 25-nm-wide Ge QD. For comparison, using a capacitance-voltage measurement, the average number of holes confined to each Ge dot was found to be about 40. The difference in the obtained numbers of holes confined to a single Ge dot emphasized the capability of off-axis electron holography for measuring charges confined to individual nm-scale regions of a heterogeneous sample.

Hole accumulation in Ge/Si core/shell nanowires (NWs) has been observed and quantified using off-axis electron holography as well as other electron microscopy techniques [2]. High-resolution electron microscopy and elemental line profiling with energy-dispersive X-ray spectroscopy confirmed the crystallographic and compositional structure of the core/shell NWs. High-angle annular-dark-field (HAADF) scanning transmission electron microscopy images

and off-axis electron holograms were obtained from specific NWs. The former technique provided accurate information about projected thicknesses for both the Ge core and the Si shell, and the excess phase shifts measured by electron holography across the NWs corresponded to the presence of holes inside the Ge cores. Calculations based on a simplified coaxial cylindrical model gave hole densities of $(0.4 \pm 0.2) / \text{nm}^3$ in the core region, which were in reasonable agreement with the estimates of hole densities based on published measurements.

Homogeneous zincblende (ZB) /wurtzite (WZ) heterostructure junctions in ZnSe nanobelts have also been characterized using off-axis electron holography [3]. The observation of electrostatic fields and charge accumulation was attributed to spontaneous polarization (SP) present in the WZ regions, which was calculated to be $p_{\text{sp}} = -(0.0029 \pm 0.00013) \text{ C/m}^2$. Since there are no reported SP values for WZ ZnSe available for comparison, a first-principles' calculation was also performed which gave $p_{\text{sp}} = -0.0063 \text{ C/m}^2$ for WZ ZnSe. The lower SP value calculated from electron holography was attributed to the screening effect of the surface amorphous layer. The contributions from piezoelectric polarization across the zincblende (ZB) /wurtzite interface were verified to be insignificant according to geometric phase analysis, and aberration-corrected HAADF imaging showed no polarity reversal across the ZB/WZ interface.

Overall, this work has confirmed that off-axis electron holography can be very useful for the nanoscale characterization of electrostatic potentials and charge distributions in semiconductor materials, which is not possible using conventional TEM or other experimental techniques. Moreover, the capability of

characterizing electrostatic properties for specific quantum dots, nanowires, or nanoscale heterojunctions is likely to be of considerable significance in developing future electronic devices.

6.2 Future Work

In chapter 3 and chapter 4, the hole accumulation in specific Ge quantum dots as well as in Ge/Si core/shell nanowires were observed and quantitatively determined. In chapter 5, the electrostatic field associated with SP in wurtzite structures of ZnSe was studied, and the SP value for ZnSe was determined. Thus, quantitative electron holography should be a powerful technique for future studies of electrostatic potential profiles across charged heterojunctions combined with nanoscale geometry.

The growth of *pn* junctions in semiconductor nanowires has recently been realized for axial *pn* junctions in Si [4] and Ge [5-6] nanowires, as well as radial *pn* junctions in GaAs [7], which are promising for applications in nanoscale optoelectronics such as photo-detectors and lasers [8]. Thus, it would be a useful direction for future electron holography studies to focus on electrostatic potential characterization along Si (Ge) *pn* junction nanowires, as well as *pn* junctions in compound semiconductor nanowires.

As an example, Ge nanowires with *pn* junctions have been grown using chemical vapor deposition, utilizing the vapor-liquid-solid (VLS) growth mode [3]. B₂H₆ and PH₃ were used to provide the *p*- and *n*-type dopants, respectively. A scanning electron microscopy image of Ge *pn* junction nanowires is shown in

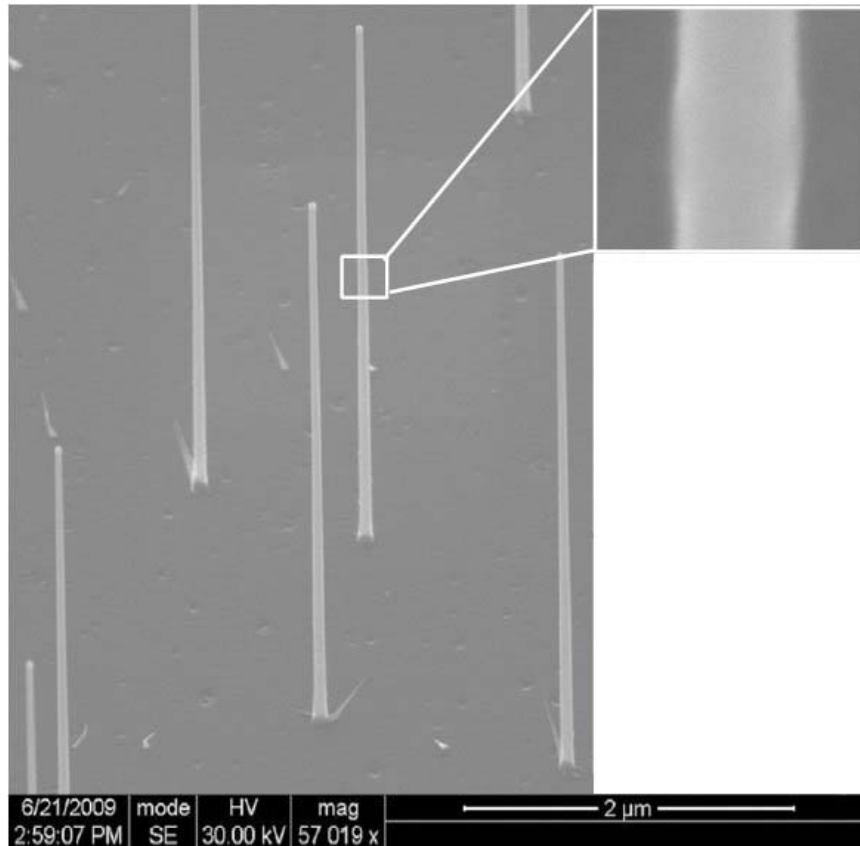


Figure 6.1 Scanning transmission electron microscopy image of Ge pn junction nanowires. The top inset shows the junction position, which is of slight larger diameter [6].

Figure 6.1. By resuming the VLS process after a 30 s purge between p - and n -segment growth, the Au-Ge alloy is reported to become supersaturated in Ge, which leads to an increase in alloy diameter prior to layer-by-layer Ge growth. The result is a slight diameter increase at the p - n junction, as illustrated in the inset of Figure 6.1 [6]. The sudden diameter change at the junctions would be very favorable for electron holography characterization since the location of the

p-n junctions can be easily identified. However, one problem with studying Ge *pn* junction nanowires is that the surfaces of the Ge nanowires are easily oxidized. On the other hand, Si *pn* junction nanowires grown using similar methods would be more suitable for electron holography study.

Preliminary holography studies of *pn* junctions in GaAs compound semiconductor nanopillars have already been carried out. As shown in Figure 6.2 (a), GaAs nanopillars were loaded on copper grids with uniform carbon film rather than holey carbon film which was normally used, since the latter would introduce uneven background to the holograms obtained. Although the nanopillars have overall good crystal quality, as can be seen from the high-resolution electron microscopy image in Figure 6.2 (b), there are many stacking faults and twinning structures perpendicular to the growth direction. These samples are not ideal for electron holography characterization since they would tend to induce extra diffraction contrast, and the magnitude of the phase shift corresponding to the diffraction contrast may be comparable to the useful information. The GaAs nanopillars are normally several microns in length, and over 100 nm in diameter. In order to obtain a field of view as large as possible, the Lorentz lens of the electron microscope was used instead of the normal objective lens. Unlike the case for Ge nanowires, the side-walls of the GaAs pillars were uniform all along the length of the nanopillar, which made determination of the locations of the *pn* junctions very difficult. Serial holograms were obtained from one end of the nanopillar all the way to the other end, and Figure 6.2 (c) shows a reconstructed phase image of an entire GaAs nanopillar. No abrupt phase change that would

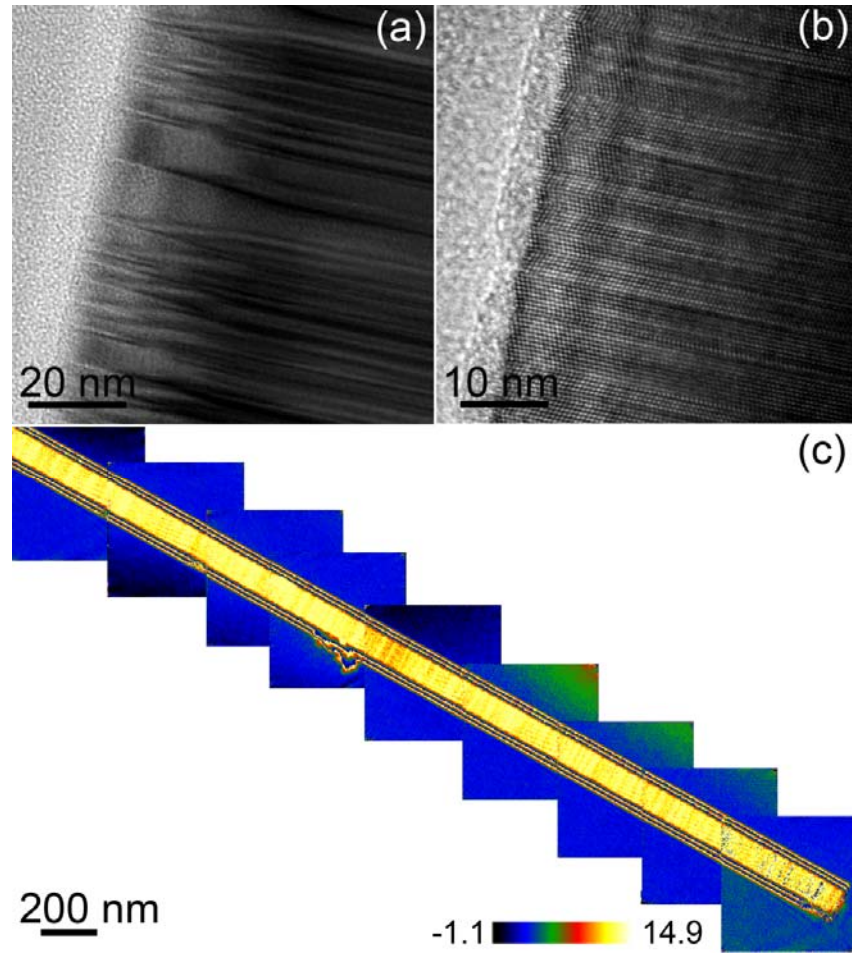


Figure 6.2 (a) Transmission electron micrograph of a GaAs nanopillar. (b) Corresponding high-resolution electron micrograph shows high density of stacking faults and twinning structures perpendicular to the growth direction. (c) phase image of an entire GaAs nanopillar.

correspond to the pn junction is observed, while diffraction contrast induced by stacking faults and twinning structures is also visible.

Further experiments should be carried out using nanopillars with much reduced stacking fault density, and samples will need to be tilted to avoid diffraction contrast as much as possible.

REFERENCES

- [1] L. Li, S. Ketharanathan, J. Drucker and M. R. McCartney, Appl. Phys. Lett. **94**, 232108 (2009).
- [2] L. Li, D. J. Smith, E. Dailey, P. Madras, J. Drucker and M. R. McCartney, Nano Lett. **11**, 493 (2011).
- [3] L. Li, L. Jin, J. Wang, D. J. Smith, W. Yin, Y. Yan, W. C. H. Choy and M. R. McCartney, Phys. Rev. Lett. (submitted).
- [4] P. Agarwal, M. N. Vijayaraghavan, F. Neuilly, E. Hijzen and G. A. M. Hurkx, Nano Lett. **7**, 896 (2007).
- [5] E. Tutuc, J. Appenzeller, M. C. Reuter and S. Guha, Nano Lett. **6**, 2070 (2006).
- [6] S. T. Le, P. Jannaty, A. Zaslavsky, S. A. Dayeh and S. T. Picraux, Appl. Phys. Lett. **96**, 262102 (2010).
- [7] J. Caram, C. Sandoval, M. Tirado, D. Comedi, J. Czaban, D. A. Thompson and R. R. LaPierre, Nanotechnology **21**, 134007 (2010).
- [8] J. Hu, Y. Liu, A. Maslov, C. Ning, R. Dutton, S. Kang, Proc. SPIE **6468**, 64681E (2007).

APPENDIX A
RELEVANT PUBLICATIONS

1. Luying Li, Lei Jin, Jianbo Wang, W.C.H. Choy, David J. Smith, and Martha R. McCartney, "Charge distribution tailoring across Zinc-blende/Wurtzite homogeneous heterostructure junctions in ZnSe nanobelts via spontaneous polarization". (Submitted)
2. Luying Li, David J. Smith, Eric Dailey, Prashanth Madras, Jeff Drucker, and Martha R. McCartney, "Observation of Hole Accumulation in Ge/Si Core/Shell Nanowires Using Off-axis Electron Holography", *Nano Lett.* **11**, 493-497 (2011).
3. Luying Li, D. J. Smith, P. Madras, E. Dailey, J. Drucker, and M. R. McCartney, "One-dimensional hole gas in Ge/Si core/shell nanowire studied by off-axis electron holography", *Proceedings of 17th International Microscopy Congress* **18.14** (2010).
4. Luying Li, David J. Smith, Prashanth Madras, Eric Dailey, Jeff Drucker, and Martha R. McCartney, "Hole accumulation in Ge/Si Core/Shell nanowires Studied by Electron Holography", *Microsc. Microanal.* **16 (Suppl 2)**, 566 (2010). DOI: 10.1017/S1431927610060174.
5. Martha R. McCartney, Nipun Agarwal, Suk Chung, David A. Cullen, Myung-Geun Han, Kai He, Luying Li, Hua Wang, Lin Zhou, and David J. Smith, "Quantitative phase imaging of nanoscale electrostatic and magnetic field using off-axis electron holography", *Ultramicroscopy* **110**, 375-382 (2010). ([Invited review](#))
6. Luying Li, Sutharsan Ketharanathan, Jeff Drucker, and Martha R. McCartney, "Study of hole accumulation in individual germanium quantum dots in *p*-type silicon by off-axis electron holography", *Appl. Phys. Lett.* **94**, 232108 (2009). ([Also selected in Virtual Journal of Nanoscale Science & Technology, June 29, 2009, Volume 19, Issue 26](#))
7. Ke Zhang, Jianbo Wang, Xiaoli Lu, Luying Li, Yiwen Tang, and Zhiyong Jia, "Structural Evolution of Hydrothermal-Synthesized $\text{Ni}(\text{SO}_4)_{0.3}(\text{OH})_{1.4}$ Nanobelts During *ex situ* Heat Treatment and *in situ* Electron Irradiation", *J. Phys. Chem. C* **113**, 142-147 (2009)
8. Luying Li, Martha R. McCartney, David J. Smith, Sutharsan Ketharanathan, and Jeff Drucker, "Study of epitaxial germanium quantum dots in silicon by off-axis electron holography", *Microsc. Microanal.* **14 (suppl. 2)**, 404-405 (2008). DOI: 10.1017/S143192760808416X.
9. Jianbo Wang, Luying Li, Zhe Liu and Renhui Wang, "Nano-Composite Materials Studied by CTEM and STEM", *Solid State Phenomena* **121-123**, 991-994 (2007).

10. Jianbo Wang, Luying Li, Dongxia Xiong, Renhui Wang, Dongshan Zhao, Changping Min, Ying Yu and Lili Ma, “High spatially resolved morphological, structural and spectroscopical studies on copper oxide nanocrystals”, *Nanotechnology* **18**, 075705 (2007).
11. Yiwen Tang, Zhiyong Jia, Yun Jiang, Luying Li, and Jianbo Wang, “Simple template-free solution route for synthesis of $\text{Ni}(\text{SO}_4)_{0.3}(\text{OH})_{1.4}$ nanobelts and their thermal degradation”, *Nanotechnology*, **17**, 5686-5690 (2006).
12. Luying Li, Jianbo Wang, Renhui Wang, Huijun Liu, Chunlin Jia, Lili Ma, and Ying Yu “Atomistic study on twinning of Cu_2O quantum dots”, *Appl. Phys. Lett.* **89**, 113109 (2006).

This document was generated using the Graduate College Format Advising tool. Please turn a copy of this page in when you submit your document to Graduate College format advising. You may discard this page once you have printed your final document. DO NOT TURN THIS PAGE IN WITH YOUR FINAL DOCUMENT!